LAURA COLLICA

EXPERIMENTAL RESULTS ON SCINTILLATING CRYSTALS FOR DUAL-READOUT CALORIMETRY

UNIVERSITÀ DEGLI STUDI DI PAVIA
FACOLTÀ DI SCIENZE MM. FF. NN.
CORSO DI LAUREA MAGISTRALE IN SCIENZE FISICHE

EXPERIMENTAL RESULTS ON SCINTILLATING CRYSTALS FOR DUAL-READOUT CALORIMETRY

Relatore
Ch.mo Prof. Michele Livan

Correlatore
Dott. Gabriella Gaudio

Tesi di Laurea di
LAURA COLLICA

Anno Accademico 2010/2011

The most exciting phrase to hear in science,
the one that heralds the most discoveries, is not "Eureka!"
but "That's funny..."

— Isaac Asimov

SOMMARIO

Gli esperimenti agli acceleratori di particelle contribuiscono da sempre al progresso della conoscenza in fisica delle alte energie. Nei moderni esperimenti la spettroscopia ad alta precisione dei jet ha assunto un ruolo fondamentale e la realizzazione di calorimetri, i.e. rivelatori che misurano l'energia delle particelle mediante assorbimento, ad alta risoluzione in energia, è diventata cruciale.

I calorimetri sono strumenti molto complessi e la loro performance è limitata da alcuni fattori intrinseci, specialmente nel caso dei calorimetri adronici. In quest'ultimi le reazioni nucleari indotte dagli adroni causano l'emissione di nucleoni a spese dell'energia depositata dalle particelle dello sciame. L'energia utilizzata per liberare i nucleoni non produce un segnale misurabile (*invisible energy phenomenon*). Inoltre la produzione di mesoni neutri π^0, che decadono elettromagneticamente, dà origine ad una componente elettromagnetica (*electromagnetic fraction* f_{em}) che varia molto da evento a evento. Questi due aspetti rendono il calorimetro adronico non lineare e vari metodi sono stati sviluppati per eliminarne gli effetti. Uno di questi è il metodo a doppia lettura (*Dual-REAdout Method*), attraverso il quale è possibile misurare la f_{em} evento per evento e quindi eliminare le relative fluttuazioni. Inoltre, attraverso questa tecnica è possibile misurare anche il contributo dei neutroni al segnale evento per evento, e quindi stimare l'energia invisibile.

Il metodo a doppia lettura può essere applicato sia a calorimetri a campionamento che omogenei, e si basa sulla misura simultanea della luce di scintillazione e della radiazione Cherenkov, prodotte nei processi di sviluppo dello sciame. Poichè la luce Cherenkov viene prodotta solo da particelle relativistiche, mentre la scintillazione è prodotta da tutte le particelle ionizzanti, la frazione elettromagnetica viene stimata comparando i contributi dei due segnali.

Nel caso di un calorimetro a campionamento vengono utilizzati due mezzi attivi, uno sensibile a tutte le particelle ionizzanti, e uno che genera radiazione Cherenkov.

Nel caso invece di un calorimetro omogeneo, e.g. cristallo scintillante, il mezzo deve produrre entrambi i tipi di radiazione e le due componenti devono venire separate off-line per poter applicare la tecnica a doppia lettura. Per dividere i due contributi vengono sfruttate le differenze nella direzionalità, nella struttura temporale e nello spettro ottico.

Nella mia tesi, dopo aver discusso gli aspetti fondamentali della calorimetria, descrivo la tecnica a doppia lettura in modo approfondito,

e discuto l'analisi a cui ho lavorato nell'ambito della collaborazione DREAM.

In particolare, nel mio lavoro di tesi presento l'analisi sistematica di otto cristalli di $PbWO_4$, eseguita per determinarne le caratteristiche in termini di emissione di luce Cherenkov e di attenuazione della luce lungo il cristallo. Discuto poi i risultati ottenuti con un prototipo ibrido, costituito da una matrice di cristalli e da un calorimetro a fibre.

Infine descrivo lo studio sulla polarizzazione della luce Cherenkov in cristalli di BSO. La polarizzazione della luce Cherenkov può infatti essere sfruttata come ulteriore strumento di separazione della radiazione Cherenkov dalla scintillazione.

ACKNOWLEDGMENTS

I owe my gratitude to all those people who have made this dissertation possible and because of whom my graduate experience has been one that I will cherish forever.

First and foremost, my utmost gratitude to my supervisor Professor Michele Livan, who has guided and helped me all time, with patience and kindness. Thanks to him, I have learned a lot and I have understood my research area better.

I am grateful to my advisor Dr. Gabriella Gaudio for tutoring, and advice as a friend. She has helped me during the entire thesis and she has carefully read and commented on countless revisions of this manuscript.

My sincere thanks also goes to Dr. Silvia Franchino, who has helped me directly during the data analysis and has assisted me in using the software needed for the analysis.

I would like to show my gratitude for having actively participated in the DREAM research program. For the first time I could work in an international collaboration and this has been very exciting and instructive for me. I would like to thank every member of the DREAM Collaboration, for having made the testbeam activity enjoyable. In particular I thank Dr. Nural Akchurin, who have given me advice on how to carry out the analysis.

Most importantly, I owe my deepest gratitude to my family, which has supported me and has been a constant source of love, concern, support and strength all these years.

I'm also grateful to my boyfriend Marco, who has always encouraged me and his support and care helped me overcome difficulties. I am thankful also for his "IT consulting".

I'm thankful to André Miede for classicthesis style and to the LyX community, you have made my work easier.

Last but not the least, I would like to thank all the people who have made these two years amusing and lovely. Particularly I'm grateful to Duda, Marko, Matteo, Cecilia, Titty, Sara, Luca, Luca2, Serena, Marco, Syl and Rina for their constant support and for the amazing days spent together.

CONTENTS

LIST OF FIGURES

LIST OF TABLES

ACRONYMS

DREAM	Dual-REAdout Method
MC	Monte Carlo
BGO	bismuth germanate
BSO	bismuth silicate
PMT	PhotoMultiplier Tube
DWC	Delay Wire Chamber
TDC	Time to Digital Converter
ADC	Analog to Digital Converter
SPS	Super Proton Syncrotron

1

INTRODUCTION

Experiments at proton and electron colliders contribute to the knowledge at high energy physics since a long time. Colliding-beam machines play a very important role, since they are characterized by a large energy available in the center-of-mass system for creation of new states. The detector systems in these experiments have to record position and momentum of particles and the need of precise timing, good spatial and energy resolution leads to different design of detector systems and to develop new methods to improve their precision.

Energy measurement by total absorption methods allows to evaluate the energy and the position coordinates of particles from high energy interactions. These kind of detectors are called calorimeters. In the absorption process, the particles interact with the dense material of the calorimeter and generate a cascade, depositing their energy.

The calorimetric information contributes also to particle identification (electrons, gammas, muons, jets). Since electrons have an important role in pointing to new physics and the energy resolution of calorimeters improves with energy, this type of device will be more and more important as the collision energy increases. The identification of hadrons and jets is even more important because the branching ratios involved are greater than the leptonic ones. Moreover, since the calorimeter signals can be fast (up to 100 ns), these instruments are widely used also as part of the triggering system.

On the other hand calorimeters show limiting factors, especially the hadronic ones. In showers developed by hadrons, strong interaction contributes to the production of hadrons, most of which are pions, and to the occurrence of nuclear reactions. In the latter processes, neutrons and protons are released from atomic nuclei and to do this binding energy must be provided. The energy used for this purpose does not contribute to the calorimeter signal (the so called *invisible energy phenomenon*). Furthermore in the hadronic processes neutral pions, produced by the strong interaction, decay in two photons, which start electromagnetic showers. The fraction of shower energy carried by the electromagnetic component increases on average with the shower energy and fluctuates strongly from event to event. These variations contribute considerably to the hadronic energy resolution and are added to other fluctuations that affect the precision of electromagnetic and hadronic calorimetric measurements, such as signal quantum fluctuations, sampling fluctuations for non-homogeneous calorimeters, shower leakage fluctuations and others.

The effects of both the electromagnetic fraction f_{em} of the hadronic shower and the invisible energy make the calorimeter non-linear for hadronic detection. Instead, in the case of electromagnetic calorimeters, the processes through which energy is deposited produce phenomena that always generate a signal proportional to the deposited energy.

To cope with these limiting factors some methods were designed in the last years and in my thesis I will discuss the *Dual-Readout Method*, a technique to measure the electromagnetic fraction f_{em} event by event, in order to eliminate the relative fluctuations, which affect the hadronic energy resolution. This method consists in using two different active media, one sensitive to all ionizing particles, e.g. a scintillating material, and one which generates Cherenkov light produced by the shower particles, or only one material that produces both kinds of light, as a scintillating crystal.

The Cherenkov light is due almost exclusively to the electromagnetic shower component. Indeed, electrons and positrons are relativistic down to keV while spallation protons, which dominate the non-em component of the hadronic shower, are typically non-relativistic. The scintillation signal is generated by both relativistic and non-relativistic particles: a comparison of scintillation and Cherenkov signal thus allows to estimate the electromagnetic shower fraction event by event.

The first detector which demonstrated the feasibility of this technique was a calorimeter called Dual-REAdout Method (DREAM), based on a copper absorber structure and equipped with two types of optical fibers, which generate the scintillation and the Cherenkov light separately. The choice of a fiber calorimeter was done for the possibility to measure the relative contribution of the scintillator and the Cherenkov signals independently, without any contamination.

However, because of the sampling fluctuations and the poor Cherenkov light yield, energy resolution was limited. In order to overcome this problem the DREAM collaboration started using crystals for dual-readout purposes in the last years. Indeed some crystals, as bismuth germanate (BGO) and lead-tungstate ($PbWO_4$) ones, are characterized by a relevant amount of Cherenkov light and can be exploited as media for an homogeneous calorimeter, not affected obviously by sampling fluctuations and whose signals are a mixture of scintillation and Cherenkov light.

A systematic study was carried out on BGO, on $PbWO_4$ with different Mo dopant concentrations and on bismuth silicate (BSO) crystals in order to have good Cherenkov vs. Scintillation separation, response uniformity and high light yield.

In my thesis I discuss the dual-readout calorimetry with crystals and I introduce the analysis that I have done within the Pavia group of the DREAM Collaboration on data taken during test-beams at the SPS proton synchrotron of CERN last year. In particular I have followed systematic studies on eight lead-tungstate crystals, doped with 0.3%

Molybdenum, in order to compare crystals response. I have studied the scintillation and Cherenkov light produced event by event as a function of the angle of rotation of the crystal with respect to the beam direction. This angular scan was done in order to exploit the isotropic emission of the scintillation light and the directionality of the Cherenkov light for separating the two contributions. The latter is indeed emitted at a characteristic angle by the relativistic shower particles that traverse the detector and is characterized by a peak near the angle at which it is most efficiently detected.

To best separate the two components, the integration of signal is done over the entire duration for the scintillation light, while it is done over a small time interval for the Cherenkov light, which is prompt and not characterized by a decay constant as the scintillation light.

Moreover optical transmission filters, a UV filter for Cherenkov readout and a yellow filter for scintillation readout, are used to reduce the contamination of scintillation in the Cherenkov signal and to exploit the different time structure in order to separate the two components.

The systematic study of signal attenuation and light yield was carried out to estimate the signal loss and also to discard the crystal with the worst characteristics, in order to make a seven crystal matrix for further tests.

Hereafter I have analyzed data relative to the mentioned $PbWO_4$ matrix, which forms the electromagnetic section of an hybrid calorimeter, in which the DREAM fiber prototype constitutes the hadronic section. These two calorimeters are characterized by different $^{e}/_{h}$ ratio, i.e. the ratio of the em to non-em responses, and their informations can be combined only because they both exploited the dual-readout technique. Indeed measuring the f_{em} event by event makes possible to correlate the two sections informations.

Besides this analysis, I participated in the studies on the polarization of Cherenkov light at different stages of the developing electron shower: since the Cherenkov light is polarized, while scintillation light is not, this aspect can be exploited as a tool to separate scintillation and Cherenkov components, by installing a polarizer filter with the transmission axes favorable to the Cherenkov light polarization. In these conditions, the Cherenkov light polarization was studied as a function of the shower development by putting lead slices of increasing thickness upstream the crystal and as a function of angle, in order to see that Cherenkov light is greatly suppressed when the filter is unfavorable, while the scintillation light does not change in both cases.

In addition to others methods as directionality, spectral characteristics, and time structure, polarization provides a fourth tool in order to distinguish scintillation and Cherenkov light. All this features, except the Cherenkov directionality, could be exploit in 4π calorimeters designed for a colliding beam experiment: different filters used to read out the crystals from the upstream and downstream ends are very promising in this context, especially if the time structure of these signals is measured as well. Installing polarization filters with the transmission axes orientated perpendicular to each other on the upstream and downstream readout channels might provide additional separation power in such a geometry.

2

CALORIMETRY IN PARTICLE PHYSICS

2.1 INTRODUCTION TO CALORIMETRY

In nuclear and particle physics the measurement of particles properties is performed by many devices: one of them is the calorimeter, typically a block of dense matter, in which the detection of particles is done through total absorption.

There are different types of calorimeters but all of them have a common feature: the measurement process through which the particle properties are estimated is destructive. Indeed, after the passage through the calorimeter, particles are no longer available for additional measures by other devices. There is one exception to this rule and concerns the minimum ionizing particles, such as muons, which may penetrate a substantial amount of matter represented by a calorimeter losing energy only by ionization and excitation, and for this reason they could be merely identified.

The term calorimetry finds its origin in thermodynamics and concerns the fact that in the absorption process almost all the particle's energy is eventually converted into heat. However the amount of energy involved in this process is very different from the thermodynamic one. In modern accelerator experiments the most energetic particles are measured in units of TeV ($1\,TeV = 10^{12} eV = 1000\,GeV$), while 1 calorie is equivalent to about 10^7 TeV. Therefore, the rise in temperature in the calorimeter is negligible and complicated methods are required to determine the particle properties.

The advent of scintillation counters opened the way to calorimetric particle detection, since in these detectors the fluorescence light produced by ionizing particles is related to the deposited particle's energy. The invention of the photomultiplier tube (PMT), which converts light into electric signals, allowed to use this phenomenon for quantitative measurements of particle properties. At that time standard scintillators were anthracene and thallium doped sodium iodide crystals but with the development of semiconductor detectors, which provided an improvement in energy resolution, semiconductor counters became the instruments of choice in nuclear γ-ray spectroscopy. In Figure 2.1.1 the difference between the two types of detector response is clearly visible.

Calorimetry started to play an important role in particle physics's experiments when shower counters were used in fixed-target experiments to get informations about photons produced by π^0 decays. Since photons could not be tracked in magnetic field and bubble chambers

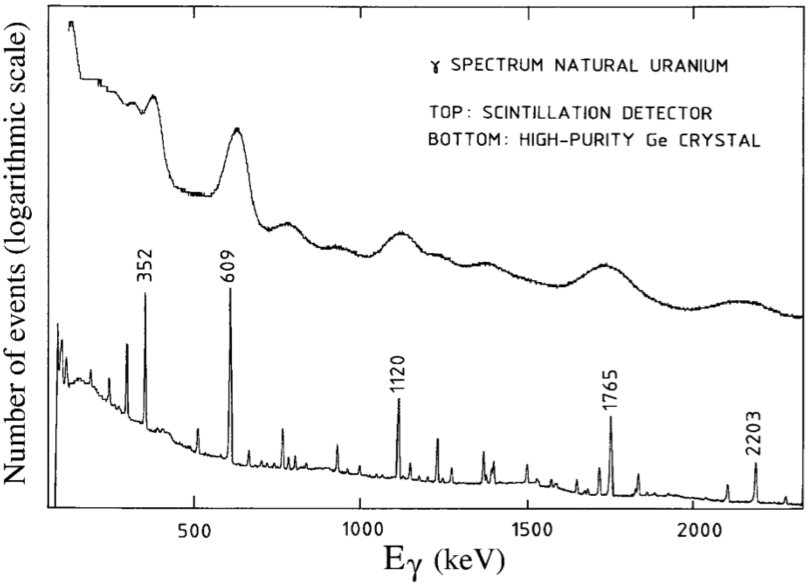

Figure 2.1.1: Nuclear γ-ray spectrum of decaying uranium nuclei, measured with a bismuth germanium oxide scintillation counter (upper curve) and with a high-purity germanium crystal (lower curve). Courtesy of G. Roubaud, CERN.

were poor efficient, NaI(Tl) scintillators were introduced to settle this problem: photons were measured with 100% efficiency and the π^0 reconstruction could be achieved with high efficiency too, since it was possible to reach sub-1% resolutions. This result generated a growing interest in crystal calorimetry for particle physics experiments and new types of crystals were developed to meet specific needs of experiments, as for example signal speed and radiation hardness. In the 1960 the lead-glass detector became popular for its signal speed: this high density material did not scintillate but it was characterized by the instantaneous Cherenkov emission.

Calorimeters can be divided into two different types: homogeneous calorimeters, like the shower counters mentioned above, and sampling calorimeters. In the former, the entire volume is sensitive to the particles and may contribute to the signal. The material of the detector must have both the function of absorbing the particles and of generating the signals and so it usually needs to have a high density. In the latter, these functions are performed by different materials, usually called the passive and active medium, respectively. The passive medium has to be a high-density material, such as iron, copper, lead or uranium, while the active medium has to generate the signals. In sampling calorimeters, typically a few percent of the energy in the shower is actually sampled and so the energy resolution that is obtained is significantly worse than the one which can be achieved with a homogeneous calorimeter. However, since they are also substantially cheaper, the development of sampling calorimeters is driven by the request for very large detector systems.

As the energy limits were pushed further by new generations of particle accelerators, calorimeters became fundamental within particle physics experiments. In fact, one of the most important feature of a calorimeter is the energy resolution dependence on the particle energy:

$$\frac{\sigma(E)}{E} \propto \frac{1}{\sqrt{E}} \tag{2.1}$$

The precision of the information provided by calorimeters improves with increasing energy, while for example the precision of momentum measurement by magnetic deflection decreases with it, due to the lower bending radius. The energy dependence of calorimeter resolution is due to the statistical nature of the physics processes involved in the generation of the calorimeter signals.

Combining the calorimetric information with tracking data, it is possible to identify some particles, e.g. electrons, and this is a very important feature at new colliders, since for example electrons have an important role in signaling new physics. Moreover, in experiments with 4π detectors at colliding-beam machines, the measurement of jets and missing energy (energy flow) turns out to be crucial since, when observed in combination with lepton production, it is a signature for interesting physics. In this context, since the calorimeter signals can be fast (up to 100 ns), these instruments offer also the possibility of event selection ("triggering").

Calorimeters do not need magnetic field for energy measurement. They are sensitive to both neutral and charged particles and the possibility of high segmentation allows to perform precise measurement of the direction of incoming particles.

In the last 20 years, all new accelerator facilities for experimental particle physics have been colliding-beam machines (such as LEP and the LHC at CERN or the Tevatron at Fermilab, etc.). At these facilities experiments consist of 4π detectors, i.e. detectors which have to cover as large solid angle around the interaction point as possible. This feature is called hermeticity and usually holds an important role in design criteria. Obviously, given the space requirements of the beampipe and of the signal cables, a complete coverage of the interaction vertex is not possible, but in modern experiments calorimeters with hermeticity f almost 90% are normally achieved.

Finally, it is necessary to mention that calorimetry is a widespread technique also in non accelerator-based experiments, especially those ones designed to study neutrino oscillations, cosmic rays and rare phenomena as proton decay or double-beta decay, which require a very large target mass to be detected. For example, the Super Kamiokande neutrino observatory consists of 50000 tons of ultra-pure water.

2.2 DETECTION MECHANISMS

The signal generation in a calorimeter is in general due to scintillation, Cherenkov radiation or ionization process. In this section these mechanisms are summarized.

Generally the passage of charged particles through matter causes them to lose energy by electromagnetic interaction with the Coulomb fields of the charged constituents of the medium. This energy may ionize or excite the atoms or molecules of the traversed medium, as discussed below.

2.2.1 *Scintillation*

Scintillation is a process associated with the excitation of the medium by particles passing through it. The excited atoms or molecules return to the ground state, emitting one or more photons. The decay time depends on many factors, such as the excitation energy and the number of available decay channels and therefore depends strictly on the scintillator material.

Scintillator materials exhibit the property known as *luminescence*: when exposed to certain form of energy, such as radiation or heat, they absorb and re-emit the energy in the form of visible light. If the re-emission occurs within $10^{-2} - 10^{-6} s$ the process is called *fluorescence*. There are many materials which scintillate: inorganic crystals, organic compound or gases. Scintillating crystals such as NaI(Tl) and BGO have decay times of several hundred of ns while complex organic scintillators, such as the plastic polystyrene, are characterized by decay times of tens of ns.

The scintillation process was the first to be used for the production of calorimetric signals and nowadays, many experiments exploit calorimeters in which the signals are generated through the scintillation light.

As mentioned before, the PhotoMultiplier Tube (PMT) plays a very important role in this type of calorimeters since it converts the scintillation light into electric signals, through a low-noise amplification. PMTs have to be optically coupled to the scintillator, and this is often done through a light guide which allows to adapt the end face of the scintillator to the PMT window. Since emission spectrum of a scintillator often peaks at UV wavelength, wavelength shifters are used to match the spectral sensitivity of the photomultiplier, which is characterized by a maximum in the visible range. These devices absorb the scintillation light and re-emit it at a longer wavelength. Wavelength shifter plates are often exploited in experiments: for example, light produced in scintillator plates of a sampling calorimeter is wavelength shifted and at the same time redirected towards the backside of the calorimeter, where the PMTs are located.

Finally it is important to mention the development of plastic optical fibers, which had highly influenced the design of scintillator calorimeters. The increasing use of scintillating fibers in calorimetry is indeed due to the following reason: fibers may be both the source of the light (generated isotropically) and the medium through which the light is guided to the readout. The major advantages offer by optical fibers are:

- very high sampling frequency (good energy resolution) if they are used as the active medium in a sampling calorimeter;
- high signal speed;
- good position resolution thanks to the arbitrary granularity allowed by the calorimeter structure;
- the possibility of an almost hermetic calorimeter structure;
- high light yield and excellent cost/performance ratio.

2.2.2 *Cherenkov radiation*

Cherenkov radiation occurs when a charged particle travels faster than light in a medium:

$$v > \frac{c}{n} \; or \; \beta > \frac{1}{n} \tag{2.2}$$

Cherenkov radiation is emitted because the charged particle polarizes the atoms along its path so that they become electric dipoles: the time variation of the dipole field leads to emission of electromagnetic radiation. The coherent wavefront is conical in shape and is emitted at a characteristic angle with respect to the direction of the particle:

$$cos\theta_C = \frac{1}{\beta n} \tag{2.3}$$

At threshold, i.e. $\beta = 1/n$, Cherenkov radiation is emitted in the forward direction. The spectrum exhibits a $1/\lambda^2$ dependence and, therefore, the visible part of Cherenkov light is seen as blue light. The contribution of Cherenkov radiation to the energy loss is very small compared to that from ionization and excitation, even for minimum-ionizing particles (MIP).

Since the Cherenkov process is sensitive to the particle velocity, it can be exploited for particle identification, in combination with a momentum measurement done with a magnetic spectrometer. For this reason, many devices have been developed for particle identification (threshold Cherenkov counters, differential Cherenkov counters, RICH). Besides, as Cherenkov light is emitted instantaneously, a Cherenkov detector will be chosen in experiments which require high signal speed.

All transparent materials are candidates for Cherenkov radiators, in particular many scintillators and light guides.

2.2.3 *Ionization*

The energy loss mechanisms through ionization depend on the nature and the mass of the particle and therefore the discussion is carried out for electrons/positrons and heavy particles (muons, pions, protons, α-particles) separately.

In the case of heavy particles, inelastic collisions with the atomic electrons of the material are almost solely responsible for the energy loss. The amount transferred in each collision is generally a very small fraction of the total kinetic energy of the particle, however, in normally dense matter, the number of collisions per unit path length is so large that a substantial cumulative energy loss is observed even in relatively thin layers of material. Elastic scattering from nuclei also occurs frequently although not as often as electron collisions. In this case, very little energy is transferred since mass of nuclei of most materials are usually large compared to the incident particle.

Inelastic collisions are statistical in nature and, because their number per macroscopic path length is generally large, the fluctuations in the total energy loss are small and therefore an average energy loss per unit path length, the stopping power dE/dx, can be used. This quantity was first calculated by Bohr using classical arguments but the correct quantum mechanical calculation was performed by Bethe, Bloch and other authors. In the calculation is assumed that the incident particle remains undeviated from its original path because of its much larger mass and that the electron is free and at rest.

The energy transfer, parametrized in term of momentum transfer is equal to:

$$-\frac{dE}{dx} = 2\pi N_a r_e^2 m_e c^2 \rho \frac{Z}{A}\frac{z^2}{\beta^2}\left[ln\left(\frac{2m_e\gamma^2 v^2 W_{max}}{I^2}\right) - 2\beta^2 - \delta\right] \quad (2.4)$$

This equation is known as the Bethe-Bloch formula and it is the fundamental expression used for energy loss calculations [32]. It is expressed in $MeV\, g^{-1} cm^2$. W_{max} is the maximum energy transferred in a single collision, which is produced by a knock-on collision (δ-rays), I is the mean excitation potential and δ is the density correction due to the electric field of the particle which tends to polarize the atom along its path, shielding the particle charge. The minimum value of dE/dx is almost the same for all particles of the same charge, and a particle at this status is known as *Minimum Ionizing Particle* (MIP). The stopping power as function of energy is shown for different particles in Figure 2.2.1.

Like heavy charged particles, electrons and positrons also undergo a collision energy loss when passing through matter. However, because

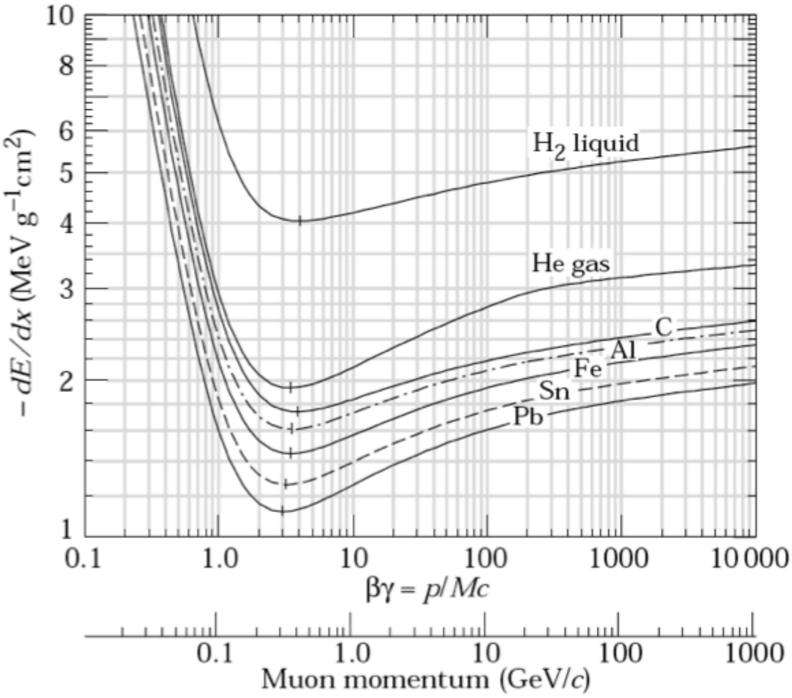

Figure 2.2.1: The stopping power as a function of momentum for different particles. [33]

of their small mass, an additional energy loss mechanism comes into play: the emission of electromagnetic radiation arising from scattering in the electric field of a nucleus, called *bremsstrahlung radiation*.

The Bethe-Bloch formula for heavy particles has to be modified because now the collision process is between identical particles: in the case of electrons the calculation must take into account the indistinguishability and the assumption that the incident particle is not deflected is no more valid.

It becomes:

$$\left(\frac{-dE}{dx}\right)_{ion} = 2\pi N_a r_e^2 m_e c^2 \rho \frac{Z}{A}\frac{1}{\beta^2}\left[ln\left(\frac{\tau^2(\tau+2)}{2(I/m_e c^2)^2}\right) + F(\tau) - \delta\right] \tag{2.5}$$

where τ is the kinetic energy of particle in units of $m_e c^2$ and F(τ) is a function which is different for electrons and positrons and depends on β [32].

Regarding the energy loss by radiation, it becomes comparable to the ionization loss at the critical energy ϵ_c, which depends on the Z-value of the material:

$$\left(\frac{dE}{dx}\right)_{rad} = \left(\frac{dE}{dx}\right)_{ion} \; for\, E = \epsilon_c \propto \frac{1}{Z} \tag{2.6}$$

At energies below $\sim$ 100 GeV, electrons and positrons are the only particles for which radiation contributes substantially to the energy loss of the particle. The emission probability in fact varies as the inverse square of the particle mass:

$$\sigma_{rad} \propto r_e^2 = \left(\frac{e^2}{mc^2}\right)^2 \qquad (2.7)$$

For example, radiation loss for muons (m = 106 MeV) is about 40000 times smaller than that for electrons.

Bremsstrahlung emission depends on the strength of the electric field felt by the electron, as shown by the following term:

$$\left(-\frac{dE}{dx}\right)_{rad} = 4\alpha N_a \frac{Z^2}{A} z^2 r_e^2 E\, ln \frac{183}{Z^{1/3}} \qquad (2.8)$$

Therefore the amount of screening from the atomic electrons surrounding the nucleus plays an important role.

A wide variety of particle detectors exploits these processes as the source of signal. The media used in ionizing detectors are often noble liquids/gases as argon, xenon and krypton, since they do not capture loose electrons, having all electronic shell of their atoms filled.

In the 1970's, calorimeters based on noble liquids as active media began to be used in particle physics experiments: liquid argon was preferred because is cheap, abundantly available and high purity levels are easily achieved. Nowadays, other noble liquids as xenon and krypton are used in experiments requiring high-Z absorbers as photon detectors. Unlike scintillation crystals, noble liquids are very radiation hard, i.e. resistant to ionizing radiation. This property is exploited, for example, in the ATLAS experiment with the lead/LAr sampling calorimeter for the electromagnetic shower detection.

Also gaseous media can be exploited for ionizing calorimeters. While in the case of liquid media there is no amplification process, in gaseous media the electrons produced in the ionization process may undergo considerable multiplication before being collected. As the electrons are accelerated by the electric field, they acquire enough energy to ionize in turn other atoms and thus generate an *avalanche*. These devices, such as wire chambers, can be used in calorimeter systems to provide the experimental signals, and are the best choice in terms of costs if large surface areas have to be covered. Nevertheless wire chambers are thin absorbers and therefore the distribution of the energy deposited in them is of the Landau type. They thus have poor energy resolution and they cannot be used as calorimeters, if high energy resolution is required.

Finally, solid state devices, based on semiconductor materials such as silicium, germanium and gallium arsenide, can also be used for particle detection. The very little energy required for the production of one electron-hole pair makes them excellent as high-resolution particle track detectors. In fact the energy for electron-hole pair production is typically one order of magnitude less than in gases, and two orders less than the energy required to produce one photoelectron in scintillation counters. Since the fluctuations in the number of primary charge carriers are one of the limiting factors for energy resolution in several types of detectors, these devices are very good candidates in many applications. These detectors are also studied as active material in sampling calorimeters, given also their fast response time. Thanks to their high density and compact structure semiconductor crystals may be much faster than other ionizing detectors.

2.2.4 *Photon interactions*

Processes which play a role in electromagnetic shower development are well understood: electrons and positrons lose energy by ionization and by radiation. The first process dominates at low energy while the second one at high energy, and the description of these mechanisms was given in the previous section.

Photons interact either through photoelectric effect, Compton scattering or pair production.

The photoelectric effect dominates at low energies in high-Z materials and in this process an atom absorbs a photon and emits an electron. The atom returns to the ground state through the emission of Auger electrons or X-rays. The photoelectric cross section depends strongly on the available number of electrons, and thus on the Z value of the absorber material:

$$\sigma_{p.e.} \propto \frac{Z^5}{E_\gamma^3} \tag{2.9}$$

In the Compton process, a photon is scattered by an atomic electron. Obviously, electrons are bound in matter, but if the photon energy is high with respect to the electron binding energy, the electron can be considered free. Since at least 40% of the total shower energy is deposited through Compton and photoelectric electrons, in the absorption process of multi GeV e^+, e^-, γ, the fine details of a calorimeter can be understood studying processes in the range between few hundred keV and few MeV.

The cross section for Compton scattering was one of the first process calculated using Quantum Electrodynamics and is known as the Klein–Nishina formula. It is a function of the scattering angle ϑ and of the electron energy ζ (see Figure 2.2.2):

$$\frac{d\sigma}{d\Omega} = \frac{r_e}{2} \frac{(1 + cos^2\theta)}{[1 + \zeta(1 - cos\theta)]^2} \left\{ 1 + \frac{\zeta^2(1 - cos\theta)^2}{(1 + cos^2\theta)\,[1 + \zeta(1 - cos\theta)]} \right\} \tag{2.10}$$

The cross section for Compton scattering depends linearly on the Z value of the absorber material than the cross section for photoelectric effect:

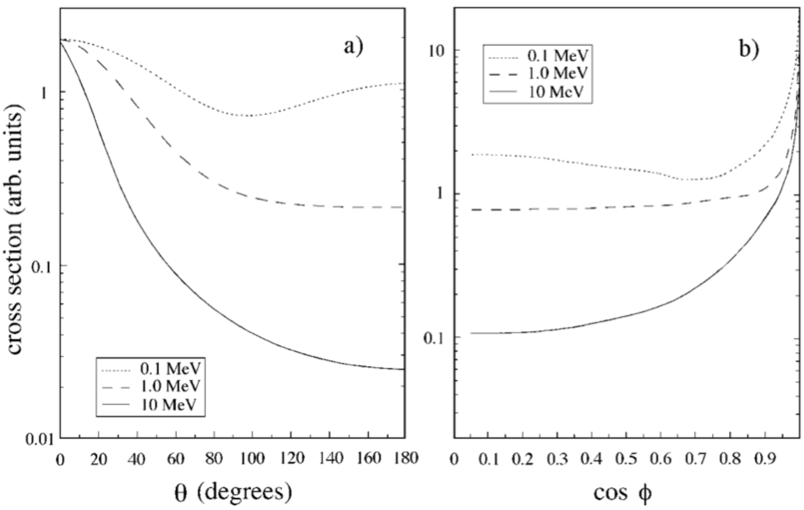

Figure 2.2.2: The cross section for Compton scattering as a function of the scattering angle of the photon (a), and the angular distribution of the Compton recoil electrons (b), for incident photons of different energies. [33]

$$\sigma^{atomic}_{Compton} = Z\sigma^{e}_{Compton} \tag{2.11}$$

However, as for the photoelectric effect, the cross section for Compton scattering decreases with increasing photon energy: $\sigma \propto 1/E$.

If the energy of the photon is at least two times larger than the mass of an electron, it can be converted in an electron and positron pair. This process can occur only in the field of a charge particle, otherwise energy and momentum cannot be conserved. Electrons and positrons produce bremsstrahlung radiation as well as ionization along their paths. The electron is eventually absorbed by an ion, while the positron annihilates with an electron. During the annihilation, two new photons are produced: if this happens when the positron is at rest, each photon has an energy equal to 511 keV, one half of its mass. Usually, more than 99% of the photon conversions into pairs are caused by nuclear electromagnetic fields but, for low-Z elements and at high energies, also pair production in the atomic electrons fields contributes significantly to the total cross section. The pair production cross section gradually increases both with Z and E, reaching an asymptotic value near 1 GeV.

In Figure 2.2.3 the energy domains of these processes as a function of the Z value of the absorbing material are shown. The relative importance of the processes through which photons interact depends strongly on the photon energy and on the electron density ($\propto Z$) of the medium. This is well illustrated in Figure 2.2.4, which shows the cross sections for these three processes as a function of energy in carbon (Z = 6, Figure 2.2.4.a), iron (Z = 26, Figure 2.2.4.b) and uranium (Z = 92, Figure 2.2.4.c). Pair production is the most likely process to

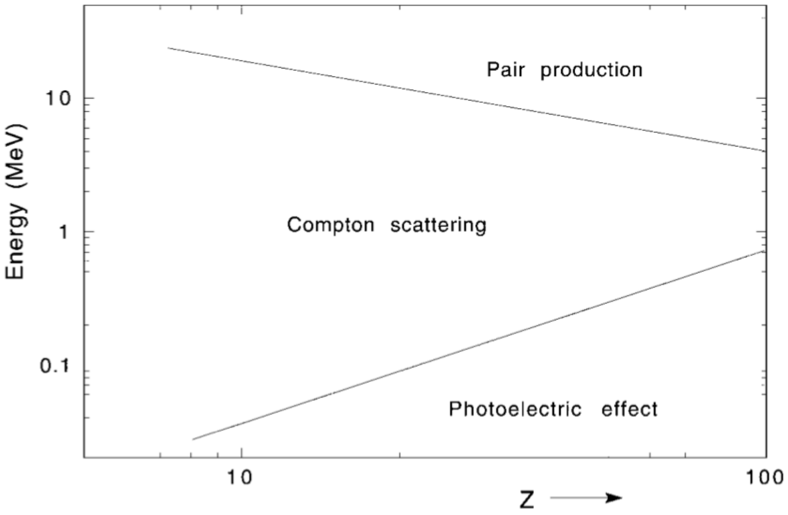

Figure 2.2.3: The energy domains in which photoelectric effect, Compton scattering and pair production are the most likely processes to occur, as a function of the Z value of the absorber material. [41]

occur at high energies, since its cross section increases with energy. Photoelectric process dominates at low energy for high-Z materials while Compton scattering dominates in the low-energy regime for low-Z materials.

Regarding the angular distribution, pair production is characterized by an highly directional distribution, while photoelectrons and Compton electrons are isotropically distributed with respect to the direction of the initial γ.

Photons interact with matter in a completely different way with respect to charged particles. The latter lose energy in a continuous stream of events, ionizing atoms and molecules. For example, considering a multi-GeV electron which traverses one cm of lead, it typically radiates thousands of photons, whom may have energies in excess of 1 GeV, but most of them are very soft, with energies in the eV–keV–MeV range. On the other hand, a multi-GeV photon may penetrate the same thickness of lead without interacts. And, if interacts, may change its identity. In this case, the concept of the mean free path λ, i.e. the mean distance traveled by the particle without suffering an interaction, is used. The probability that a particle interacts, after traveling the distance x is:

$$P_{int}(x) = 1 - e^{-\frac{x}{\lambda}} \tag{2.12}$$

Therefore the probability that the mentioned photon interacts (converts into an e^+e^- pair) in one cm of lead ($\lambda = 7.2\,mm$) is about 75%. This concept has no meaning for electrons, for which the average energy loss can be computed (it is about 83% of electron's energy in this case)

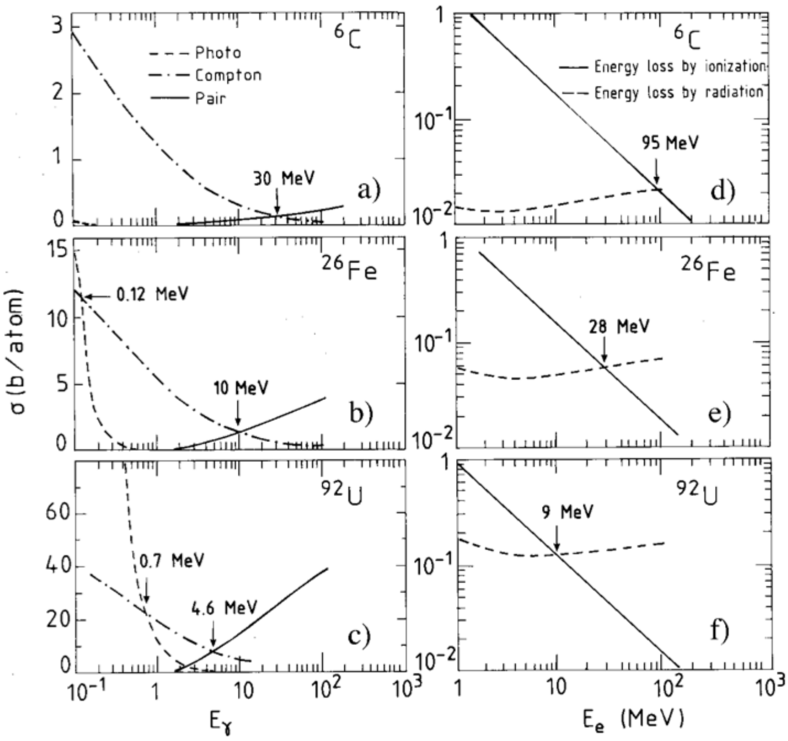

Figure 2.2.4: Cross sections for the processes through which the particles composing electromagnetic showers lose their energy, in various absorber materials. On the left the cross sections for pair production, Compton scattering and photoelectric effect in carbon (a), iron (b) and uranium (c) are shown. On the right, the fractional energy losses by radiation and ionization are given as a function of the electron energy in carbon (d), iron (e) and uranium (f).[41]

[32]. This issue will be treated later, introducing the radiation length of materials.

2.3 THE PHYSICS OF SHOWER DEVELOPMENT

Even if calorimeters are intended to measure energy deposits at the level of 10^9 eV and up, their performance is in practice determined by what happens at the MeV, keV and eV levels. Each particle which interacts in the calorimeter starts a shower, whose characteristics depends on the type and the energy of the primary particle. In particular, showers originated by hadrons and by photon/electron are extremely different and they need to be treated separately.

In the next section the shower development characteristics, the effects of the electromagnetic and strong interactions, and the differences between electromagnetic and hadronic showers are discussed.

2.3.1 *Electromagnetic Showers*

One of the most relevant results of the combined effect of pair production by high energy photons and bremsstrahlung emission by electrons is the formation of *electron-photon showers*. A high energy photon converts in matter into an electron and positron pair which then emit energetic bremsstrahlung photons. These in turn convert in e^+e^- pairs and so on: the result is a cascade of photons, electrons and positrons. This process continues until the energy of electrons and positrons drops below the critical energy: at this point, called the *shower maximum*, the e^+e^- pairs will lose their energy preferentially via atomic collisions rather than bremsstrahlung emission, thus halting the development of the shower.

The development of a cascade is a statistical process and depends strongly on the material, therefore it is convenient to describe its characteristics through quantities which do not depend on Z. The radiation length describes the longitudinal shower development while the Molière radius is the variable used for the lateral shower development.

The radiation length is defined as the distance over which the electron energy is reduced by a factor $1/e$ due to radiation loss only:

$$\left(\frac{dE}{dx}\right)_{rad} = \frac{E}{X_o} \Longrightarrow E = E_0 e^{-\frac{x}{X_0}} \tag{2.13}$$

$$X_0 = \frac{716.4\,A}{Z(Z+1)\,ln(287/\sqrt{Z})}\,g\,cm^{-2} \tag{2.14}$$

This parameter has different meaning for electrons and photons: when high-energy electrons encounter material, they start to radiate immediately while high-energy photons may or may not convert in the same amount of material. Figure 2.3.1 shows the distributions of the energy deposited by 10 GeV electrons and 10 GeV photons on 5 X_0 thick slab of lead. Photons-induced showers deposit their energy deeper inside the absorbing structure and are characterized by a greater spread in the energy loss.

The differences between electron-induced and photon-induced showers have consequences for calorimeter detection of these particles. Indeed, since the performance of electromagnetic calorimeters is almost always determined with beams of electrons, the results may not be valid for γs.

The Molière radius is defined as:

$$\rho_M = 21.2\frac{X_0}{\epsilon_c}\,MeV \tag{2.15}$$

This quantity is frequently used to describe the lateral development of the shower and depends, as given in the relation above, on the critical energy and on the radiation length.

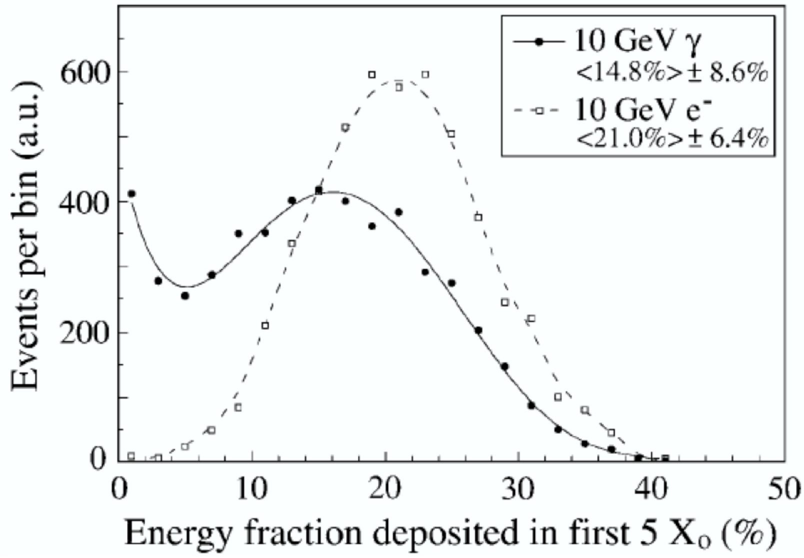

Figure 2.3.1: Distribution of the energy fraction deposited in the first 5 radiation lengths by 10 GeV electrons and gammas showering in lead. Results of EGS4 calculations [42].

The Molière radius scales with Z^{-1} while the radiation length scales with Z^{-2}. Therefore ρ_M is much less material dependent than X_0. For example, copper and lead have almost the same value for ρ_M while their radiation length differ by a factor 3.

A simple model of the shower development assumes $X_0 \backsimeq \lambda_{pair}$, and considers only bremsstrahlung and pair production (symmetric). Following these assumptions, an electron or a photon with initial energy E_0 produces $N \backsimeq 2^t$ particles after t radiation lengths, and the average energy of particles at step t is equal to $E(t) \backsimeq \frac{E_0}{2^t}$.

The number of shower particles produced in this multiplication process reaches a maximum at a certain depth in the absorber (the *shower maximum*) and gradually decreases beyond that depth. The number of shower particles is correlated to the energy deposited and the shower profile as a function of depth is shown in Figure 2.3.2. The depth of the shower maximum increases logarithmically with the energy of the incoming electron and, because of the particle multiplication, the total amount of material needed to contain em showers is relatively small. For example, when 100 GeV electrons enter lead, 90% of their energy is deposited in only 4 kg of material.

Assuming that the particle multiplication phase of the shower stops at the critical energy, the following relations apply:

$$E(t_{max}) = \frac{E_0}{2^{t_{max}}} = E_c \tag{2.16}$$

$$t_{max} = \frac{ln(E_0/E_c)}{ln2} \tag{2.17}$$

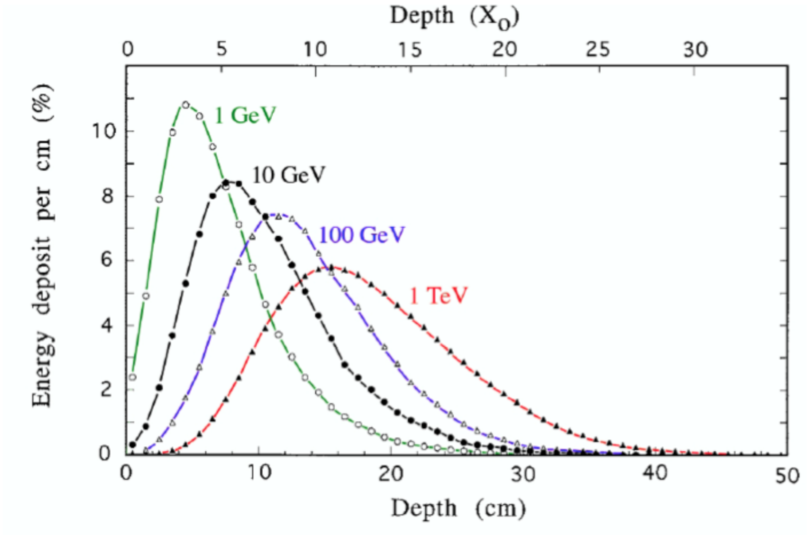

Figure 2.3.2: The energy deposited as a function of depth for 1, 10, 100 GeV electrons in a block of copper. In order to compare the energy deposit profiles, the integrals of these curves have been normalized to the same value. The vertical scale gives the energy deposit per cm of copper as a percentage of the energy of the showering particle. Results of EGS4 calculations [33]

$$N_{max} \approx \frac{E_0}{E_c} \tag{2.18}$$

This is a simple model which gives only a rough qualitative picture of the shower. Monte Carlo simulations allows to make more precise calculation.

It is important to note that most of the energy is deposited by very soft particles, with energy below 1 MeV, as Figure 2.3.3 shows. Accordingly, Compton scattering and photoelectric processes are the most abundant mechanisms, while the pair production occurs only in the early stages of the shower development. As a consequence electrons, which are produced in all the three photon interaction processes, are more abundantly than positrons, except in the very early stages where pair production is dominant.

Usually positrons deposit one quarter of the total em shower energy, while the rest is deposited by electrons. On average, positrons are more energetic respect to electrons and deposit their energy around the shower axis.

The average energy of the shower particles depends on the depth inside the detector: deeper the shower develops, softer is the spectrum. As a consequence, the relative importance of the three different photon interactions changes. In high-Z absorber materials, for example, the photoelectric effect becomes gradually dominant as the shower develops.

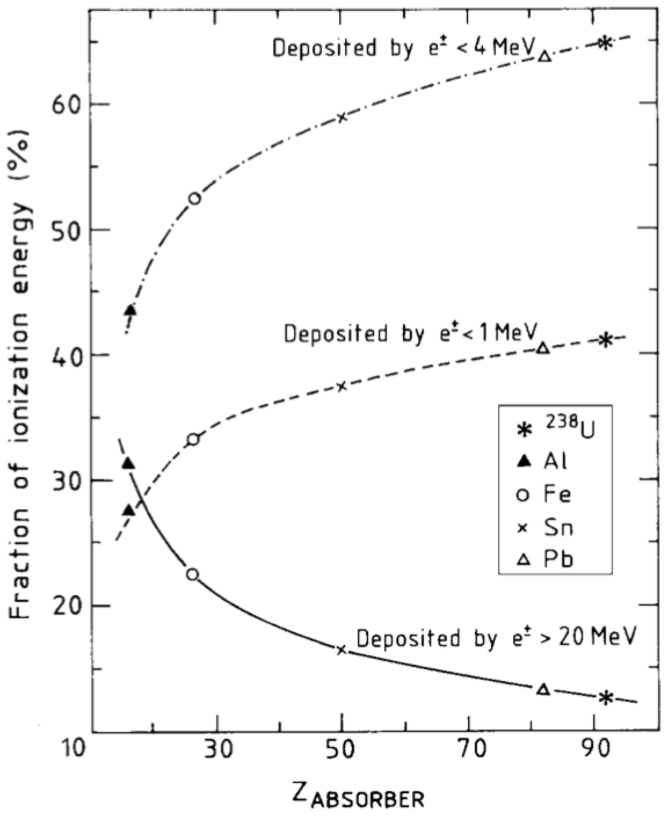

Figure 2.3.3: The composition of em showers. Shown are the percentages of the energy of 10 GeV electromagnetic showers deposited through shower particles with energies below 1 MeV (the dashed curve), below 4 MeV (the dash-dotted curved) or above 20 MeV (the solid curve), as a function of the Z of the absorber material. Results of EGS4 simulations [41].

2.3.2 *Electromagnetic shower profiles and shower containment*

As discussed previously, the shower development depends strongly on the Z of the absorber material. Therefore, the longitudinal and transversal profiles of a shower can be described in term of this parameter and of the initial energy of the showering particle as well.

Not surprisingly, as Z increases, the shower maximum shifts to greater depth and the shower profiles decay more slowly beyond the shower maximum. As a result of these effects, a larger number of radiation lengths is needed to contain a given em shower in lead than in aluminum (as shown in Figure 2.3.4). Even if their longitudinal profiles look very similar, they do not scale perfectly with X_0. This is due to the fact that the particle multiplication continues down to lower energies in high-Z material and decreases more slowly beyond the shower maximum. On the other hand, the multiplication phase continues longer as higher is the initial energy of the showering particle (see Figure 2.3.5).

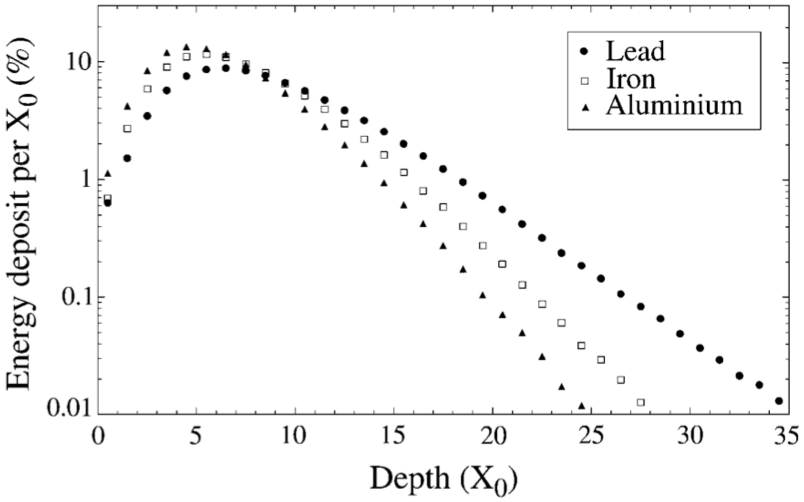

Figure 2.3.4: Energy deposited as a function of depth, for 10 GeV electron showers developing in aluminum, iron and lead, showing approximate scaling of the longitudinal shower profile, when expressed in units of radiation length, X^0. Results of EGS4 calculations [41].

Electron-induced and photon-induced showers are slightly different. Figure 2.3.5 shows that it is necessary about one additional radiation length to contain a γ-induced showers with respect to a electron-induced one of the same energy. For examples, a 20 GeV photon travels, on average, $\frac{9}{7}\ X_0$ before converting into e^+e^- pair of 10 GeV each. This effect does not affect much the shower containment: it takes only an extra 1.3 X_0 to contain twice as much energy, implying a logarithmic energy dependence of the longitudinal shower profiles, as comes out in Figure 2.3.2.

The lateral spread is mostly due to multiple scattering, for which electrons and positrons move away from the shower axis, and to isotropic processes as Compton scattering and photoelectric effect. Bremsstrahlung photons which are emitted by electrons that travel at a considerable angle with respect to the shower axis, may also contribute to lateral spread. Multiple scattering dominates in the late stages of the shower development, while the other mentioned processes prevail in the early stages of the shower development, particularly in high-Z materials. Figure 2.3.6 shows the results of EGS4 Monte Carlo simulations for the radial energy deposited profile in different absorber materials. It appears that the Z dependence is less pronounced compared to the longitudinal case.

The deviations from scaling observed in these figures are caused by phenomena which happen below the critical energy, i.e. Compton scattering and photoelectron production through which at least 40% of the shower energy is deposited. These processes are not properly described by the scaling variables X_0 and ρ_0 since these variables are

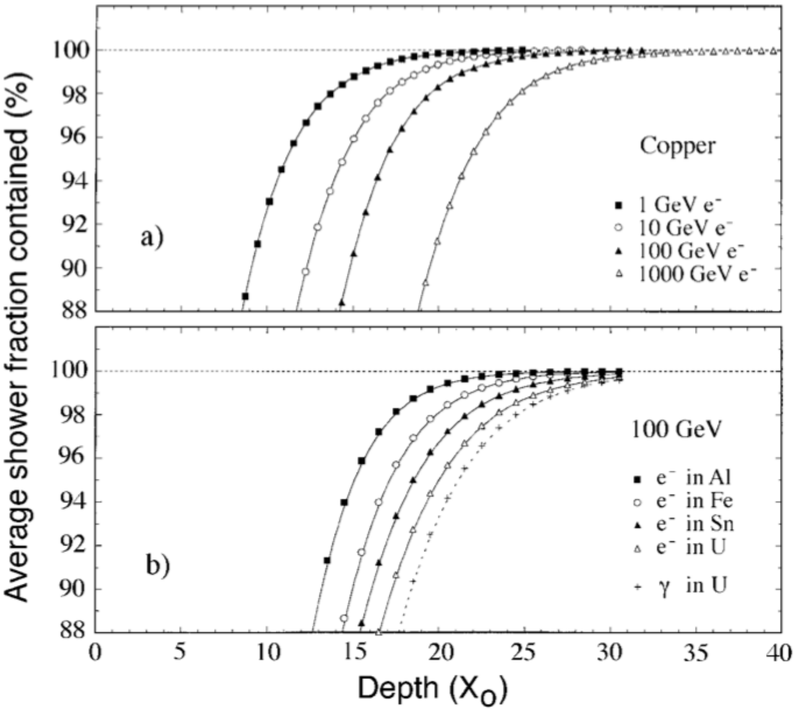

Figure 2.3.5: Average energy fraction contained in a block of matter with infinite transverse dimensions, as a function of the thickness of this absorber. Shown are results for showers induced by electrons of various energies in a copper absorber (a) and results for 100 GeV electron showers in different absorber materials (b). The lower figure also shows the results for 100 GeV γ showers in ^{238}U. Results of EGS4 calculations [41].

defined for the asymptotic energy regime (>1 GeV). Another feature of these particles is that they deposit energy isotropically, as it is visible in Figure 2.3.7. This feature has an important consequence: the active layer in a sampling calorimeter can be oriented as desired, without any implications for the calorimetric performance. *Sandwich type* calorimeters, i.e. sampling calorimeters composed of alternating layers of absorber and active material oriented perpendicular with respect to the beam line, are not the only possible geometry for sampling calorimeters. On the contrary other orientations may be better in term of hermeticity, granularity, etc. The range of 1 MeV electrons, typical particles involved in Compton scattering, is about 1 mm in typical absorber materials, such as iron and lead. This value sets the scale for useful distance between active layers in a sampling em calorimeter.

2.3.3 *Hadronic showers*

In the case of hadronic showers, strong interactions between the shower particles and the nuclei of the absorbing medium play also an important role. The variety of processes which may occur is larger

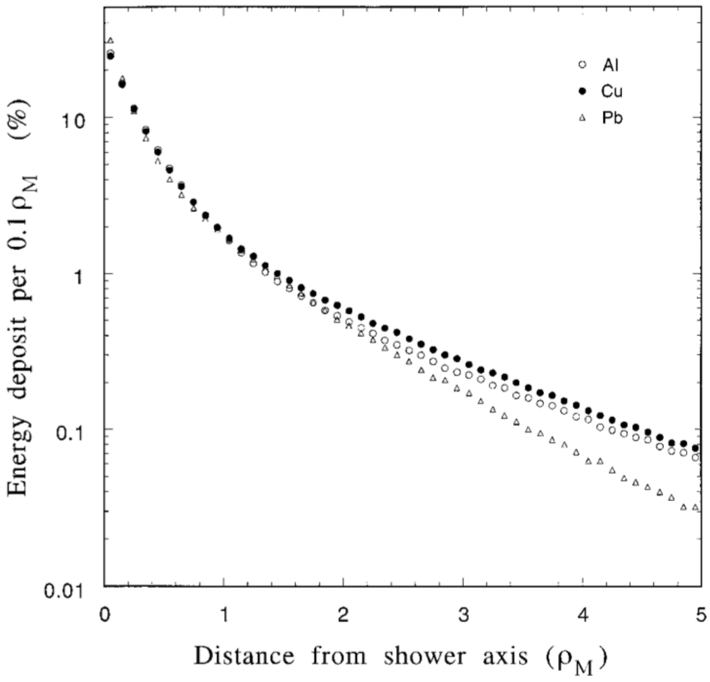

Figure 2.3.6: Radial profiles of energy deposited for 10 GeV electrons showering in aluminum, copper and lead. Results of EGS4 calculations [41].

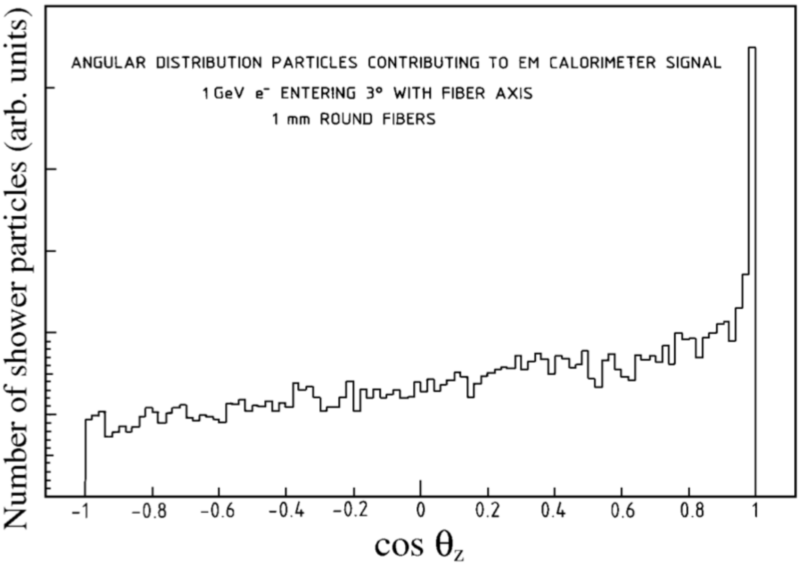

Figure 2.3.7: Angular distribution of the shower particles (electrons and positrons) through which the energy of a 1 GeV electron is absorbed in a lead-based calorimeter. Results of EGS4 Monte Carlo simulations. From [6].

and so the discussion of the hadronic showers is more complex than the one of electromagnetic showers.

In the case of a charged hadron, the medium will be ionized in a continuous stream of events. At some depth the hadron encounters an atomic nucleus with which it interacts strongly. In nuclear reactions hadrons change their identity and the reaction products could be tens of hadrons. The struck nucleus changes too, loosing nucleons and, being left in an excite state, will decay by emitting several γ-rays.

Many of the neutral hadrons produced in an hadronic cascade decay through electromagnetic interaction: π^0's and η's decay in 2 γ's, which in turn develop em showers. Other neutral hadrons do not ionize the medium: the only type of interaction that they may undergo is the nuclear one. In particular, in hadronic shower development neutrons are abundantly produced. They lose energy in very different way with respect to those of charged hadrons, and this is an important aspect to consider in order to understand hadronic calorimetry. Indeed, in order to release neutrons and protons from atomic nuclei, the binding energy has to be provided. The energy used for this purpose does not contribute to the calorimeter signal, and so it is called invisible energy.

As for em showers, secondary particles may in turn ionize the medium and/or undergo nuclear reactions and so on, producing an hadronic shower. In the early stages of the shower the multiplication process increases the number of particles until the shower maximum is reached, i.e. where further multiplication is balanced by the absorption of shower particles. Beyond this maximum, the energy deposit by the shower particles gradually decreases.

Despite these similarities with the em showers, there are important differences between the two types of shower. First of all the scale of the hadron shower development is larger than the em one. The scale variable which describes the hadronic shower profiles is the *nuclear interaction length* (λ_{int}): the average distance an hadron travels before inducing a nuclear interaction. It is defined as for the mean free path of high-energy photons. The probability that a particle traverses a distance z in the medium without interacting with a nucleus is:

$$P = e^{(-z/\lambda_{int})} \tag{2.19}$$

where λ_{int} is inversely proportional to the total cross section for nuclear interactions:

$$\sigma_{tot} = \frac{A}{N_A \lambda_{int}} \tag{2.20}$$

The size of projectiles and the size of target determine this cross section. Since both depend on the A value, it follows that λ_{int} scales with $A^{-1/3}$ when expressed in units of g/cm^2 [41]. Hadronic shower profiles, on average, look like the em ones even if the scale factor is much larger. For example, for copper X_0 is equal to 1.4 cm while λ_{int} is equal to 15 cm.

In the following sections the different components of an hadronic showers and their properties are discussed.

2.3.3.1 *The electromagnetic component*

The fraction of the hadronic shower which propagates electromagnetically fluctuates strongly event by event and it is called the *electromagnetic fraction*, f_{em}.

On average, 90% of the hadronic shower particles are pions and one third of them are π^0s. Neutral pions decay to two photons with a branching ratio of about 100% and may be produced by shower particles until these are sufficiently energetic. Moreover, since the π^0s production is an irreversible process, the f_{em} gradually increases with energy.

A simple model to estimate the average electromagnetic fraction assumes that all available shower energy is used to produce mesons, and one third of the mesons produced in nuclear reactions consists of neutral pions. After n generation of the shower development f_{em} is:

$$f_{em} = 1 - (1 - \frac{1}{3})^n \tag{2.21}$$

The non-electromagnetic content of the shower decreases as $(1 - 1/3)^n$ and after each interaction, $(1 - 1/3)$ of the remaining energy is available for the next generation of collisions. The number of generation n is a function of the energy E of the particle that initiates the shower. If the total number of mesons produced is assumed to be proportional to E and to the multiplicity $<m>$, i.e. the average number of mesons produced per interaction, the f_{em} scales according to the Equation 2.21.

This simple model does not take into account that other particles are produced in an hadronic shower, not only charged and neutral pions. Then the factor 1/3 in Equation 2.21 should be considered an upper limit, and will be called f_{π^0}. Moreover $<m>$ depends on the energy E: in particular, the average number of mesons produced in a reaction increases logarithmically with the energy. Finally, this model neglects the energy loss by ionization and nuclear excitation of the calorimeter media, which depends on Z-value of the material, and the conservation of the baryon number.

A more precise model has been studied by Gabriel *et al.* [26]. The resulting expression for the electromagnetic fraction is

$$f_{em} = 1 - \left(\frac{E}{E_0}\right)^{(k-1)} \tag{2.22}$$

where E_0 is a scale factor, which corresponds to the average energy needed for the production of one pion, and the exponent *(k-1)* is related to $<m>$ and f_{π_0} through the relation below:

$$1 - f_{\pi^0} = < m >^{(k-1)} \rightarrow k = 1 + \frac{ln\,(1 - f_{\pi^0})}{ln < m >} \qquad (2.23)$$

The exponent k defines the energy dependence of the em shower fraction, since it is determined by two parameters: the average fraction of π^0 production per nuclear interaction f_{π^0}, and the average multiplicity per nuclear interaction, $<m>$.

Gabriel and his collaborators have studied these relations and their parameters using simulated data on hadronic shower development in different absorber materials and they arrived to several conclusions:

- E_0 depends on the Z of the traverse medium;
- the f_{em} in proton-induced showers is much smaller than for pion-induced showers of the same energy.

This last phenomenon has a simple explanation. In pion-induced showers there is no requirement of the baryon number conservation, which limits the π_0 production in proton-induced shower. Therefore pion-induced showers contain a larger em component.

The Z dependence instead lies in the ionizing mechanism of the medium by charged hadrons since the amount of energy lost in this way depends strongly on Z. As the energy loss per hadron increases, the number of hadrons produced in the shower development decreases. So E_0 increases and the number n and the em shower fraction f_{em} decrease. These predictions were supported experimentally by the SPACAL [8] and the QFCAL Collaboration [13], whom have attempted to measure the electromagnetic fraction of the hadronic showers developing in their detectors. For example, in Figure 2.3.8 are shown the results obtained by the SPACAL Collaboration. The curves in this figure correspond to calculations based on Equation 2.22, using a value $E_0 = 1.3$ GeV, recommended by Gabriel *et al.* for lead, the absorber material of the SPACAL detector. The parameter k was varied in these calculations and the three curves represent results for k = 0.80, 0.82 and 0.84, respectively. The experimental data favor k = 0.82.

2.3.3.2 *The nuclear sector*

Typical shower particles in hadron showers are 50-100 MeV spallation protons, 3 MeV evaporation neutrons and charged pions.

Charged hadrons, before interacting with a nucleus, ionize the medium and may lose a significant amount of energy, especially if they are soft hadrons produced in the cascade.

Pions may interact with a nucleus too, but since they are only 2/3 the size of protons, they have a smaller probability of encountering a nucleus and so they travel typically 25-50% more distance before a nuclear interaction can occur.

On the average, the 80% of the energy of the non-em component is available for exciting and dissociate the medium nuclei.

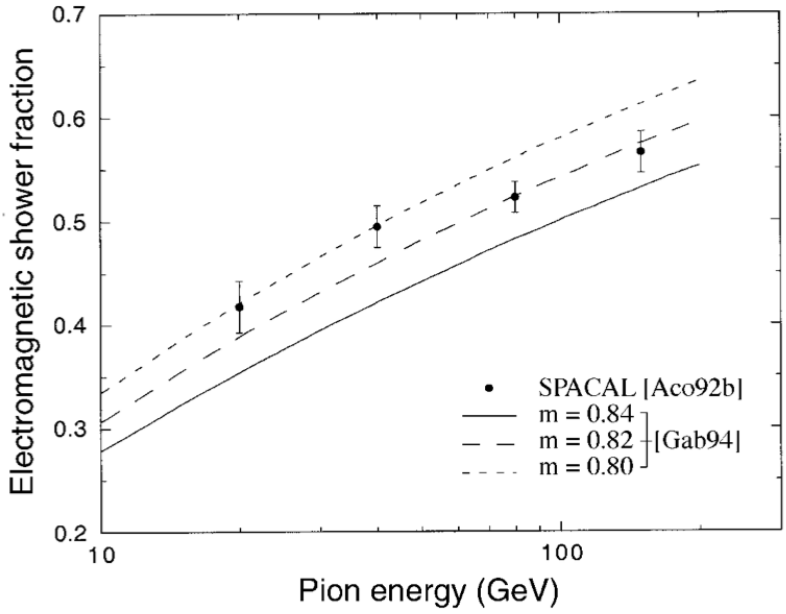

Figure 2.3.8: The average em shower fraction in pion-induced showers measured in the SPACAL lead/fiber calorimeter. The curves represent predictions based on Equation 2.22. Experimental data from [8].

The process more likely to occur is spallation. This reaction can be described as a two-step process: the incoming high energy hadron strikes the nucleus generating a fast intranuclear cascade, and then the excited nucleus decays by emitting nucleons or nucleon aggregates. The de-excitation of the nucleus is called the evaporation stage. The emission of nuclei continues until the excitation energy is smaller then the binding energy of the nucleon. The remaining energy, typically few MeV, is released as γ-rays. Taking into account a given nucleus, struck by an hadron of a certain energy, the variety of possible spallation reactions is huge.

The nuclear binding energy which is provided by shower particles to release nucleons in the spallation process, does not produce any calorimeter signal, and so it is called invisible energy. Since the variety of processes which may occur is very large, the invisible energy fluctuates strongly event by event and it is one of the factors which limit the energy resolution of an hadronic calorimeter. Anyway it is possible to exploit the correlation between the binding energy loss and the kinetic energy carried by the nucleons in order to estimate the invisible energy, as will be discussed later.

In the Table 2.3.1 both the energy deposited and the composition of the non-em component of an hadronic shower in lead and iron are reported.

The discrepancy between the number of protons and neutrons released is due to several factors. Protons are emitted mostly by the

	Lead	Iron
Ionization by pions	19%	21%
Ionization by protons	37%	53%
Total ionization	56%	74%
Nuclear binding energy loss	32%	16%
Target recoil	2%	5%
Total invisible energy	34%	21%
Kinetic energy evaporation neutrons	10%	5%
Number of charged pions	0.77	1.4
Number of protons	3.5	8
Number of cascade neutrons	5.4	5
Number of evaporation neutrons	31.5	5
Total number of neutrons	36.9	10
Neutrons/protons	10.5/1	1.3/1

Table 2.3.1: The energy deposit and the composition of the non-em component of hadronic showers in lead and iron is reported. The listed numbers of particles are per GeV of non-em energy [41].

nucleus in the cascade-step while in the evaporation process almost all nucleons emitted are neutrons. This is in particular true for lead, which is characterized by a Coulomb barrier for protons equals to 12 MeV. Since in the evaporation stage nucleons are released with a kinetic energy of few MeV, it is difficult to find charged particles coming out from the nucleus. Concerning the nuclear binding energy loss, the great difference between the two materials is due to the fact that iron is the most stable nucleus in nature and it is thus characterized by a very high binding energy.

The neutron/proton asymmetry is greater in lead than in iron, and this is due to the higher Coulomb barrier in lead, and to the different proton/neutron ratio in the nuclei. Indeed in lead (Z/A=82/108), 39% of the energy carried by spallation nucleons is brought by protons, while in iron (Z/A=26/56) this fraction amounts to 46% [41]. Since the kinetic energy of escaping protons is lost by ionization, a larger fraction of the energy is contained in the lead nuclei and will be later released in the form of evaporation neutrons.

Table 2.3.1 also contains other features:

- charged pions have a minor role with respect to protons in the absorption process;

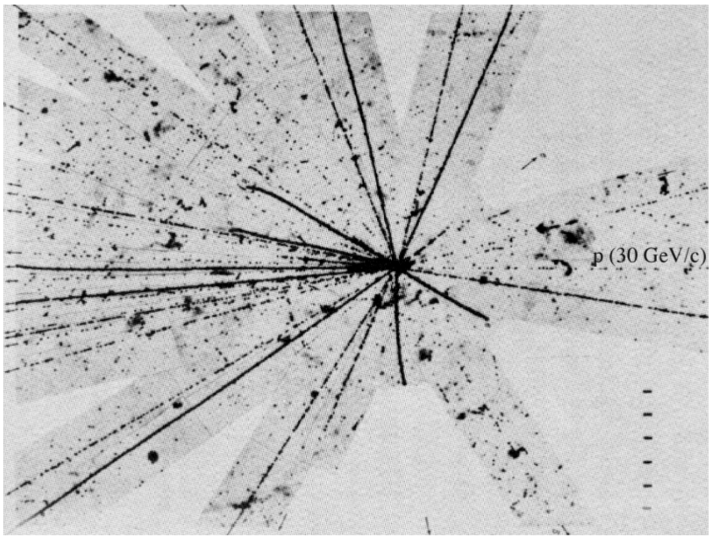

Figure 2.3.9: A proton-nucleus interaction in a nuclear emulsion stack. Photograph courtesy CERN.

- soft spallation protons have a major role in the absorption process, since about 40% of the non-em energy is deposited through them;
- the fraction of invisible energy is very large;
- a significant part of the hadronic shower energy is carried by a large number of soft neutrons.

Finally, it is important to point out that there is another contribution to the invisible energy: the kinetic recoil energy of the struck nucleus in the spallation process. Indeed, as it is shown in Figure 2.3.9, spallation protons and neutrons are likely to be emitted along the direction of the projectiles and thus the nucleus recoils. This recoil energy is usually too small to generate a signal, and so it contributes to the invisible energy.

2.3.4 *Hadronic shower profiles*

As mentioned before, the longitudinal profile of an hadronic shower is very similar to the one of an em shower, except for the scale: the hadronic showers develop deeper in the absorber medium since the nuclear interaction length is larger than the radiation length, up to a factor of 30 in high-Z materials, as is shown in Figure 2.3.10. The difference in the scaling variables allows to distinguish between the two type of showers easily. For example, a pre-shower detector, i.e. a slice of lead followed by a sheet of plastic scintillator positioned in front of the calorimeter, can be used to do this task. Pions release only a very small fraction of their energy in it while electrons will start a

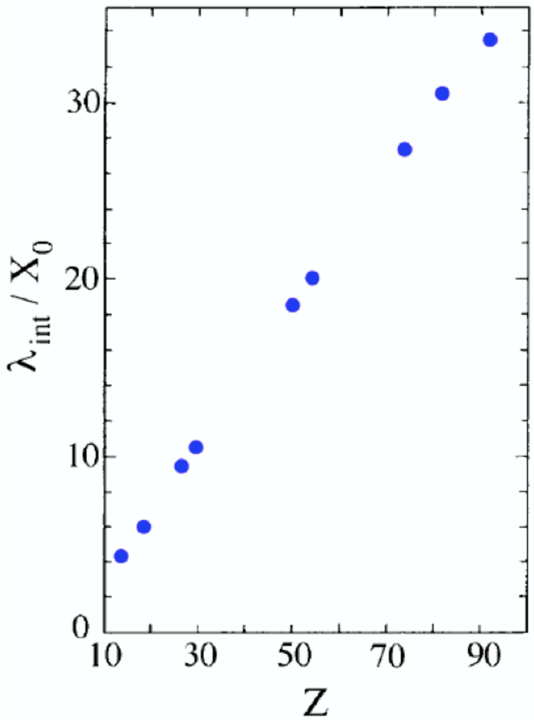

Figure 2.3.10: Ratio of the nuclear interaction length λ_{int} and of the radiation length X_0 as a function of Z [33].

shower: the two energy distribution will be thus very different (see Figure 2.3.11).

The depth of an hadron calorimeter needed to contain the shower increases logarithmically with the shower energy, as for em showers. But, since the scale of the two types of showers is different, the containment of an hadronic shower will require more material with respect to the containment of an em shower of the same energy (at least for materials with Z>10).

An hadronic shower is also broader: the lateral profile shows in general a narrow core, which corresponds to the em component, surrounded by a large halo, as is visible in Figure 2.3.12. Since the electromagnetic fraction of the shower increases with energy, high-energy showers develop more close to the shower axis than low-energy ones and will be contained laterally in a smaller cone. The non-em component of the shower is instead responsible for the halo, which decays exponentially with the distance from the shower axis.

The ZEUS collaboration has measured the lateral profiles at different depths in their uranium/plastic-scintillator calorimeter, with a 100 GeV pions beam [10]. Their results are shown in Figure 2.3.13: in the early stages of the shower development the em shower core is prominent while beyond 4.5 λ_{int} it is completely disappeared.

The shower profiles shown until now were averaged over a large number of showers. But the hadronic shower profiles are very different

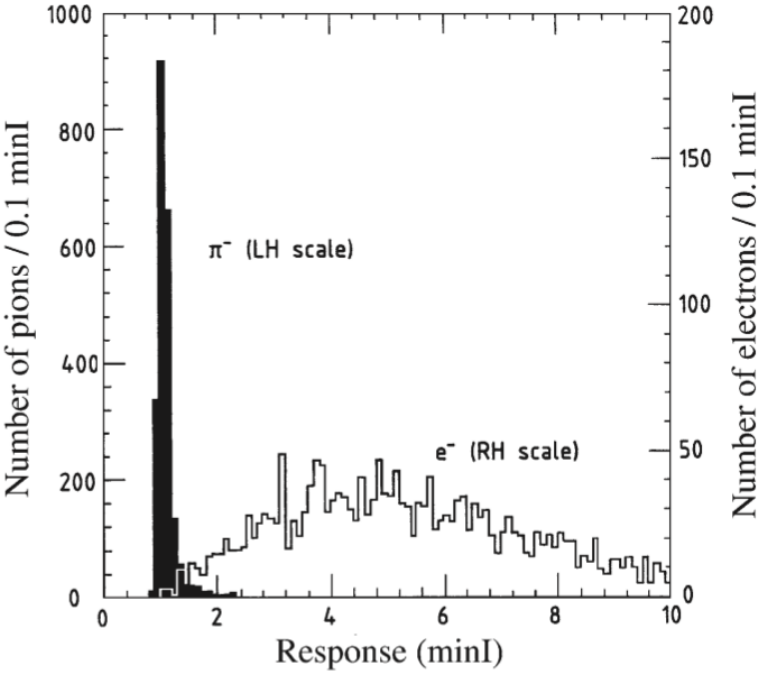

Figure 2.3.11: Signal distributions for 75 GeV π^- and e^- in a very simple pre shower detector.[33]

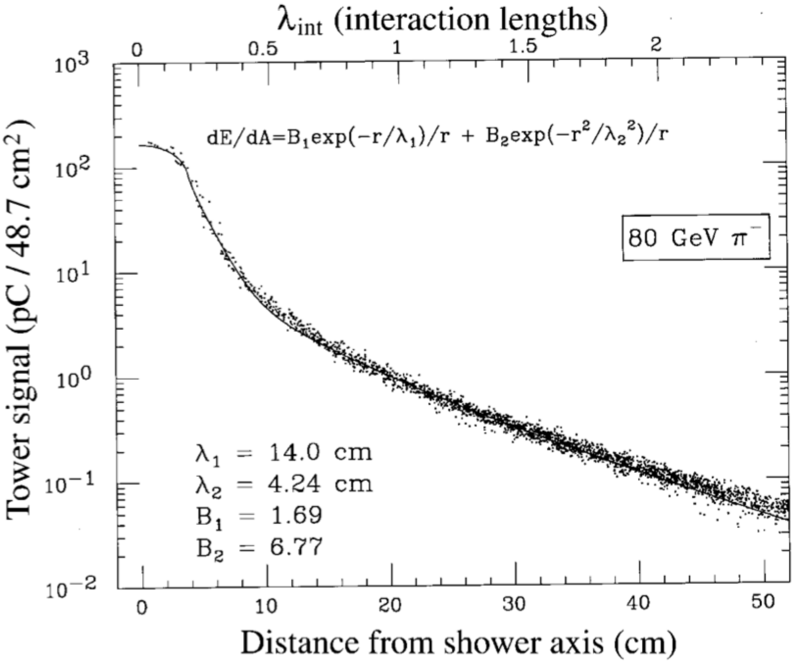

Figure 2.3.12: Average lateral profile of the energy deposited by 80 GeV π–showering in the SPACAL detector. The collected light per unit volume is plotted as a function of the radial distance to the impact point. Data from [8].

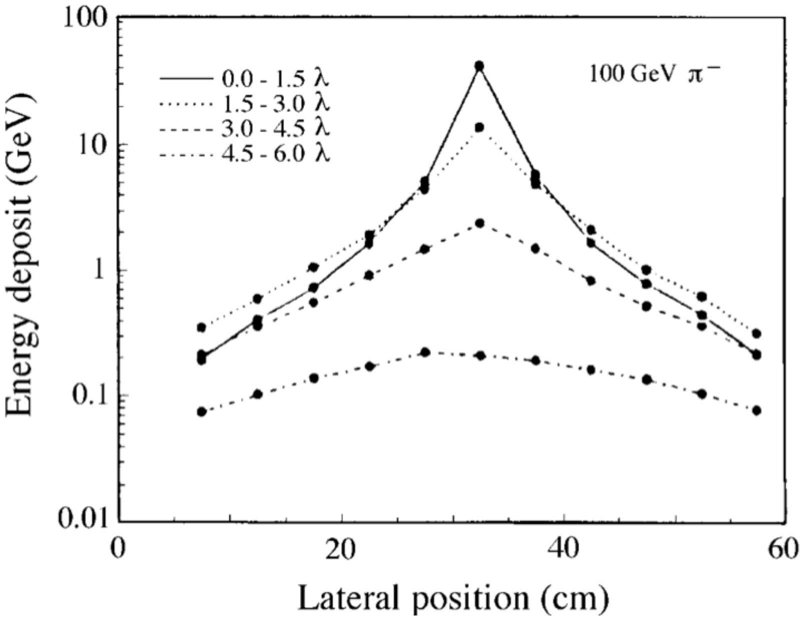

Figure 2.3.13: Lateral profiles for pion-induced showers, measured at different depths, with the ZEUS calorimeter. Data from [10].

from each other and this is primarily due to the π^0-induced showers. The production of energetic π^0s may indeed occurs in different regions of the absorbing volume and so the energy deposit profiles will differ considerably from the average. Some examples are shown in Figure 2.3.14: the energy is deposited through one or several π^0s in the second or third generation of the shower development. The profiles shown in Figure 2.3.14 are not exceptional in hadronic shower development, since π^0s deposit their energy in a smaller volume than other shower particles. These profiles reflect the event by event fluctuations in the energy carried by π^0s and in the position in which they deposit energy. Figure 2.3.15 shows instead six examples of electromagnetic shower profiles. As it is clearly visible, they are very similar to each other, unlike pions ones.

The typical particles in hadron showers are 50-100 MeV spallation protons and 3 MeV neutrons. The proton range at these energies is about 1 cm, while 3 MeV evaporation neutron range is typically longer, since neutrons may travel several centimeters between two interactions. Indeed, neutrons deposit their energy only through nuclear interactions. They can undergo elastic and inelastic scattering with the nuclei, or be captured. The last process may occur when neutrons have lost almost all their kinetic energy, i.e. when neutrons are thermalized.

The measurement of their kinetic energy can be fundamental in the case of sampling calorimeters. By choosing proper active and passive materials, the contribution of neutrons to the calorimeter signals can be large, and its measurement allows to estimate the invisible energy, as will be discussed later.

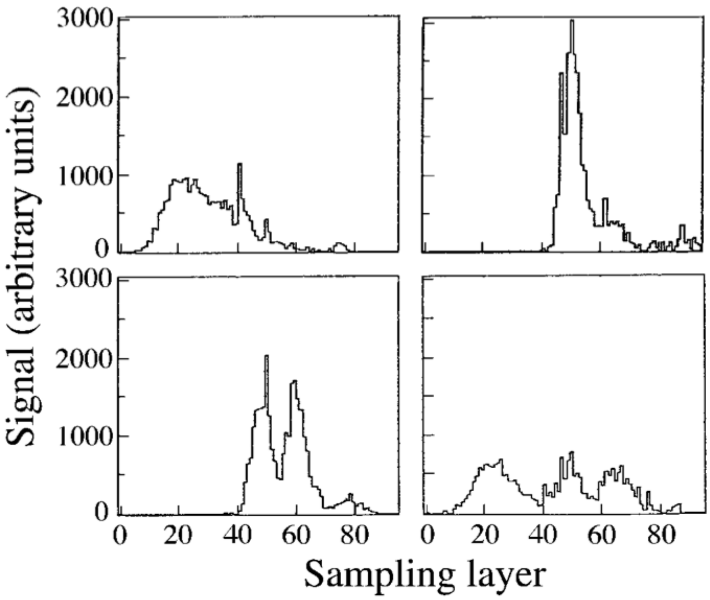

Figure 2.3.14: Longitudinal profiles for 4 different showers induced by 270 GeV pions in a lead/iron/plastic-scintillator sandwich calorimeter: the absorber structure consists of 40 lead plates (3.1 mm thick), followed by 20 iron plates (2.5 cm thick). Data from [29]

Evaporation neutrons dominate the tail of the longitudinal and lateral shower profiles because of their long mean free path. Calorimeters which exploit neutron signals have thus to integrate over a large volume and also a long time.

2.4 THE CALORIMETER RESPONSE FUNCTION

As can be derived from previous discussion, the physics of shower development is complex. Accordingly, calorimeters, especially the hadronic ones, are non-trivial instruments. In this section the energy response of calorimeters, fluctuations and instrumental aspects will be discussed, in order to have a better comprehension of these devices.

The calorimeter response is defined as the *average calorimeter signal divided by the energy of the particle that generates it*.

A calorimeter is linear when its response is constant as a function of energy. The units through which the calorimeter response is expressed are the number of photoelectrons per GeV, picoCoulomb per MeV or similar, depending on the calorimeter system.

The calorimeter response to different types of particles is often compared, and *mips* (minimum ionizing particle) represent the "benchmark particles". The response of a calorimeter to a particle X is thus expressed as the ratio X/mip, i.e. the calorimeter response to particle X over the calorimeter response to *mip*.

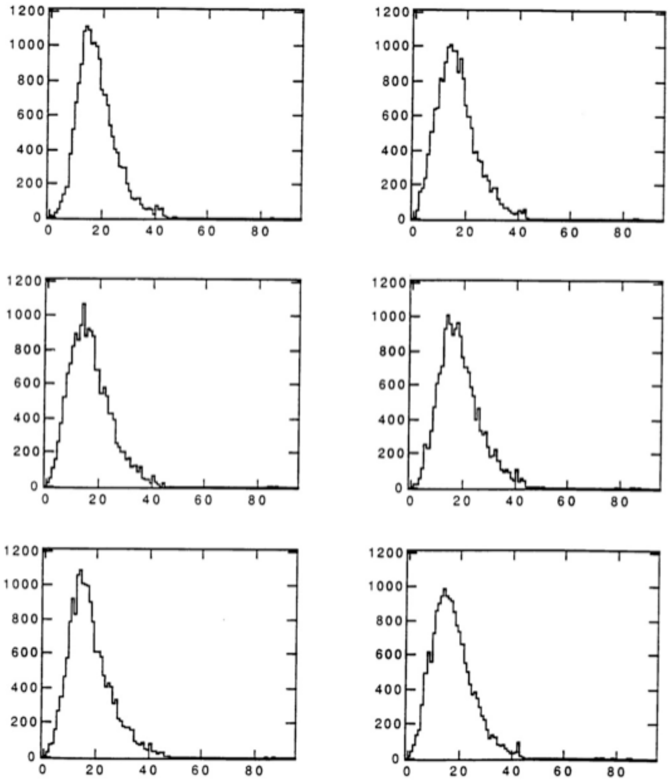

Figure 2.3.15: Longitudinal profiles for 4 different showers induced by 170 GeV electrons in a lead/iron/plastic-scintillator sandwich calorimeter: the absorber structure consists of 40 lead plates (3.1 mm thick), followed by 20 iron plates (2.5 cm thick). Data from [29]

The response to mips cannot be measured directly since they are hypothetic particles. Charged particles can be considered mips when their stopping power reaches its minimum value but as soon as they lose energy again, they cease to be mips. The particles which can be considered mips are muons, even if at relativistic energies their energy loss is greater than the minimum value.

One way to determine the experimental calorimeter response to mips is to measure the signals produced by muons at different energies and then extrapolate the mip part of the signals.

The best way to evaluate the calorimeter response is to plot it versus energy (as in Figure 2.4.1). Indeed, this method is highly sensitive to small non-linearities. Electromagnetic calorimeters are in general linear, since all the energy deposited by em showers generates signals.

Deviations from linearity may be observed, and are usually an indication of instrumental problems. Indeed these deviations can be due for example to:

- saturation effects in PMTs, which can be solved lowering the PMT gain (as Figure 2.4.1 shows);

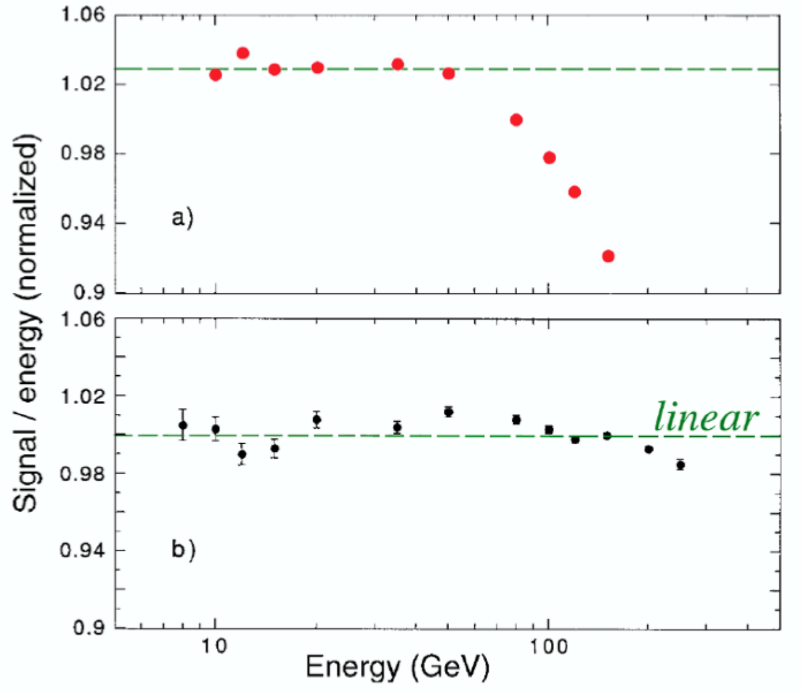

Figure 2.4.1: The electromagnetic calorimeter response as a function of energy, measured with the QFCAL calorimeter, before (a) and after (b) precautions were taken against PMT saturation effects. Data from [13].

- saturation in gaseous detectors operating in "digital" mode, which are characterized by a response depending on the particle density;
- shower leakage;
- recombination of ions and electrons in the medium.

This effects cause the calorimeter response to decrease with energy.

On the contrary, signal non linearity is a very common feature for hadron calorimeters, given the energy dependent em shower fraction and the invisible energy phenomenon.

In non-em shower component the energy is carried by mesons, spallation protons, evaporation neutrons, recoil target nuclei, nuclear γs and it is lost in release nuclei. The response of calorimeter to this non-em component is indicated as h, while the response to the em component is called e.

The calorimeter response to the hadronic component of a shower can be expressed as:

$$h = f_{rel} \cdot rel + f_p \cdot p + f_n \cdot n + f_{inv} \cdot inv \qquad (2.24)$$

where f_{rel} is the fraction carried by relativistic charged pions, f_p is the fraction carried by spallation protons, f_n is the fraction carried by evaporation neutrons and f_{inv} is the fraction due to the invisible energy. *rel, p, n, inv* are the calorimeter responses for the mentioned components. Normalizing all of them to the one for mips, and knowing that *inv* = 0, one obtains:

$$\frac{e}{h} = \frac{e/mip}{f_{rel} \cdot rel/mip + f_p \cdot p/mip + f_n \cdot n/mip} \tag{2.25}$$

In Table 2.3.1 the indicative values for the fraction of all the non-em components are reported.

Charged pions behave like mips at low energies, well below 1 GeV. As their energy increases, nuclear reactions start play an important role and π^0s are produced widely.

Since π^0s generate em showers, the response to pions gradually becomes similar to the one for em showers, as the energy increases.

The e/h value cannot be directly measured. One method to indirectly measure the e/h ratio, knowing the electromagnetic fraction f_{em} is given below:

$$\pi = f_{em} \cdot e + (1 - f_{em}) \cdot h \tag{2.26}$$

$$\pi/e = f_{em} + [1 - f_{em}] \cdot h/e \tag{2.27}$$

which leads to

$$e/\pi = \frac{e/h}{1 - f_{em}\,[1 - e/h]} \tag{2.28}$$

This relation is depicted in Figure 2.4.2 for a number of e/h values. To derive this relationship, the ratio e/π has to be measured and the energy dependence of the f_{em} has to be known (see Equation 2.22). The figure clearly shows that the e/π signal ratio approaches 1, in the limit of high energies, despite the e/h value.

The signal non-linearity is determined by the e/h value. Assuming that the calorimeter is linear for em shower detection, from Equation 2.27 follows that the ratio of pion responses at energies E_1 and E_2 is related to e/h:

$$\frac{\pi(E_1)}{\pi(E_2)} = \frac{f_{em}(E_1) + [1 - f_{em}(E_1)]\,(e/h)^{-1}}{f_{em}(E_2) + [1 - f_{em}(E_2)]\,(e/h)^{-1}} \tag{2.29}$$

If e/h =1, this ratio is equal to 1 too, and the calorimeter is thus linear. The same situation holds for jets. Jets consist of collection of particles, resulting from quark fragmentation or hard gluons produced in the collisions. The four-vector of a jet reflects the four-vector of the fragmenting (di)quark. Its measurement is thus more important than the measurement of all individual hadrons.

The shower generated by a jet, contains an em component as the hadronic showers do. The only difference is that jets usually contain already a number of π^0s before entering the calorimeter and so they

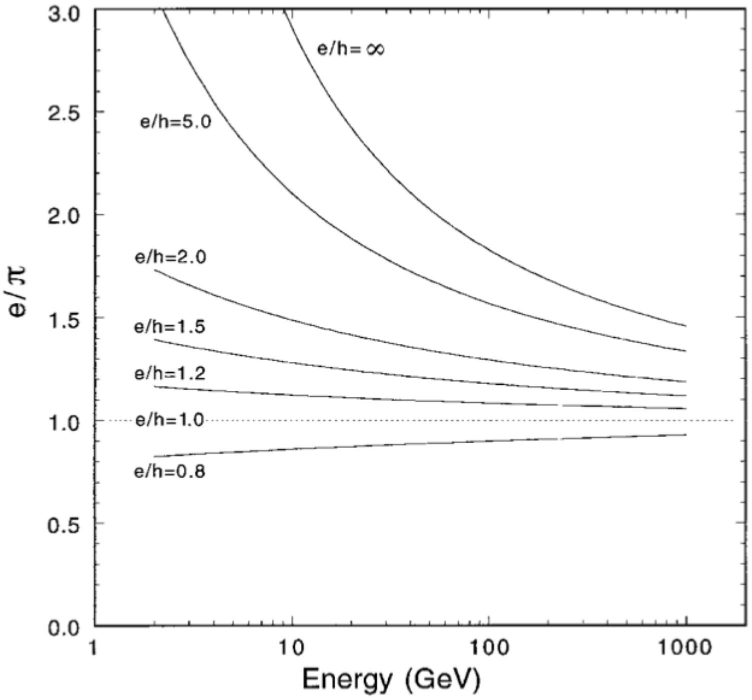

Figure 2.4.2: The e/π signal ratios as a function of energy, for different values of e/h.[41]

have an "intrinsic" electromagnetic component. Besides, the average f_{em} of jet shower may be different from that of an individual hadron shower. The reason lies in the fragmentation process. In the case of a diquark fragmentation, the leading particle is a baryon while in the case of a quark fragmentation, the leading particle is a meson. Since the conservation of the baryonic number, heavy quarks (c, b) may likely to produce light quarks (u, d) than neutral pions. Anyhow, the calorimeter response for jets is smaller than that for electrons, photons and muons and it is energy dependent.

2.4.1 *Homogeneous calorimeters*

In this type of calorimeters, all the volume is sensitive to the particles and may contribute to the production of the signal.

Homogeneous calorimeters are intrinsically linear for em showers, except for saturation and instrumental effects as discussed below. They are thus characterized by

$$^{e}/_{mip} = 1 \tag{2.30}$$

because of similarities between the energy deposit mechanisms of muons and electrons. As a consequence, if the calorimeter is calibrated with electrons, i.e. the relation between the calorimeter signal and the deposited energy is found with electron of known energy, the calibration constant can be exploit to determine also the energy deposited by muons.

Obviously, the calibration constant cannot be used for hadrons and jets, since they lose energy in a wide variety of processes and not all the energy deposited generates a measurable signal (invisible energy phenomenon). Homogeneous calorimeters are thus all characterized by $e/h > 1$ and therefore they are non-compensating devices (see Section 2.4.3).

For this reason, these calorimeters are never used as hadronic devices since there are no possible methods in order to make them compensating. On the contrary, homogeneous calorimeters can be exploited as the em section of a calorimeter. In this case, the hadronic performance of the combined system is anyway affected by the fact that the em section is highly non compensating. As a consequence, in this case it is not worth to build a very good hadronic section.

2.4.2 *Sampling calorimeters*

Sampling calorimeters are made of two different materials, one which has the function of absorbing particles energy, and one which generates the calorimeter signal.

One important parameter which characterizes these devices is the *sampling fraction*. It is defined as the energy deposited by *minimum ionizing particles* (mip) in the active calorimeter layers, with respect to the total energy deposited by such particles in the whole calorimeter.

2.4.2.1 *The sampling calorimeters response to electrons and photons*

In sampling calorimeters the e/mip value is generally far from one, and depends strongly on the Z-value of both the absorber and the active material. The larger is the difference between the Z of the two media, the smaller is the response to em showers. This effect has been under study for many years, and it has become known as the *transition effect*.

The reason why the response to em showers is suppressed in sampling calorimeters is due to how low-energy γs and electrons (< 1 MeV) interact with matter. Their range is much shorter than the typical thickness of the absorber layers. Therefore the sampling of these electrons is very inefficient, since only those who interact near the boundary between the passive and the active media, will enter the active material and therefore contribute to the signals. In high-Z materials, these soft electrons are produced through the photoelectric effect, whose cross section has a Z^5 dependence. The most part of the soft photons thus interact only in the absorber and this causes the low e/mip value.

As the energy resolution, also the em sampling fraction is heavily affected by phenomena which occur at energies 10^4 smaller than the incident particle ones. This effect causes also a dependence of the

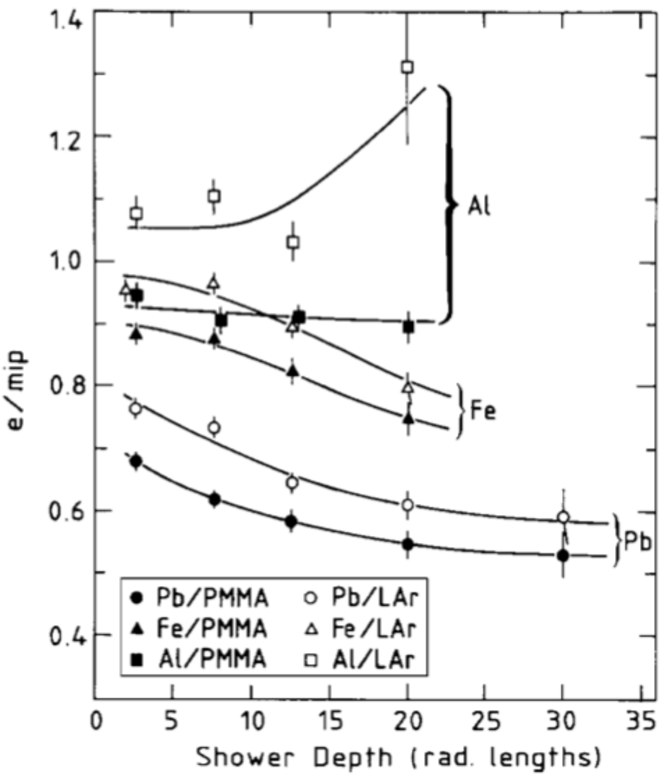

Figure 2.4.3: The e/mip ratio as a function of the shower depth, or age, for 1 GeV electrons in various sampling calorimeter configurations. All calorimeters consist of 1 X_0 thick absorber layers, interleaved with 2.5 mm thick PMMA or LAr layers. Results from EGS4 Monte Carlo simulations [39].

sampling fraction from the age of the shower, i.e. the depth, as it is visible in Figure 2.4.3. Soft γs are absorbed by Compton scattering and photoelectric effect especially in the last stages of the shower development, and the deviations from $e/mip = 1$ is due to them. This feature has important consequences for the calibration of longitudinally segmented sampling calorimeters. The calibration constants, i.e. the coefficients which relate signals to energy deposits, have to be different for the different sections.

However, if the sampling frequency is increased, i.e. the layers are made thinner, the sampling fraction increases as well since the total boundary surface increases. This effect was studied with EGS4 simulations, as the other mentioned effects. The results are shown in Figure 2.4.4, for uranium calorimeters with PMMA (Polymethylmethacrylate) or LAr readout.

2.4.2.2 *The sampling calorimeter response to hadrons*

Most of the sampling hadron calorimeters are intrinsically non-linear.

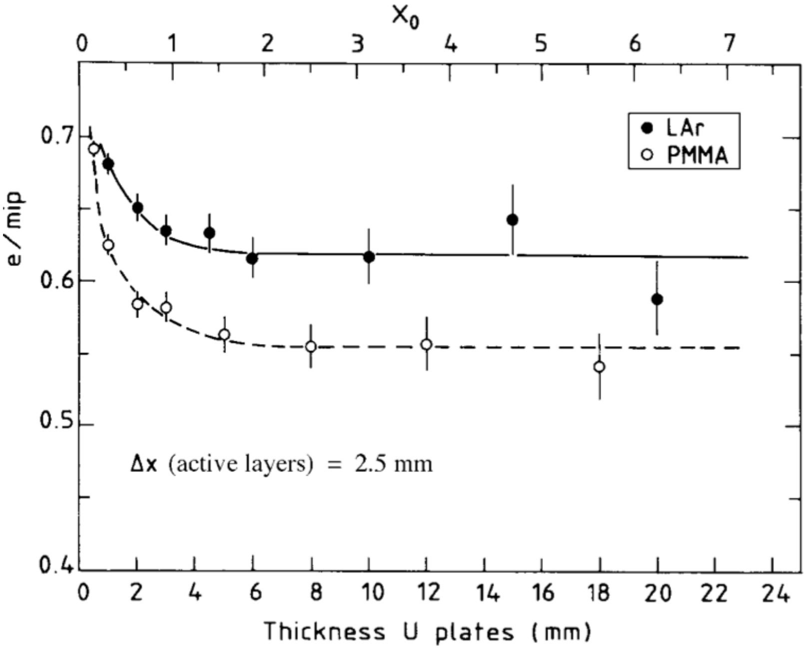

Figure 2.4.4: The e/mip ratio as a function of the thickness of the absorber layers, for uranium/PMMA and uranium/LAr calorimeters. The thickness of the active layers is 2.5 mm in all cases. Results from EGS4 Monte Carlo simulations [39].

The $^{e}/_{h}$ value may assume a wide variety of values. Some sampling calorimeters have $^{e}/_{h}$ values near 1 and are called compensating calorimeters (Section 2.4.3). Those calorimeters have a lot of advantages, one of these is the hadronic signal linearity, at least for energies > 5 GeV.

Most of the sampling calorimeters used in practice are under compensating, i.e. $^{e}/_{h} > 1$, but there are examples also of overcompensating calorimeters, i.e. $^{e}/_{h} < 1$. Three examples are shown in Figure 2.4.5. The compensation issue will be discussed later.

In Equation 2.25 the dependence of the $^{e}/_{h}$ ratio on the different calorimeter responses is shown. In the case of sampling calorimeters:

- $^{rel}/_{mip}$ is approximately 1 since relativistic charged pions resemble mips in their ionization losses;
- $^{p}/_{mip}$ decreases as the energy decreases, since low-energy protons are inefficiently sampled. As in the case of soft electrons, this contribution may increase if the thickness of the absorber layers is reduced, or if the thickness of the active layers is increased.
- $^{n}/_{mip}$ depends strongly on the A value of the absorber material. The main process through which the evaporation neutrons lose energy is the elastic scattering: the smaller is A, the larger is the kinetic energy transferred to the absorber nuclei. Neutrons may be sampled in an efficient way only if they transfer their

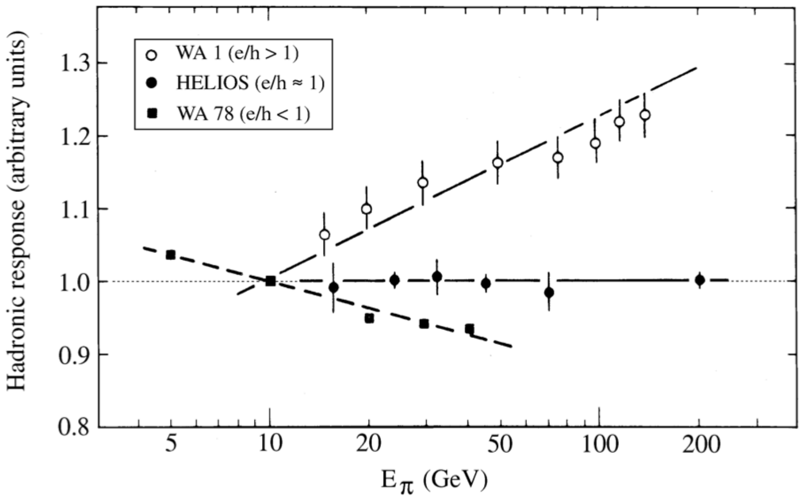

Figure 2.4.5: The response to pions as a function of energy for three calorimeters with different e/h values: the WA1 calorimeter (e/h > 1, [9]), the HELIOS calorimeter (e/h ≈ 1, [27]) and the WA78 calorimeter (e/h < 1, [11, 12]). All data are normalized to the results for 10 GeV.

kinetic energy to the nuclei. Adding hydrogen to a calorimeter structure, neutrons are quickly thermalized and lose most of their energy in the collisions. As a result, n/mip depends on the fraction of hydrogen contained in the calorimeter and has a wide range of values. Typically it is much larger than 1 in calorimeters which exploit neutron signals, even in the presence of saturation effects.

As just mentioned, saturation effects in the active medium may affect largely the hadronic response. This effects are due to signals produced by densely ionizing particles, as the spallation protons, and are often present in active media such as plastic scintillators and liquid argon.

Since the hadronic showers are broad and nuclear gammas contribute after 1 μs to the signals, the hadronic response depends on position and time. All particles which characterize the hadronic showers have a typical three-dimensional energy deposition profile. Neutrons propagate isotropically and they constitute the lateral and longitudinal tails of the shower. An example of the longitudinal distributions of various nuclides is shown in Figure 2.4.6. The em component represents instead the shower core.

This spatial dependence has to be taken into account when calibration constants are used in order to estimate the amount of energy deposited in the calorimeter. Indeed, if the calorimeter response to neutrons is very different from that to particles used to set the energy scale, the energy deposited by them may be mismeasured considerably. The same thing occurs when the energy contained in the em core is estimated. Since the calibration constants are chosen in order

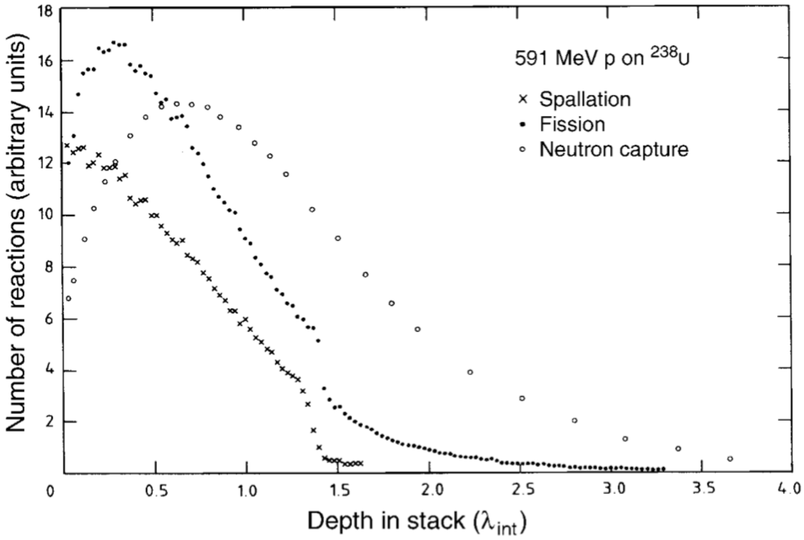

Figure 2.4.6: Longitudinal distributions of various radioactive nuclides produced in the absorption of 591 MeV protons in 238U. From [37]

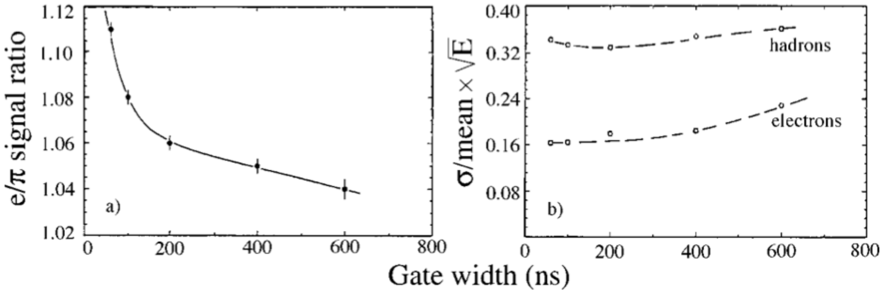

Figure 2.4.7: The ratio of the average ZEUS calorimeter signals from 5 GE/c electrons and pions (a) and the energy resolutions for detecting these particles (b), as a function of the charge integration time [31].

to reproduce the correct hadron energy for the entire shower, the energy represented by the calorimeter signals from the area near to the shower axis may be wrongly determined.

In particle physics experiments, the energy of the primary particle or of the jet is estimated by collecting signals from the central area of the calorimeter. Therefore the signals produced by neutron capture in the lateral tails are frequently cut. Moreover, since the signal integration is typically done over 100 ns, signals generated by nuclear γs, which are emitted after neutron capture, are cut away because they cover time intervals of about 1 μs. These signals usually cannot be considered, as can be inferred by Figure 2.4.7. In this figure the results relative to the ZEUS experiment are reported.

As the gate width for the signal integration is increased, a larger amount of noise is also recorded, in such a way that hadron energy resolution gets worse. Besides, also the em energy resolution deteriorates, as it is visible in figure Figure 2.4.7.b.

2.4.3 *Compensation*

The need for compensation comes from the different calorimeter responses to the em and the non-em component of an hadronic showers. The energy shared between these two parts of an hadronic shower varies from event to event, and it is energy dependent. The energy resolution is thus deteriorated by such effects, as will be discussed in the next section.

Only sampling calorimeters may be compensating and some methods for achieving compensation are discussed below. They are based on the enhancement of the response to the non-em showers.

For a long time it was believed that the use of uranium absorber could be the key ingredient for compensation, by exploiting the nuclear fission. However its use is neither essential nor sufficient. A more powerful way to increase the non-em response is by use active materials containing hydrogen, as it is clearly shown in Figure 2.4.8.

The neutrons produced during hadronic cascade undergo elastic scattering with nuclei and transfer a fraction of their kinetic energy to them:

$$f_{elastic} = \frac{2A}{(A+1)^2} \tag{2.31}$$

where A is the atomic number of the target nucleus. If a neutron scatters with an hydrogen nucleus, it gives half of its kinetic energy to the proton, which densely ionizes the medium and contributes to the calorimeter signal.

The relative contribution of neutrons to hadronic response can be tuned to the value needed for achieving compensation. This has been demonstrated experimentally for plastic-scintillator structures with Pb or ^{238}U as absorber material.

All compensating calorimeters rely on the contribution of neutrons to the hadronic signals. Indeed, by properly amplifying the neutron signals, one compensate for the invisible energy losses. This is due to the fact that the kinetic energy of the evaporation neutrons is related to the nuclear binding energy loss, as is shown in Figure 2.4.9.

In order to achieve compensation, a crucial role is also played by the sampling fraction, as shows in Figure 2.4.10. The $^{n}/_{mip}$ ratio could reach very high values, specially if the sampling fraction is very small. A compensating calorimeter must thus have a precisely tuned sampling fraction, for amplify the neutron signals by the proper factor.

To summarize, a compensating calorimeter has to be a sampling device and the active material has to contain hydrogen and to be sensitive to the signals produced by recoil protons.

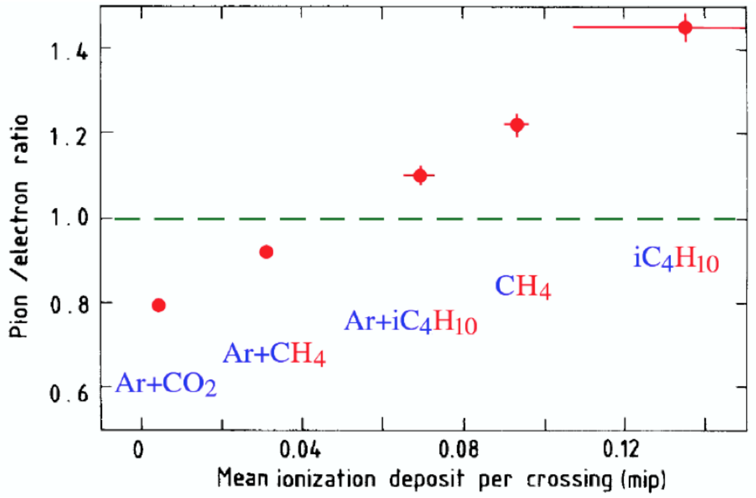

Figure 2.4.8: The π/e signal ratio as a function of the hydrogen content of the gas mixture [33].

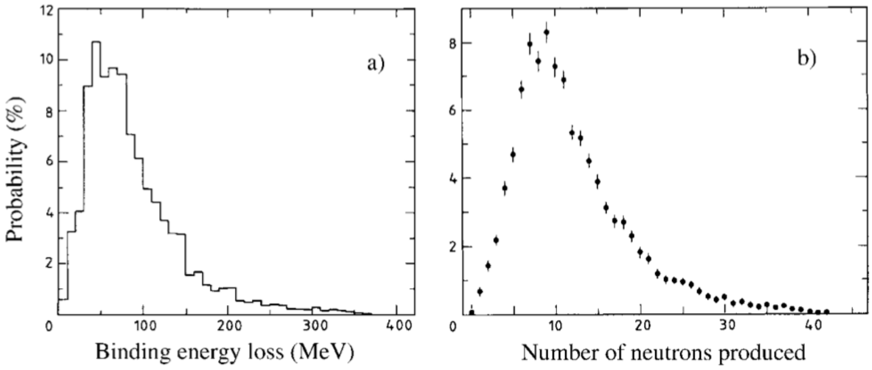

Figure 2.4.9: The nuclear binding energy lost in spallation reactions induced by 1 GeV protons on ^{238}U nuclei (a), and the number of neutrons produced in such reactions (b). From [39].

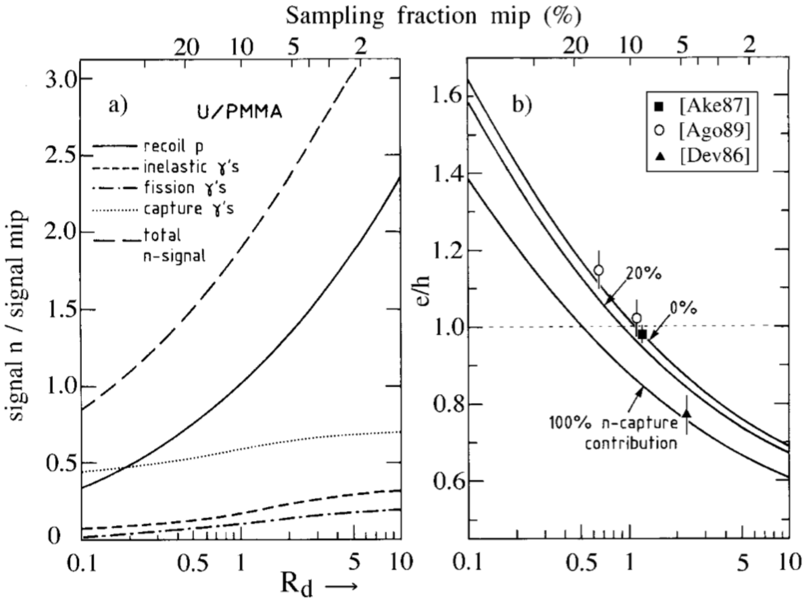

Figure 2.4.10: The n/mip response ratio, split up into its components, for ^{238}U/PMMA calorimeters, as a function of R_d, the ratio of the thicknesses of the passive and active calorimeter layers (a). The e/h ratio as a function of R_d, assuming that 0%, 20% or 100% of the γs released in thermal neutron capture contribute to the calorimeter signals (b). The top axis of both graphs indicates the sampling fraction for mips. From [40].

In intrinsically non-compensating devices, an alternative approach, called *off-line compensation*, can be applied. As the term suggests, the compensation is done off-line and through the determination of the two components event by event. It can be carried out exploiting the different spatial development of the em and non-em showers, or measuring the em fraction f_{em} event by event. The latter method can be achieved by comparing, for example, the scintillation and the Cherenkov light produced in scintillator-based calorimeters. Only relativistic particles radiate Cherenkov light: in an hadronic showers, the em component consists of relativistic particles (electrons and positrons) down to few hundred keV, while in the non-em component the energy is mostly deposited by non relativistic particles, i.e. spallation protons and neutrons. Therefore, only the em component of the hadronic showers radiates Cherenkov light, and comparing the Cherenkov signal with the scintillation one, which is generated by all the showering particles, the f_{em} can be estimated.

Calorimeters based on the detection of the Cherenkov light are extremely non-compensating devices and may be used only for the reasons just mentioned. They are fast devices since the emission of Cherenkov light is an instantaneous process (the time constant is typically equal to 5-10 ns). This feature allows to separate two events very closely spaced in time. Besides, only the em core of hadronic showers is detected. Therefore, the volume necessary to contain hadronic showers is smaller, both longitudinally and laterally. Hadron showers look thus very narrow and this is important since the shower overlap when particle densities are very high may be reduced. Because of these properties, calorimeters which exploit the Cherenkov light may be used in future experiments.

2.5 FLUCTUATIONS

Calorimeters are instruments aimed to the energy measurement of particles in high-energy physics. Therefore the most important characteristic of a calorimeter is its energy resolution. Energy resolution determines the precision with which the energy of a particle can be measured and is estimated experimentally through the calibration of the calorimeter. A variety of fluctuations affect the energy resolution and they will be discussed below.

Since calorimeters are based on physical processes that are statistical in nature, signal quantum fluctuations affect the precision of calorimeters, as well as other effects, such as shower leakage, sampling fluctuations, etc.

Fluctuations, aside from those caused by shower leakage and instrumental effects, follow Poisson statistics. Therefore they contribute to the energy resolution with a term:

$$\frac{\sigma_E}{E} = a\frac{1}{\sqrt{E}} \tag{2.32}$$

where energy is expressed in GeV.

Usually several sources of fluctuations contribute to the energy resolution of a calorimeter but often one source dominates the others, as sampling fluctuations in sampling calorimeters for example. Typically, they have different energy dependence and are uncorrelated. Therefore these fluctuations have to be added in quadrature:

$$\sigma_E = \sqrt{(\sigma_1)^2 + (\sigma_2)^2 + (\sigma_3)^2} \tag{2.33}$$

where $\sigma_1, \sigma_2, \sigma_3$ are the standard deviations of the fluctuations caused by source 1, 2, 3 respectively. If some sources of fluctuations are correlated, they have to be combined accordingly.

2.5.1 *Signal quantum fluctuations*

The precision of calorimetric measurements is determined and limited by fluctuations. Since the statistical nature of processes on which calorimeters are based, signal quantum fluctuations may affect the energy resolution.

Among the calorimeters which are dominated by signal quantum fluctuations, there are the quartz fiber calorimeters. In these devices,

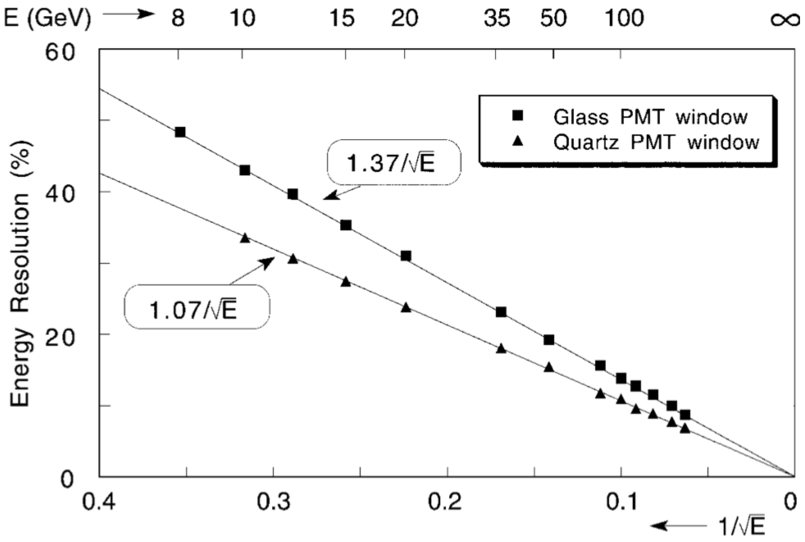

Figure 2.5.1: The energy resolution for electron detection with the QFCAL prototype detector, as a function of energy. Results are given for measurements in which photomultiplier tubes with a glass window were used and for measurements in which the same type of PMTs were equipped with a quartz window [13].

given the very small light yield, such as 1 photoelectron per GeV, large signal quantum fluctuations deteriorate the energy resolution and make negligible other sources of fluctuations. The cause for this large fluctuations is the following: only a small fraction of the scintillation light and the Cherenkov light generated in the quartz fibers is trapped and transported to the PMT. Besides, using PMTs with glass window, the probability that a Cherenkov photon reaches the photocathode is limited. The quantum efficiency can be improved if PMTs are equipped with quartz windows, as shown in Figure 2.5.1.

2.5.2 *Sampling fluctuations*

These fluctuations are determined both by the sampling fraction, i.e. the energy deposited by minimum ionizing particles in the active calorimeter layers, measured relative to the total energy deposited by such particles in the calorimeter, and the sampling frequency, i.e. the thickness of the layers for a given sampling fraction.

The nature of these fluctuations is statistical too, since they arise from fluctuations in the number of shower particles which contribute to the signal.

In electromagnetic calorimeters with non-gaseous media, the expression below well describes these fluctuations:

$$\frac{\sigma}{E} = 2.7\%\sqrt{d/f_{samp}} \cdot E^{-1/2} \tag{2.34}$$

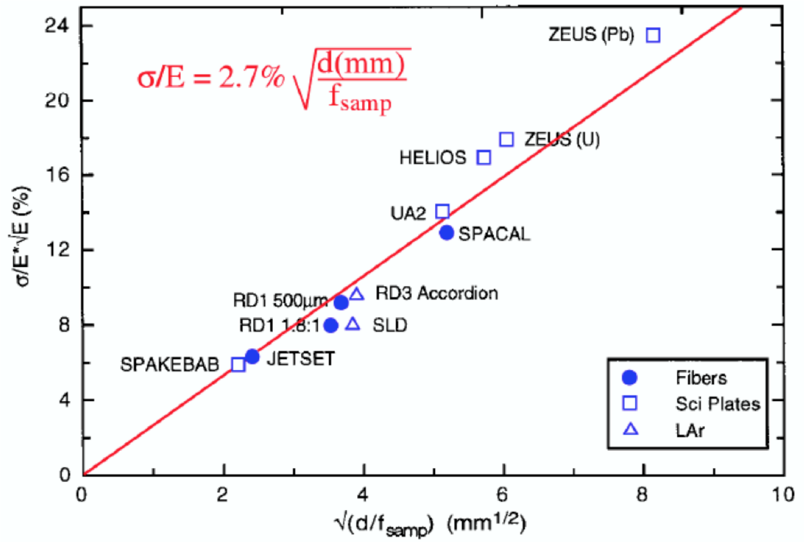

Figure 2.5.2: The electromagnetic energy resolution as a function of the parameter $(d/f_{samp})^{-1/2}$. See text for details. [38]

where d is the thickness of the active sampling layer (e.g. the diameter of a fiber or the thickness of a scintillator plate or a liquid-argon gap, in mm) and f_{samp} is the sampling fraction for mips (see Figure 2.5.2).

The thickness of the absorber material determines the number of Compton electrons and photoelectrons contributing to the signals. The smaller is its thickness, the larger are the soft electrons sampled. The thickness of the active material determines instead the size of fluctuations in the contributions from individual shower particles. Indeed, in detectors with very large sampling fraction, electrons may also be generated in the active layers.

Increasing both these quantities, particles are sampled more efficiently and energy resolution improves.

Figure 2.5.3.a shows examples of energy resolution as a function of f_{samp}, in several plastic-scintillator calorimeters. Figure 2.5.3.b shows results relative to scintillating-fiber calorimeters: as the diameter of the fibers decreases, the energy resolution improves since the sampling frequency increases.

The energy resolution of fiber calorimeters is better that the one for scintillator-plates calorimeters, for a given sampling fraction. Indeed, in the former there is a larger number of active layers in a given volume and so the amount of boundary surfaces between active and passive layers is greater. As a consequence, a large number of soft electrons may contribute to the calorimeter signals.

Until now only soft electrons produced through Compton scattering and photoelectric effect have been discussed. Regarding the em showers, there also the fast e^+e^- pairs created in the conversion of high-energy γs. These particles may contribute to the signal in several consecutive active layers. However, in dense active materials, the range

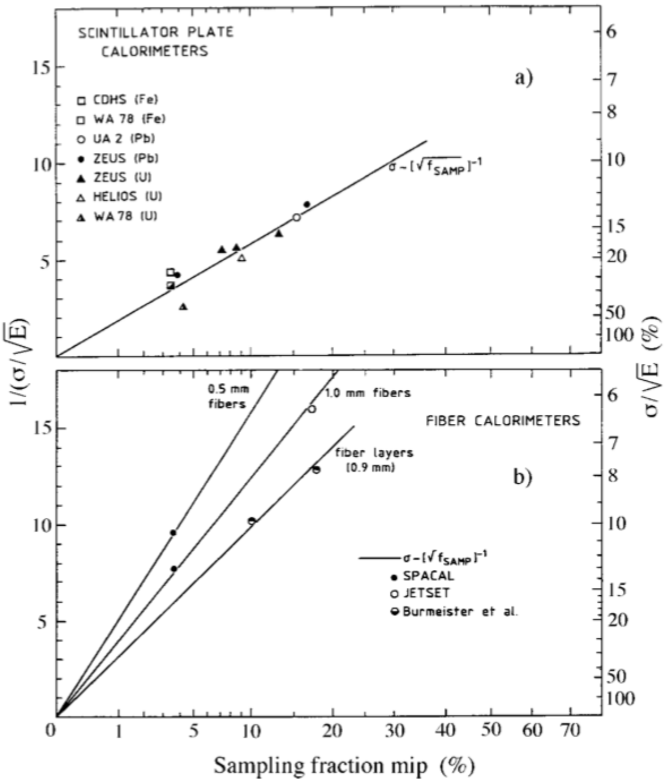

Figure 2.5.3: The em energy resolution as a function of the sampling fraction for various representative plastic scintillator plate calorimeters (a) and for scintillating-fiber calorimeters (b). From [38] .

of these particles is very small and typically there is no correlation between signals in neighbouring active layers, as had been thought at the beginning [36].

2.5.3 *Shower Leakage*

Calorimeters have become fundamental devices in particle physics experiments and at colliding-beam machines have to be designed as 4π detectors.

As a consequence, it is very important to know the degree of the shower containment with the most accurate precision. First, in order to limit shower leakage fluctuations, and second, in order to avoid the escape of particles, which may disturb the performance of the detectors located downstream the calorimeter, such as the muon counters. Shower leakage depends on the energy and on the type of showering particles. Electrons of a given energy are better contained than protons of the same energy, and the latter are better contained than pions, on average.

The fluctuations in the shower leakage do not have statistical nature and can be classified in:

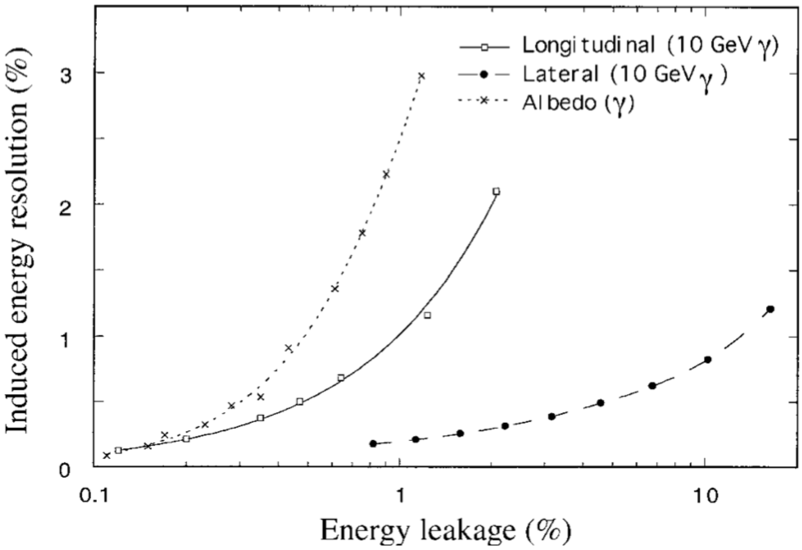

Figure 2.5.4: A comparison of the effects caused by different types of shower leakage. Shown are the induced energy resolutions resulting from albedo, longitudinal and lateral leakage as a function of the average energy fraction carried by particles escaping from the detector. The longitudinal and lateral leakage data concern 10 GeV γs, the albedo data are for γ-induced showers of different energies. Results from EGS4 Monte Carlo calculations [41].

- longitudinal leakage. Shower particles escape the detector coming out from the rear end of the calorimeter.
- lateral leakage. Shower particles escape through the lateral sides of the calorimeter. Since the energy of a particle is determined integrating the signal over a volume surrounding the shower axis, lateral losses are typically larger than the longitudinal ones. So the effects of lateral leakage usually dominate the performance of a calorimeter.
- albedo. Particles are backscattered from the front face of the calorimeter. This effect is the only one which is by definition unavoidable but is also the smaller one, except at low energies.

A comparison of these three effects is shown in Figure 2.5.4, from which is also clear that longitudinal leakage fluctuations most affect the energy resolution. The reason for that resides in the different number of shower particles responsible for the leakage. Longitudinal fluctuations are driven by fluctuations in the starting point of the shower, i.e. by the behavior of a single particle. Lateral fluctuations are essentially due to a large number of particles, and therefore these fluctuations are smaller (see Figure 2.5.5).

Shower leakage through the front face of the calorimeter are relevant only at low-energies. Indeed, the backscattered particles have to be very soft in order to subtend such large angles. Albedo may cause more

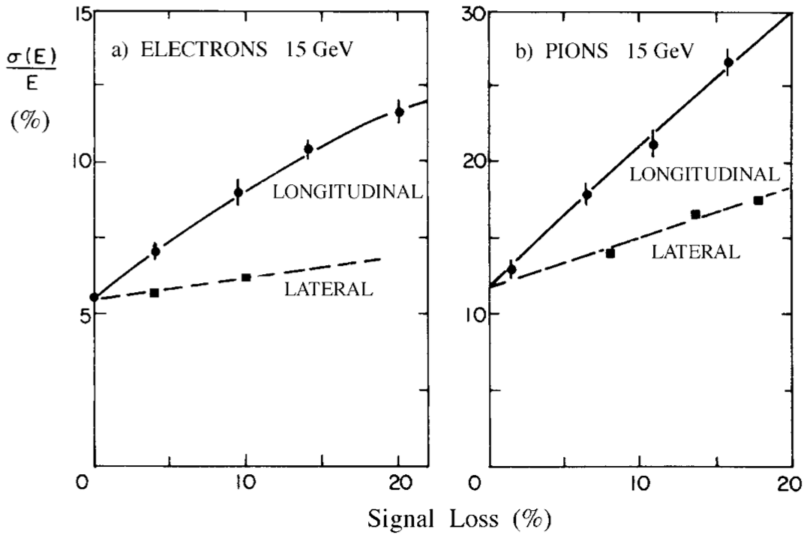

Figure 2.5.5: The effects of longitudinal and lateral shower leakage on the energy resolution, as measured for 15 GeV electrons (a) and pions (b) by the CHARM Collaboration in a low-Z calorimeter [5, 2].

serious problems in the upstream detectors, since albedo particles may produce signals and damage the tracking detectors.

2.5.4 *Instrumental Effects*

The calorimeter performance is also affected by instrumental effects such as the electronic noise, the light attenuation, channeling effects and the structural differences in sampling fraction.

The electronic noise contributes to the signals. Its contribution to the energy resolution scales with E^{-1} and is completely uncorrelated to the other sources of fluctuations. For example, in scintillator-based calorimeters, a source of noise is given by the electronic modules (e.g. Analog to Digital Converter (ADC)) which digitize and analyze the PMT signals. The electronic module, in absence of the PMT signal, accumulates a certain amount of charge which results in a "pedestal". Obviously these pedestals have to be subtracted from the raw signals in order to get the real calorimeter signals. Pedestals fluctuate as well, and their fluctuations may be reduced by increasing the PMT gain: in this way signal amplitudes increase and may be best resolve with respect to the electronic noise.

Light detectors are also affected by light attenuation, which induces a position dependence in the calorimeter response. One simple method to limit the effects of light attenuation and to correct the residual effects is to use a two-sided readout. Many experiments such as ZEUS, HELIOS and KLOE exploit this technique in their calorimeters.

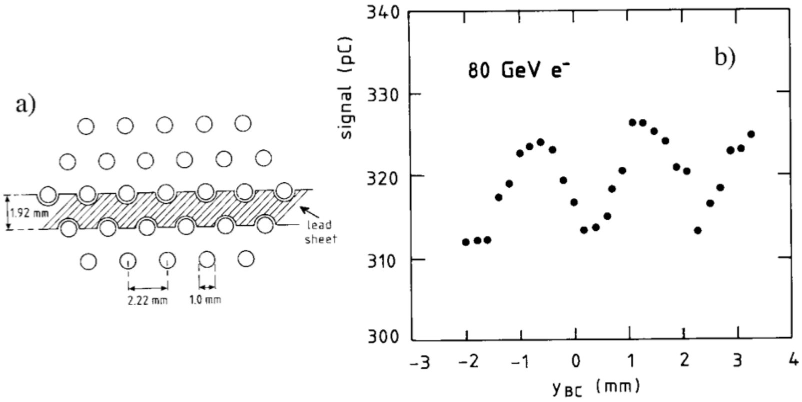

Figure 2.5.6: Lateral cross section of SPACAL (a). The SPACAL signal as a function of the y-coordinate of the impact point (b). Data for 80 GeV electrons. From [7].

Fiber-calorimeters are moreover affected by channeling effects, i.e. particles which enter the calorimeter exactly at the position of a fiber generate anomalous signals. This effect can be avoided if fibers are oriented at angles different from 0° with respect to the direction of the incident particles. Another consequence of this phenomena is the position dependence of the signal, as it is visible in Figure 2.5.6. Indeed, depending on the impact point of the particle, the part of the shower sampled may be very large (impact point in the fiber plane) or very small (impact point between two fiber planes). As before, this effect disappears when the detector is slightly tilted. Besides, using fibers with a small radius, this effect is considerably smaller.

Many other instrumental effects exist and may affect the energy resolution of the calorimeters but their discussion is beyond the aim of my thesis.

In practice the resolution of a given calorimeter is affected by different types of fluctuations, each with its own characteristic energy dependence. In Figure 2.5.7 the em energy resolution for the various contributions is shown. For energies below 10 GeV, electronic noise is the dominant contribution, between 10 and 100 GeV stochastic fluctuation dominates, while for energies greater than 100 GeV energy-independent source of fluctuations dominate (such as the impact-point dependent response).

2.5.5 *Fluctuations in hadronic showers*

The same source of fluctuations also characterized the hadronic energy resolution.

Sampling fluctuations are larger for hadronic showers because the number of different particles which contributes to the generation of the signal is smaller. Indeed the spallation protons, which are the

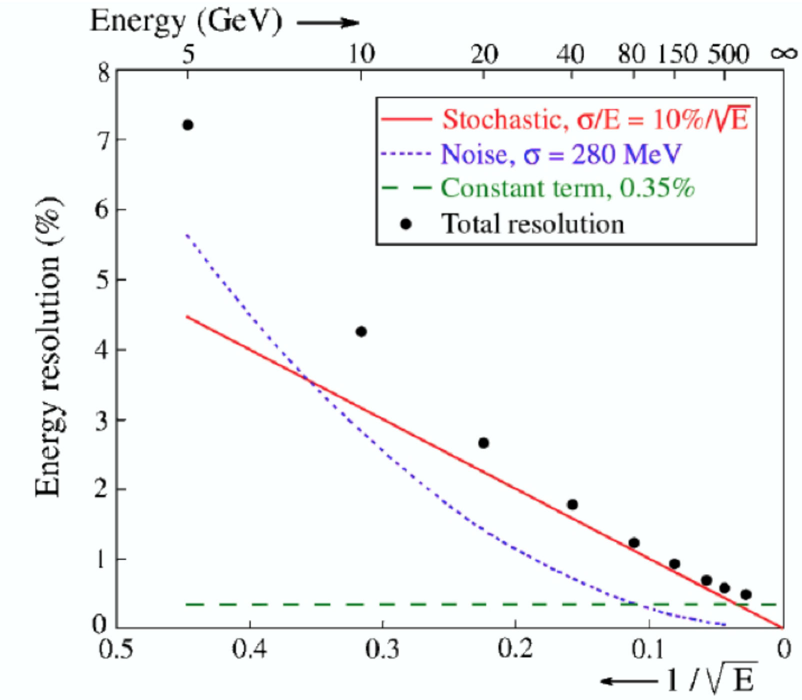

Figure 2.5.7: The em energy resolution and the several contribution to it, for the ATLAS EM calorimeter [33].

leading hadronic particles in the energy deposition processes, may traverse several active layers.

However, one of the dominant source of fluctuations is the *invisible energy*, which tends to dominate the performance of an hadronic calorimeter. The fraction of the invisible energy fluctuates strongly event by event but it can be eliminated, or at least reduced, if the active and the passive materials are chosen properly, as discussed in Section 2.4.3.

Another source of fluctuations is the em shower fraction f_{em}. In pion showers there is an asymmetry between the probability of a large fraction of energy carried in the em shower component and the probability of a similar fraction carried by the hadronic component. Indeed π^0s production may occur in the first generation as well as in the next ones, and the conversion of them in electromagnetic showers is irreversible. This asymmetry is clearly visible in Figure 2.5.8.

In the case of proton showers, fluctuations in the f_{em} are smaller. The conservation of the baryon number limits the production of leading π^0s and thus the em component of the shower is smaller, in comparison with pion showers. The energy resolution is thus better for proton showers, as Figure 2.5.8 shows. The signal distributions represented in this figure have been recorded by the CMS Quartz-Fiber calorimeter. The rms width is about 20% smaller in the proton distribution.

In non-compensating calorimeters, the non-Poissonian fluctuations of the f_{em} usually dominate the hadronic performance. Their contri-

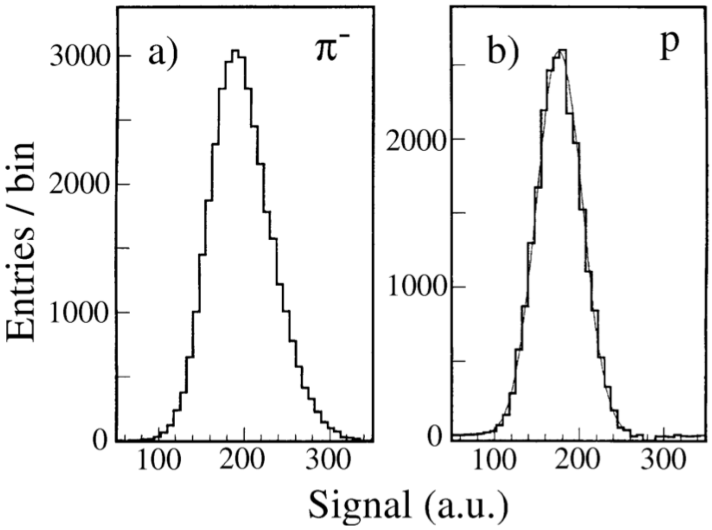

Figure 2.5.8: Signal distributions for 300 GeV pions (a) and protons (b) detected with a quartz-fiber calorimeter. The curve represents the result of a Gaussian fit to the proton distribution [14].

butions depend on energy and fluctuate event by event. Due to their dependence on the energy, the f_{em} fluctuations do not contribute with a constant term, but with an energy dependent term, which has to be added in quadrature with the other contributing terms as below:

$$\frac{\sigma_E}{E} = \frac{a}{\sqrt{E}} \oplus cE^{-0.28} \tag{2.35}$$

The first term in the second member is the stochastic term. The parameter c is determined by the e/h value ($0<c<1$).

2.5.6 *The shape of the response function*

Not all types of fluctuations give rise to response variations that are symmetric around the average value.

For example, the fluctuations in the f_{em} may be asymmetric, as described before for pion showers.

In the case of shower leakage, low-energy tails in the signal distributions occur. These tails are due to escaping particles, which lose only a little fraction of the energy in the calorimeter. In scintillating calorimeters read out at the rear end by silicon diodes, or PMTs, the longitudinal leakage can provoke large signals, and in this case high-energy tails in the signal distribution occur.

Signal quanta fluctuations are instead characterized by Gaussian response function if the number of quanta released by the showering particles is high, as follows from the central limit theorem. In the case of a very small number of signal quanta, for example when the light yield is very low, the response function is a Poisson distribution. This effect has been observed in quartz-fiber calorimeters.

2.5.7 *Choosing the calorimeter system*

In the previous sections many different types of calorimeters have been described. The choice of the technology and of the detector parameters depends on many factors, such as the physics that one wants to study, the radiation levels, the costs and others.

If one wants a calorimeter with a high performance in detecting em showers, an inevitable consequence will be the poor performance for hadron detection. Indeed, as mentioned before, high electromagnetic energy resolution means high e/h value, and so poor hadronic energy resolution. Several projects aim to find a reasonable compromise in order to have a calorimeter with good performance for both em and hadron detection, and one of them will be discussed in detail in the next chapter.

The calorimeter system is often chosen after that prototypes have been tested in particle beams. Obviously, the results obtained at test-beams have to be interpreted with caution. Indeed the signal integration can be done over the entire volume and/or over a long time, while in real experiments this is not possible.

In a real experiment the presence of inert materials, such as cables, support structures and electronics, between the interaction vertex and the calorimeter will affect particles and will certainly deteriorates the energy resolution of the device. Moreover one has only the calorimeter signal while at test-beams the nature and the energy of the particle entering the calorimeter is well known. In many calorimeters, the total signal depends strongly on the type of particle, i.e. electrons and pions of the same energy cause quite different signals. Therefore, when a collection of different particles enter the calorimeters, all the weighting schemes devised for the detection of individual particles of known type and energy, become useless.

Also the choice of the readout and the segmentation of the system is crucial and one has to consider the experimental conditions in order to decide the optimal solution.

Finally, if one wants to improve the calorimeter's energy resolution, one has to work on the fluctuations that dominate. For example, the light yield of quartz-fiber detectors is typically very small and the signal quantum fluctuations are the major contribution to the energy resolution. Increasing the sampling frequency, in order to reduce the sampling fluctuations, do not improve the precision of the device. The only possibility is to increase the light yield, choosing for example PMTs with the high quantum efficiency in the UV range.

3

THE DUAL-READOUT METHOD

In modern experiments the measurement of jets is one of the most important challenges. At high energies jets are characterized by a rather collimated bunch of particles: hadrons, photons (mainly from π^0s decay) and also leptons (from fragmenting b or c quarks). A calorimeter system must thus have signal speed and good energy resolution.

High-resolution hadron calorimetry is very relevant for a future high-energy linear e^+e^-collider in order to distinguish, for example, the $W^\pm$ and Z^0 bosons decay in jets. At such linear collider this task will be more difficult than it was at LEP since there will be no kinematic constrains. Indeed electron and positron beam will emit bremsstrahlung radiation when they pass by each other, i.e. "beamsstrahlung", and thus the center-of-momentum energy cannot be known. On the other hand the uncertainties due to jet algorithm and the contributions of underlying events to the signals will be very small, because of its clean leptonic environment.

As results from Monte Carlo simulations, a jets energy resolution of about $30\%/\sqrt{E}$ is required for distinguishing $W^\pm$ and Z^0 bosons decays in jets, and this resolution can be reached with compensating calorimeters, as the SPACAL [7] and ZEUS [30] calorimeters.

However, compensating calorimeters had some drawbacks. Indeed, compensation requires large integration volume and time since it relies on neutron detection, and this is often not possible in a real experiment. For example, SPACAL reached an hadronic resolution of $\sigma/E \sim 30\%/\sqrt{E}$ with 13 tons and 80 ns. Moreover, compensating calorimeters have a modest electromagnetic energy resolution because of the small sampling fraction, necessary in order to achieve compensation.

As discussed in chapter 2, high-resolution electromagnetic and high-resolution hadronic calorimetry are mutually exclusive: good jet resolution involves poor em resolution and vice versa. Besides, it is not possible yet to achieve in hadron calorimetry the same level of precision of em calorimeters because of hadron-specific fluctuations, i.e. em shower fraction and invisible energy fluctuations. Indeed the theoretical achievable limit for hadronic calorimeters is $\sigma/E \sim 15\%/\sqrt{E}$, in lead absorber (the limit value depends on the not perfect correlation between the number of neutrons produced and the invisible energy).

Until now, there are two major R&D (*Research & Development*) projects which aim to improve the hadronic energy resolution, the *Particle Flow Algorithm* (PFA) and the *Dual-REAdout Method* (DREAM).

The *Particle Flow Algorithm* is based on the combined use of a precision tracker and a calorimeter with high granularity. The idea is that the charged jet fragments are measured with the tracker, while neutral particles are measured with the calorimeter. Such methods have been used in the reconstruction of di–jets from Z^0 decay within the TESLA detector at DESY, resulting in a final mass resolution of better than 3 GeV [34]. The imaging detector capability, along with the use of the particle flow algorithm, allows the reconstruction of almost all individual particles in an event. Nevertheless the calorimeter measures also the charged particles and so a double counting problem arises. To solve this problem, it is necessary to de-convolute contributions to the calorimeter signal from showering charged particles. The deconvolution is based on a Monte Carlo simulation, which is far from perfect.

A finer granularity does not solve the shower overlap problem and the only way to prove the merits of this method is by means of prototypes studied at testbeams. The CALICE Collaboration [3] has built several detectors which exploit different technology, in order to test this method.

The other approach, called the *Dual-readout Method*, exploits the simultaneous readout of two type of light, the scintillation and the Cherenkov radiation. The Cherenkov light in hadronic showers is produced almost only by the em shower component. Indeed, the non-em component of an hadronic shower is mostly constituted by spallation protons and neutrons, which are not relativistic and thus do not produce Cherenkov light. Therefore, by comparing the amount of Cherenkov and scintillation light produced by an hadronic shower in this type of calorimeter, one can determine the em shower fraction and the neutron fraction event by event, as will be discussed in the next sections. Fluctuations in the f_{em} and in the neutron fraction bring to hadronic non-linearity, non-Gaussian response function and poor energy resolution. The dual-readout technique allows to measure the f_{em} and the neutron fraction event by event, eliminating thus the relative fluctuations.

The DREAM Collaboration had studied first, by testing a fiber calorimeter, how to eliminate the main contributions to hadronic energy fluctuations, i.e. the em shower fraction f_{em} and the invisible energy fluctuations. After the excellent results obtained with this detector, which had established the validity of the concept of the dual-readout technique, other effects such as the sampling fluctuations and the signal quantum statistics started to be studied. In this context, a wide study of crystal calorimeters was carried out, in order to develop an high-performance em calorimeter using the same readout scheme. Besides, the DREAM Collaboration had studied the performance of an hybrid calorimeter, constituted by the fiber calorimeter and by the crystal em section, by applying the dual-readout technique to both detectors. Without using the dual-readout method, the e/h mismatch would spoil the hadronic resolution because the e/h of a crystal calorimeter is typically ~ 2. The application of the dual-readout principles in such a calorimeter may work only if one can detect simultaneously scintillation and Cherenkov signals also in the em section. With this hybrid calorimeter an excellent hadronic and electromagnetic energy resolution may thus be reached. This issue will be discussed in depth later.

In the next section I will discuss the fiber detector which exploits this technique.

3.1 THE DREAM DETECTOR

The first detector which demonstrated the feasibility of the dual-readout technique was a 10 λ_{int} calorimeter based on a copper absorber structure and equipped with plastic-scintillator and Cherenkov fibers, which generate the scintillation and the Cherenkov light separately. The choice of a fiber calorimeter was done for the possibility to measure the relative contribution of the scintillator and the Cherenkov signals independently, without any contamination.

The ratio of the quartz and scintillator signals turns out to be related to the em fraction of the shower energy, and its measurement event-by-event allows to eliminate the relative fluctuations. This device and the collaboration that operates it is known as DREAM (Dual-READout Method). Some results are described below [15].

The basic element of this detector is an extruded copper rod, 2 m long and 4x4 mm^2 in cross section. The rod is hollow and in the central hole, with a diameter of 2.5 mm, seven optical fibers are inserted. Three of them are plastic scintillating fibers, the other four are Cherenkov ones. Two different Cherenkov fibers are used: in the central region of the detector high-purity quartz fibers are exploited while in the peripheral regions acrylic plastic ones were used for cost reasons. All fibers have an outer diameter of 0.8 mm and a length of 2.5 m. The fiber pattern is the same for all rods, and it is shown in Figure 3.1.1. The DREAM detector consists of 5580 rods, 5130 of these equipped with fibers, the others are used as fillers on the periphery of the detectors.

Fibers are grouped to form 19 readout towers: each tower consists of 270 rods and has an hexagonal shape, as it is visible in Figure 3.1.2. At the rear end of the calorimeters, fibers in each tower are split into two bunches: one bunch of scintillating fibers and one of Cherenkov fibers, adding up to 38 bunches in total.

Each hexagonal cell is readout by 2 PMTs (10-stage, Hamamatsu R-580), one for each type of light. A yellow filter is installed between scintillating fibers and the PMTs. The yellow filter predominantly removes the blue part of the spectrum, increasing the attenuation length

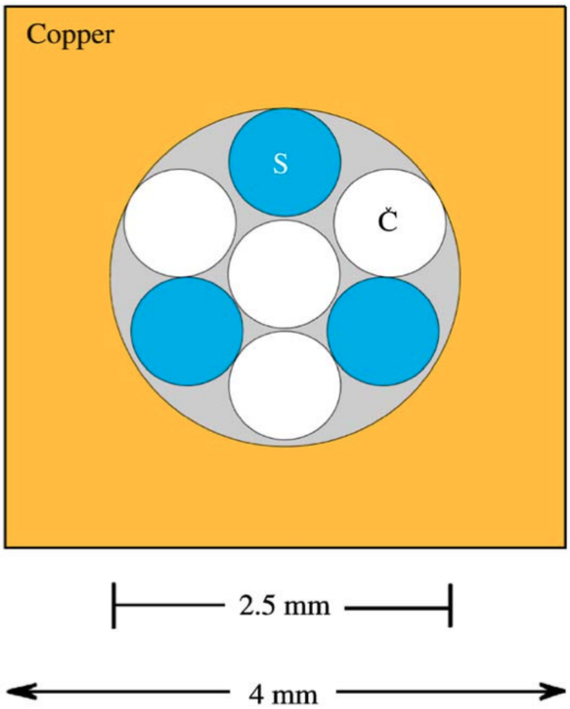

Figure 3.1.1: The basic building block of the DREAM detector. Seven optical fibers (four Cherenkov and three scintillating fibers) are inserted in the copper rod hole, as shown. See text for details. [15]

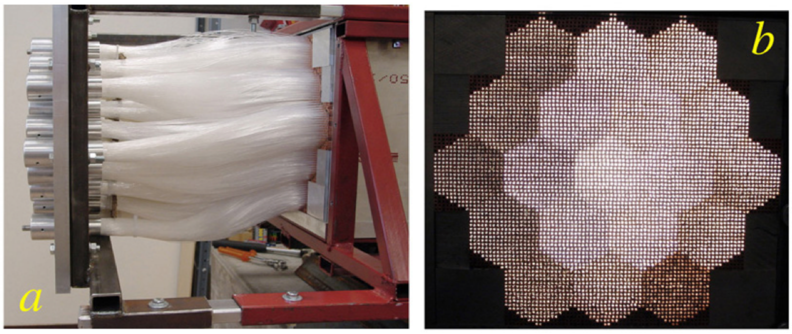

Figure 3.1.2: The DREAM detector. Shown are the fiber bunches exiting from the downstream end of the detector (a), and an image of the front face while the fibers were illuminated with a bright lamp from the rear (b). The hexagonal readout structure is clearly visible. [15]

of the scintillating fibers substantially. In the case of the Cherenkov fibers, light attenuation is very low.

The effective radiation length (X_o) of the calorimeter is 20.1 mm, the Molière radius (ρ_M) is 20.4 mm and the nuclear interaction length (λ_{int}) 200 mm.

The DREAM detector was tested at the CERN Super Proton Syncrotron (SPS) with pions and simulated "jets" (obtained with pion beam hitting a 10 cm polyethylene target upstream the detector). The calibration of the 19 towers was done with 40 GeV electrons, with the detector tilted of 2° with respect to the beam direction in order to avoid channeling effects. Indeed, as we will see, this type of calorimeter does not need to be calibrated with hadrons.

3.1.1 *Electron detection with the DREAM calorimeter*

The DREAM detector was designed for hadron calorimetry. However, it is interesting to analyze the performances in term of electromagnetic shower detection [17].

Sampling inefficiencies, light attenuation and signal non-uniformity have relevant consequences for the electromagnetic energy resolution. The effects of sampling inefficiencies, which result in sampling non-uniformity, depend on the angle between the shower axis and the fiber direction. Light attenuation in the fibers and the signal non-uniformity near the boundaries between towers and over the entire surface of the hexagonal readout tower cause also signal non-linearity. These effects may be caused by variation in fiber quality and/or in the quantum efficiency of the PMT's photocathode. The light attenuation was stronger in the scintillation fibers and so non-linearity is more prominent in the scintillation signals. These effects lead to a deviation from the $E^{-1/2}$ scaling and to the presence of a constant term, which becomes dominant at higher energies.

The electromagnetic performance of the DREAM detector is very sensitive to the angle of incidence of the particles relative to the fiber direction, due to channeling effect. The latter is considerably smaller for the Cherenkov signals.

Figure 3.1.3 shows the em energy resolution of the DREAM calorimeter for the two readout media. The angle θ and ϕ are the angles of incidence of the beam particles with respect to the fibers in the vertical plane and the horizontal plane respectively. This comparison shows that the stochastic term for the quartz readout is larger than that for the scintillation fibers.

The performance is very poor for electromagnetic detection and this is due to the poor light yield of quartz fibers (8 p.e. per GeV) and of plastic fibers (18 p.e. per GeV). On the other hand the deviation from $E^{-1/2}$ scaling is somewhat smaller for signals measured with the Cherenkov fibers, since non-uniformities are larger in the case of

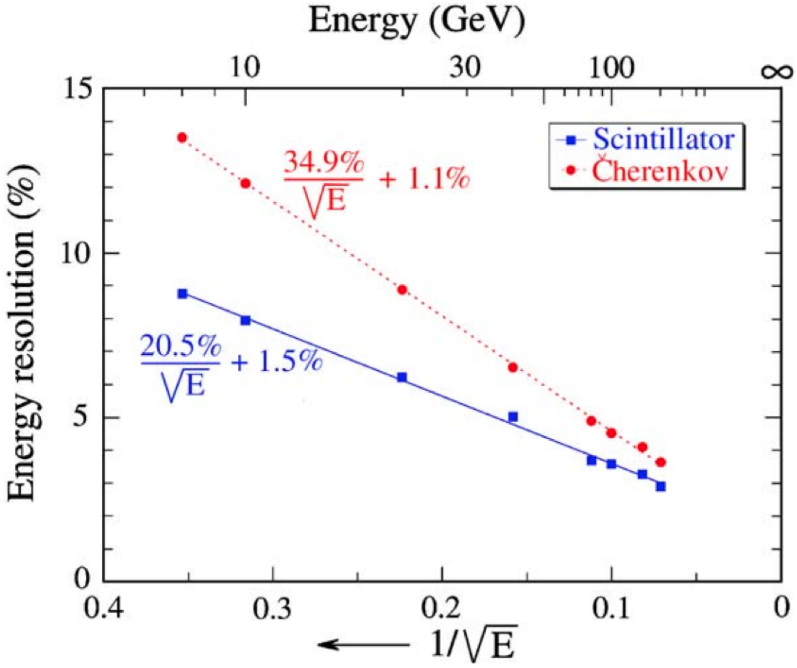

Figure 3.1.3: The em energy resolution as a function of energy, measured with the scintillating (squares) and Cherenkov fibers (circles), for electrons entering the calorimeter in the tilted position ($\phi = 3°, \theta = 2°$).

scintillation light. However they are very small and the response to electrons results reasonably uniform.

In Figure 3.1.4 the response of the DREAM calorimeter to electrons in the range 8-200 GeV, for both the scintillation and the Cherenkov signals is shown. The data are normalized to the response for 40 GeV electrons, obtained in the calibration runs. This response was $\sim 1\%$ smaller than that in the energy scans. The statistical errors are smaller than the size of the symbols. Systematic errors, dominated by gain instabilities, are at the 1–2% level.

The Cherenkov response is nearly constant while the scintillation one exhibits a large non-linearity, since it is highly affected by non-uniformities.

Indeed, the response at 8 GeV is $\sim 12\%$ smaller than that at 200 GeV.

In order to limit the contribution of the signal quantum fluctuations to the energy resolution as much as possible, the light yield of both types of fibers has to be as large as possible. It was estimated that the light yield has to be larger than 40 p.e. per GeV deposited energy in order to limit the effects of signal quantum fluctuations on the energy resolution to $15\%/\sqrt{E}$ [4]. This requirement is especially important for Cherenkov signals, since the Cherenkov light is emitted only by the em component of the shower. So the Cherenkov light yield should be about 80 p.e. per GeV. In order to increase the light yield of the Cherenkov and scintillation fibers, a number of parameters can be

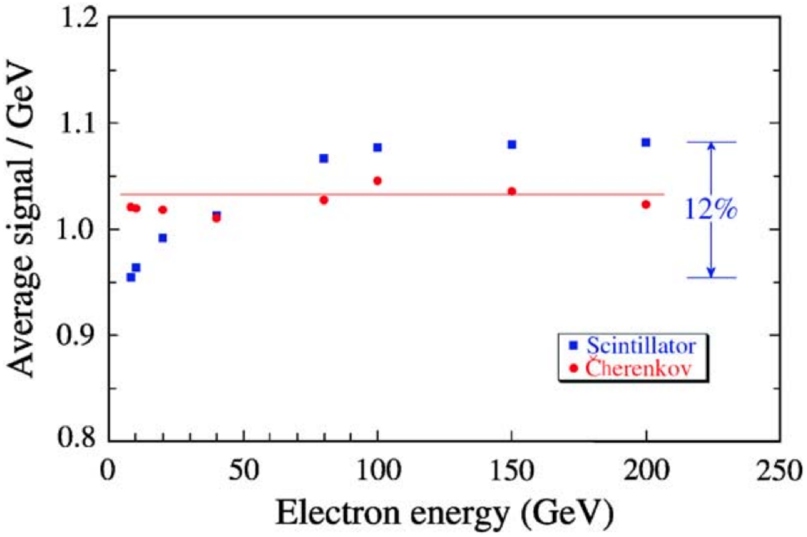

Figure 3.1.4: The response for electrons entering the DREAM calorimeter oriented in the tilted position ($\phi = 3°$, $\theta = 2°$) as a function of energy. Results for the scintillating fibers (squares) and the Cherenkov fibers (circles) are shown separately [17]

changed, such as the numerical aperture of fibers, the Cherenkov light yield, the quantum efficiency, etc.

3.1.2 *Hadronic and jet detection with the DREAM calorimeter*

The DREAM detector was tested with pions and simulated jets with energies ranging from 20 to 300 GeV [16].

The signal distributions for 100 GeV pions is shown in Figure 3.1.5, for both scintillation and Cherenkov light. The distributions are both asymmetric and broad, reflecting the characteristics of the f_{em} fluctuations in a non-compensating calorimeter. Another consequence of the under compensating nature of this calorimeter, i.e. $e/h = 1.3$ for copper/scintillator and $e/h = 4.7$ for copper/Cherenkov fibers, is that the mean values of pion signals are considerably smaller than those for electrons of the same energy, which are used to set the scale.

The energy resolution for single-pion shower is shown in Figure 3.1.6. It is well described by a linear sum of a $E^{-1/2}$ scaling term and a constant term.

The calorimeter is also non-linear for both pion and jet detection as shown in Figure 3.1.7: the scintillation response increases by $\sim 20\%$ over the energy scan performed.

In Figure 3.1.8 a scatter plot of the Cherenkov signals versus the scintillation ones for 100 GeV negative pions is shown. Each dot represents an event. The Q/S ratio is represented by a straight line in this plot. The fact that the Q/S ratio is smaller than 1.0 indicates that a significant fraction, typically $\sim 25\%$ of the scintillator signal

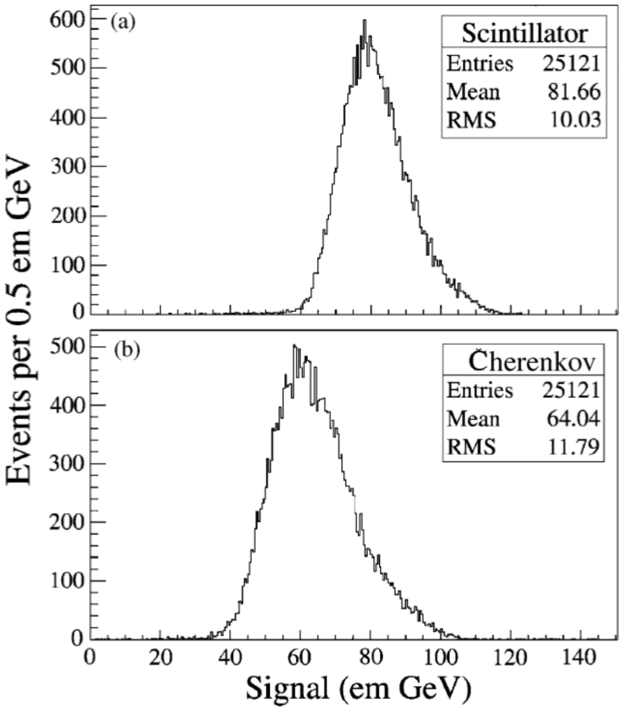

Figure 3.1.5: Signal distributions for 100 GeV π^- recorded by the scintillating (a) and Cherenkov (b) fibers of the DREAM calorimeter, oriented in the untitled position. The signals are set at the electromagnetic scale. [16]

from the pions showering in this detector is caused by non-relativistic particles, predominantly protons released from nuclei in spallation processes, or recoiling from elastic neutron scattering in the plastic fibers. The signals were corrected for the effect of shower leakage, which is estimated by studying the radial shower profiles event-by-event [16].

Exploiting the knowledge of the ratio of the Cherenkov (Q) to scintillation (S) signal, the value of the f_{em} could be obtained event-by-event. Indeed, the hadronic calorimeter response can be expressed in terms of the f_{em} as follows:

$$R(f_{em}) = f_{em} + \frac{1}{e/h}(1 - f_{em}) \tag{3.1}$$

Defined in this way, R=1 for em showers. Therefore the above mentioned ratio becomes:

$$\frac{Q}{S} = \frac{f_{em} + 0.21(1 - f_{em})}{f_{em} + 0.77(1 - f_{em})} \tag{3.2}$$

by use Equation 3.1 for copper/Cherenkov fibers ($e/h = 4.7$) and copper/scintillator ($e/h = 1.3$) structures. The merits of this method are shown in Figure 3.1.9 and Figure 3.1.10. Figure 3.1.9 shows the results for 200 GeV jets.

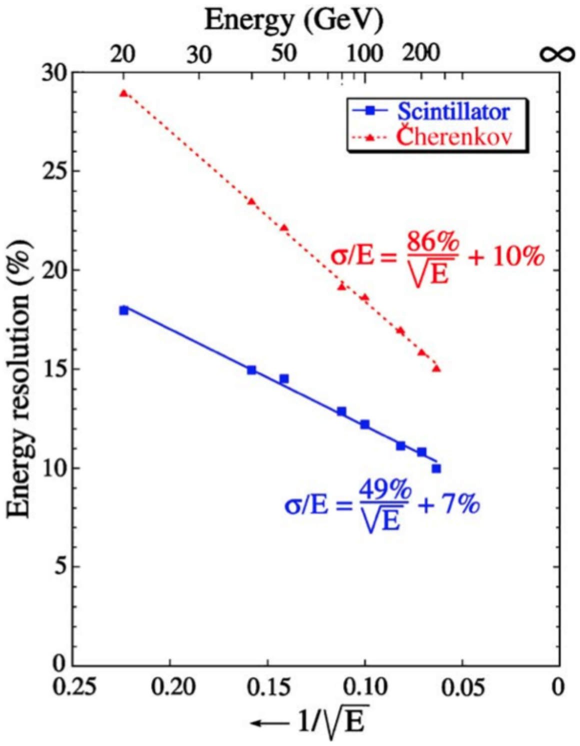

Figure 3.1.6: The energy resolution of the DREAM detector for the scintillator and Cherenkov signals from single-pion showers, as a function of the pion energy. The lines represent the results of least-squares fits to the experimental data. [16]

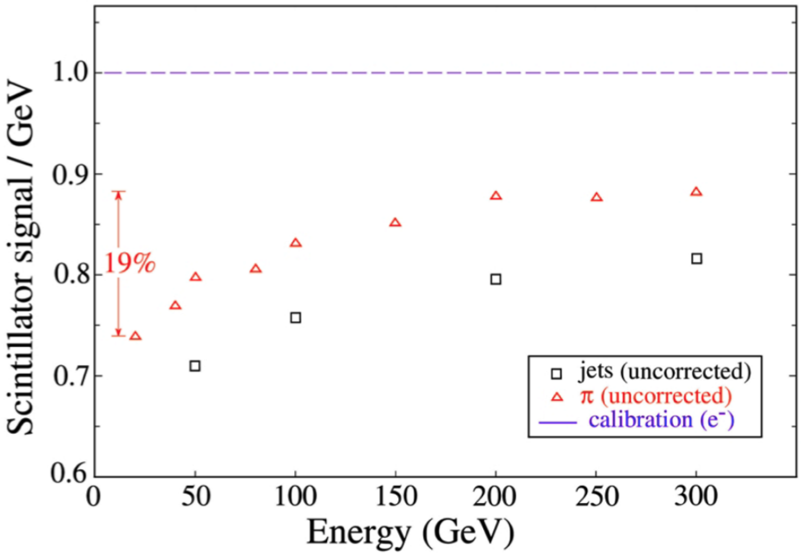

Figure 3.1.7: The scintillator response of the DREAM calorimeter to single pions and “jets” as a function of the beam energy. [16]

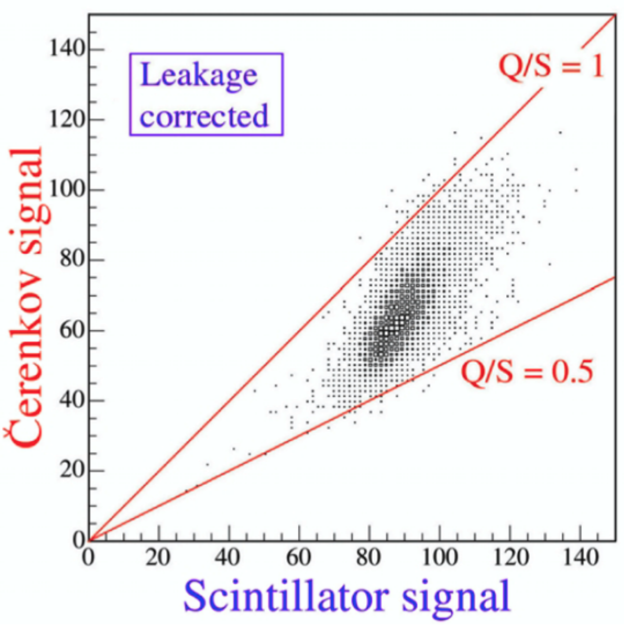

Figure 3.1.8: Cherenkov signals versus scintillator signals for 100 GeV negative pions in the DREAM calorimeter. These plots were derived from the raw data after applying corrections for shower leakage. See text for details. [16]

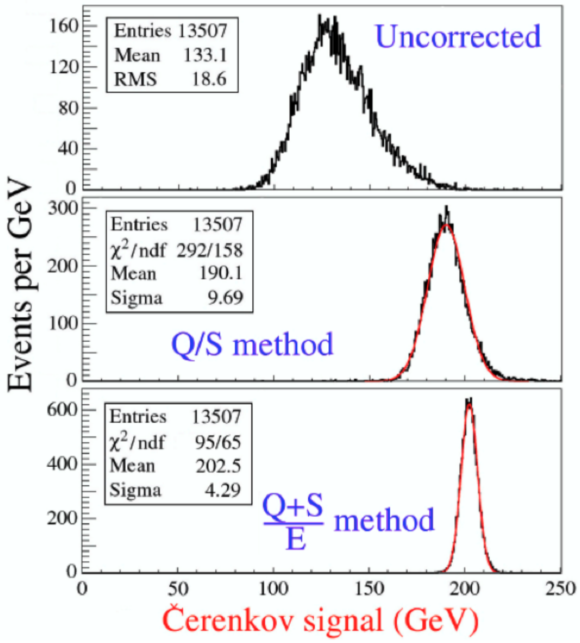

Figure 3.1.9: Cherenkov signal distributions for high-multiplicity “jets” in DREAM, before and after corrections on the basis of the Q/S ratio. In the bottom plot the knowledge of the beam energy is used and the effect of shower leakage is eliminated. [16]

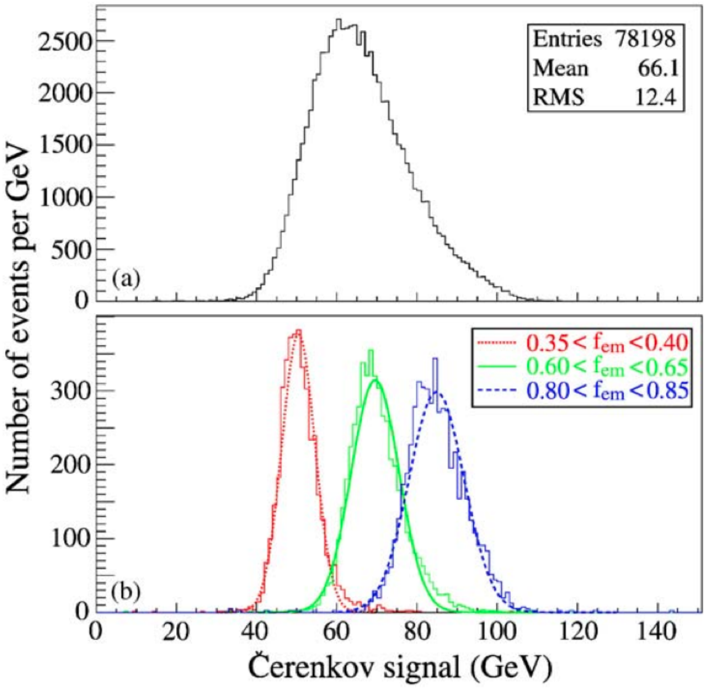

Figure 3.1.10: Cherenkov signal distribution for 100 GeV negative pions (a) and distributions for subsamples of events selected on the basis of the measured f_{em} value, using the Q/S method (b). [16]

The Cherenkov signal distribution becomes narrower, Gaussian and thus symmetric after the Q/S correction. After this correction the resolution for these jets was improved from 14% to 5%, in the Cherenkov channel. The energy resolution is thus largely improved by exploiting the knowledge of the Q/S ratio, since its measurement provides directly the value of f_{em} for each individual event.

Figure 3.1.10 shows instead how subsamples of events selected on the basis of the f_{em} value probes different regions of the Cherenkov signal distribution. The mean value of them increases with the f_{em} and the relative distributions are clearly more symmetric than the overall one.

After the Q/S correction, the calorimeter linearity improves considerably, as it is visible in Figure 3.1.11. This procedure led to hadronic energies that are correct within a few percent, in an instrument calibrated with electrons.

Because of the relatively small detector size (1200 kg), these results are dominated by fluctuations in lateral leakage. Moreover the poor light yield of both fibers gives rise to signal quantum fluctuations which give a large contribution to the energy resolution. By increasing the dimensions of the detector and by improving the light yield, its performance should improve.

However, Figure 3.1.9 and Figure 3.1.11 show that the dual-readout technique solves the problems associated with non-compensating

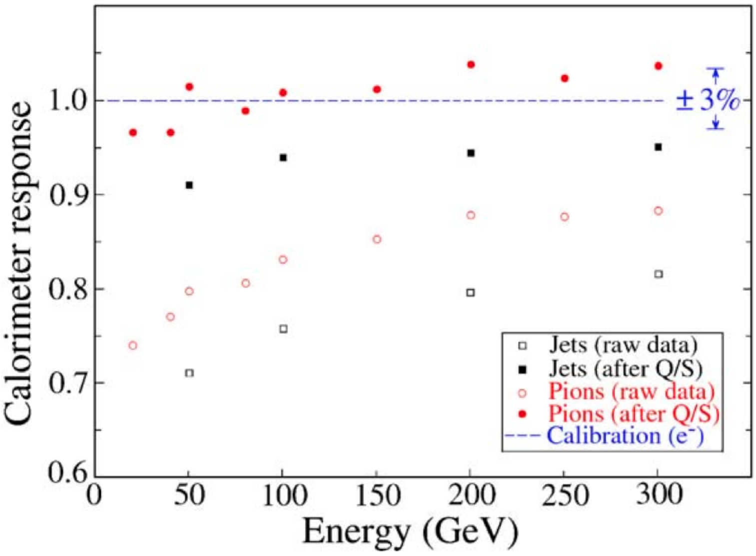

Figure 3.1.11: The calorimeter response to both single pions and high-multiplicity jets, before and after corrections made on the basis of the measured Q/S signal ratio. [16]

calorimeters, such as signal non-linearity and non Gaussian response function and offers a powerful method to improve hadron calorimeter performance.

Based on the mentioned results, obtained in the past seven years, a new fiber prototype has been constructed and tested in summer 2011. A number of changes have been made concerning the fiber type and arrangement in the absorber structure improving both the light yield and the sampling fraction.

3.1.3 *Measurement of the neutron fraction*

In the previous chapter we have discussed in depth the effects due to invisible energy. Once that the f_{em} fluctuations are eliminated through the Dual-Readout Method, and a detector sufficiently large in order to contain all the shower particles is built, nuclear breakup effects become dominant. Measuring the signal contributions from neutrons event by event is another aim of the DREAM Collaboration [20].

An estimation of the neutron contribution can be obtained by measuring the time structure of the scintillation signals event-by-event. Indeed neutrons appear as a tail with a characteristic decay constant, which depends on the mean free path of neutrons in the calorimeter ($\sim$ 20 ns in the fiber calorimeter). This tail is absent in the Cherenkov signals, which is clearly insensitive to neutrons, and also in the scintillation signals generated by em showers (see Figure 3.1.12.a).

One would expect an anti-correlation between the neutron fraction (estimated by integrating the tail over the proper time interval) and the Q/S ratio of the DREAM detector. Indeed, the larger is the em fraction,

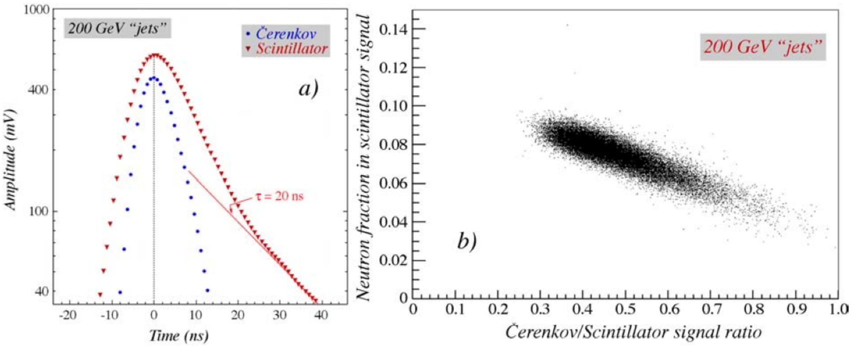

Figure 3.1.12: The average time structure of the Cherenkov and scintillation signals recorded for 200 GeV "jets" in the fiber calorimeter for 200 GeV jets (a). A scatter plot for 200 GeV jets: for each event, the combination of the total Cherenkov/scintillator signal ratio and the fractional contribution of neutrons to the total scintillator signal is represented by a dot (b). [4]

related to the Q/S ratio, the smaller is the non-em component of the shower, and thus the neutron fraction. This anti-correlation is visible in Figure 3.1.12.b, which thus shows that the long tail mentioned above represents the neutrons produced in the shower development.

Due to the fact that the em fraction and the invisible energy fluctuations are the main contributions to hadronic energy resolution, a measurement of these two quantities could bring to a very good hadronic energy resolution.

From the above results it looks like dual-readout detectors are optimal candidates for high-quality hadron calorimetry for all types of particles. We must also emphasize that the calibration of an hadron calorimeter is not an easy task. One of the benefits of dual-readout calorimeters is that these detectors can be calibrated just with electrons while, generally, an hadron calorimeter needs to be calibrated with hadrons and in the case of a segmented em/hadron calorimeter this is almost an impossible procedure [28].

3.2 DUAL-READOUT WITH CRYSTALS

The Dual-readout method can in principle be applied also to homogeneous calorimeters, as long as the signal is a mixture of both Cherenkov and scintillation light.

Apart from the shower leakage fluctuations, the energy resolution of the DREAM detector is also affected by fluctuations in the Cherenkov light yield, which contribute more than $35\%/\sqrt{E}$ to the measured hadronic energy resolution. Moreover, sampling fluctuations were measured to contribute $\sim 20\%/\sqrt{E}$ to the electromagnetic resolution, while were estimated to contribute twice as much for the hadronic resolution [4].

Certain dense high-Z crystals, such as $Bi_4Ge_3O_{12}$ (BGO), $Bi_4Si_3O_{12}$ (BSO) and $PbWO_4$, produce a relevant amount of Cherenkov light. In particular lead-tungstate crystals are characterized by a Cherenkov light yield of 50-60 photoelectrons per GeV. This means that fluctuations in the light yield give a smaller contribution to the hadronic energy resolution ($\sim 13\%/\sqrt{E}$) [23].

High-density scintillating crystals have been always the detectors of choice in experiments which require high-resolution measurements of electrons and photons. However, the application of the dual-readout principles in such a calorimeter may work only if one can detect simultaneously scintillation and Cherenkov signals also in the em section.

In order to apply the dual-readout method the scintillation and Cherenkov light produced in these crystals need to be separated and the calorimeter performance will depend on the precision with which the relative contributions of these two signals can be determined.

The scintillation and the Cherenkov light can be separated by exploiting their different characteristics (summarized in Table 3.2.1):

- *Differences in the time structure*: Cherenkov light is prompt while the scintillation process is characterized by one or more time constants, which determine the pulse shape. By integrating the signal in different gates, it is possible to distinguish the two contributions.

- *Differences in the spectral properties*: Cherenkov light exhibits a λ^{-2} spectrum while the scintillation spectrum is characteristic for the crystal under study. This difference can be exploited by using proper optical filters located between the crystal and the readout.

- *Differences in directionality*: Cherenkov light is emitted at a characteristic angle, while the scintillation light is emitted isotropically.

- *Polarization of the Cherenkov light*: the Cherenkov light can be separated from the scintillation one also by means of polarization filters.

	Cherenkov light	Scintillation light
Time structure	Prompt	Exponential decay
Light spectrum	$1/\lambda^2$	Characteristic peaks
Directionality	Cone: $cos\theta_c = 1/\beta n$	Isotropic
Polarization	Polarized	Unpolarized

Table 3.2.1: Different properties of Cherenkov and Scintillation light.

Therefore, a "perfect" crystal for dual-readout application should have a scintillation decay time of tenth of ns and a scintillation spectrum which peaks far from the bulk of Cherenkov radiation.

Concerning the polarization of the Cherenkov light, I have studied its characteristics at different stages of the electron shower development, by installing a polarizer filter with the transmission axes favorable to the Cherenkov light polarization. Indeed, the Cherenkov light is emitted by a medium that is traversed by a relativistic charged particles. The medium's atoms are excited and polarized in this process. They emit coherent radiation at a characteristic angle θ_C with respect to the particle track. The polarization vector of this radiation is oriented perpendicular to the direction in which the photons travel, i.e. perpendicular to a cone whose central axis is the particle track. This analysis will be discussed in details in chapter 4.

It is important to note that the difference in directionality between the two type of light cannot be exploited in a realistic 4π experiment. Indeed crystals has to be oriented at a definite angle, i.e. the Cherenkov angle, with respect to the direction of the incoming particles in order to observe the mentioned asymmetry. Moreover, in the late stages of a shower, particles are mostly emitted isotropically. These aspects are illustrated by Figure 3.2.1. In this plot the anisotropy in the angular dependence of the signals is shown by the (R-L)/(R+L) ratio, which represents the asymmetry of the Cherenkov light emission: the circles represent the asymmetry as measured in the normal configuration, i.e. with beam particles showering in the crystal. The triangles represent the asymmetry as measured in the configuration called "late", i.e. beam particles start showering in the block of lead located upstream the crystal. As it clearly visible, the asymmetry decreases in the late stages of the shower development.

3.2.1 *Experimental setup and analysis methods*

Many studies on the mentioned differences between the two types of light have been carried out in testbeams performed at the CERN SPS with electron and pion beams. The DREAM Collaboration have tested $PbWO_4$ crystals doped with different ions, BSO and BGO crystals, and the same analysis described below has been done for all of them. Since I have analyzed mostly data on lead-tungstate crystals, I will discuss the analysis on the experimental results obtained with this type of crystal.

The experimental setup is shown in Figure 3.2.2. The light generated by particles which traversing the crystal is readout by two PMTs, located at the opposite ends. The crystal is mounted on a platform which can rotate around its vertical axis and the particle beam hits the crystal in its center. The two signals are measured for different orientations of the crystal with respect to the beam, i.e. as a function

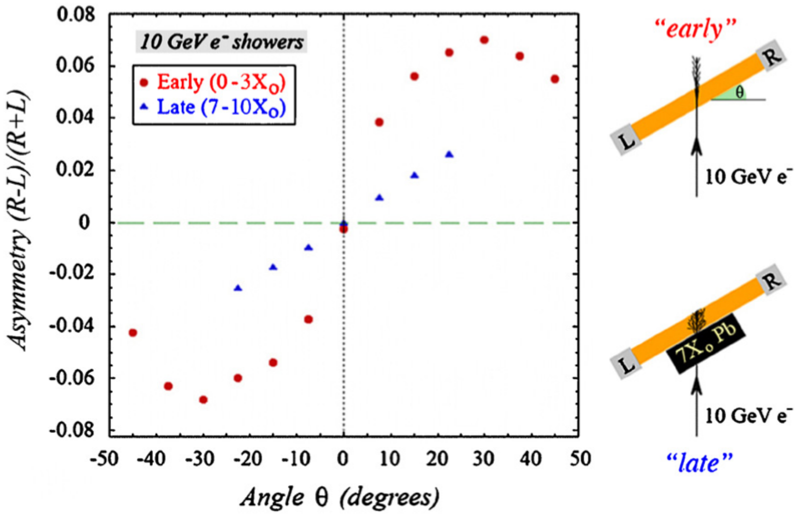

Figure 3.2.1: The response asymmetry measured for 10 GeV electrons showering in a 2.5 X_0 thick $PbWO_4$ crystal, as a function of the orientation of the crystal. Results are shown for the early and the late components of the showers. The latter measurements were obtained by placing 4 cm of lead upstream of the crystal [18].

of the angle θ (see Figure 3.2.2), in order to study the difference in directionality.

Cherenkov light has a maximum in one of the two PMTs when the crystal is oriented at the "Cherenkov" angle, i.e. $\theta = 30°$ for Right PMT or $\theta = -30°$ for Left PMT. The opposite angle is called the "anti-Cherenkov" angle. In Figure 3.2.3 the average time structure of the Cherenkov signals at these angles is shown. Clearly, the amplitude of the signal at the Cherenkov angle is larger than that at the anti-Cherenkov angle. In this figure it is also shown the result of subtracting the signal observed at $\theta = 30°$ and $\theta = -30°$. The resulting pulse (inverted) represents the calorimeter response function to the (prompt) Cherenkov component alone.

A very useful figure of merit for checking the separation power between the two types of light is the Cherenkov/scintillation ratio (C/S) as a function of the rotation angle, as shown in Figure 3.2.4. This ratio is strongly dependent on the angle of incidence and reaches a maximum near $\theta = 27°$, i.e. precisely where one would expect the Cherenkov signal to reach a maximum since Cherenkov light is emitted at an angle of 63° by ultra-relativistic particles traversing this crystal (the index of refraction of lead-tungstate crystal is n = 2.2).

It is important to note that in Figure 3.2.4.a there is a small bump near the anti-Cherenkov angle, which is absent in Figure 3.2.4.b. This bump is the result of Cherenkov light that was reflected from the side where the yellow filter was mounted, and detected at the opposite side (UV side). Since it arrives somewhat later at the PMT, this effect

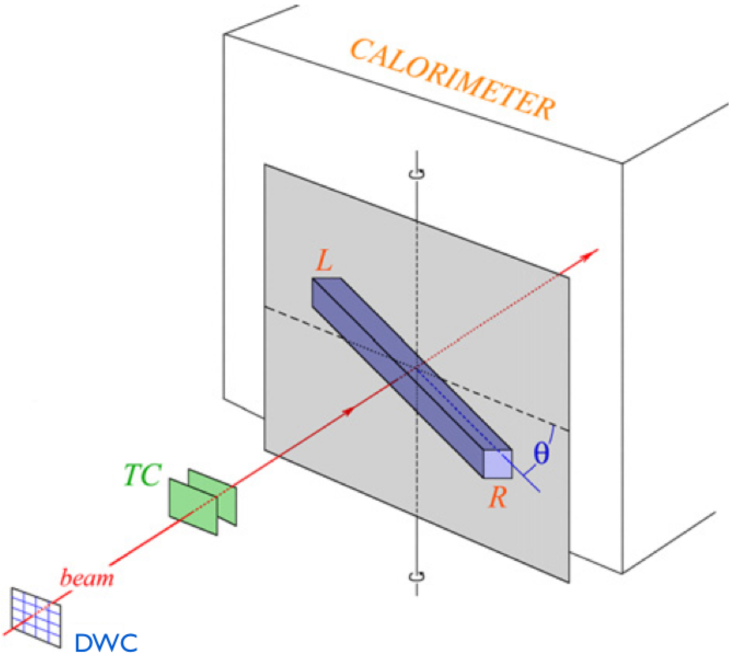

Figure 3.2.2: Experimental setup used for crystals test. The angle θ is negative when the crystal is oriented as drawn here [19].

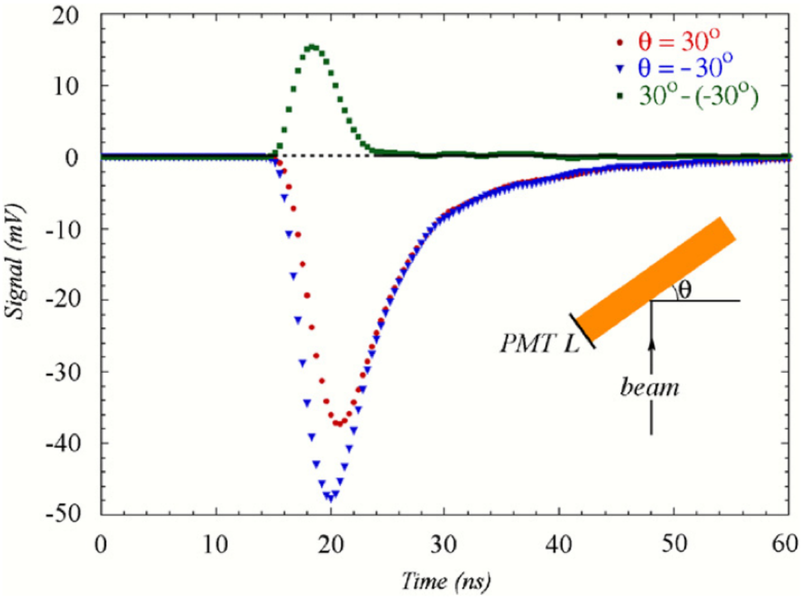

Figure 3.2.3: Time structures of the PMT L signals from 50 GeV electrons traversing the $PbWO_4$ crystal at angles $\theta = 30°$ and -30° respectively, and the difference between these two time distributions [33].

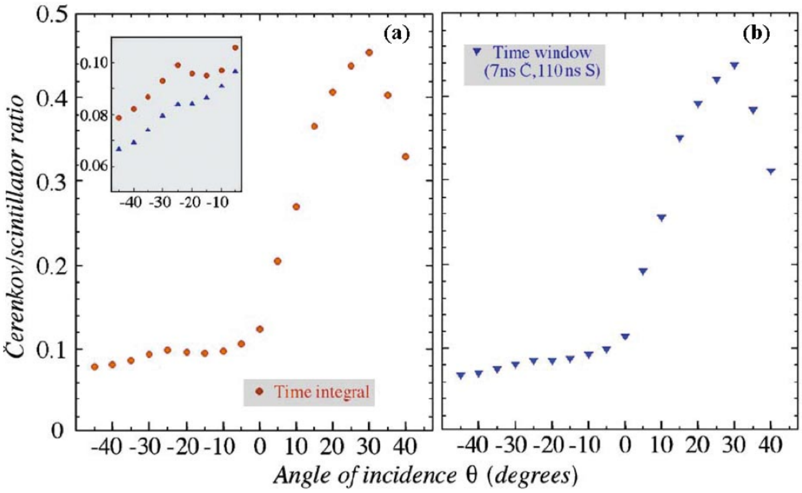

Figure 3.2.4: The C/S ratio as function of the angle θ for lead-tungstate crystals (undoped). The signals were obtained either by integrating over the full time structure (a), or over a limited time interval chosen such as to purify their Cherenkov or scintillation content (b). See text for details.[23]

is not visible in Figure 3.2.4.b, where a very narrow gate was used to select the Cherenkov signal.

Another way to show the anisotropy in the angular dependence of the signals is through the (R-L)/(R+L) ratio, where R and L are the average signals from the Right (Cherenkov) and Left (Scintillation) PMTs, respectively.

The response uniformity along the crystal is studied by means of a longitudinal scan: the beam particles hit the crystal at different distances from PMTs and the light attenuation along the crystal is investigated.

One of the reasons why we started studying crystals as dual-readout calorimeters was the very low Cherenkov light yield of quartz/clear fibers in the DREAM module. Therefore, it is very important to determine the Cherenkov light yield of the crystals under tests.

Figure 3.2.5 illustrates the method through which the energy resolution, as a function of the energy deposited, is estimated. It is assumed that, for a given amount of energy deposited in the crystal, the fluctuations in the number of scintillation photons are negligible compared to those in the number of Cherenkov photons. If this assumption is not correct, thus the Cherenkov light yield obtained in this way is a lower limit. By integrating the scintillation signals over the entire time structure the energy deposited is estimated. For the analysis, data obtained with 50 GeV electrons with the crystal oriented at the Cherenkov angle are used since, in this configuration, Cherenkov photons reach a maximum. The relation between the ADC counts and the amount of energy deposited is given by a Monte Carlo simulation. Figure 3.2.5.a shows the event-by-event distribution of the

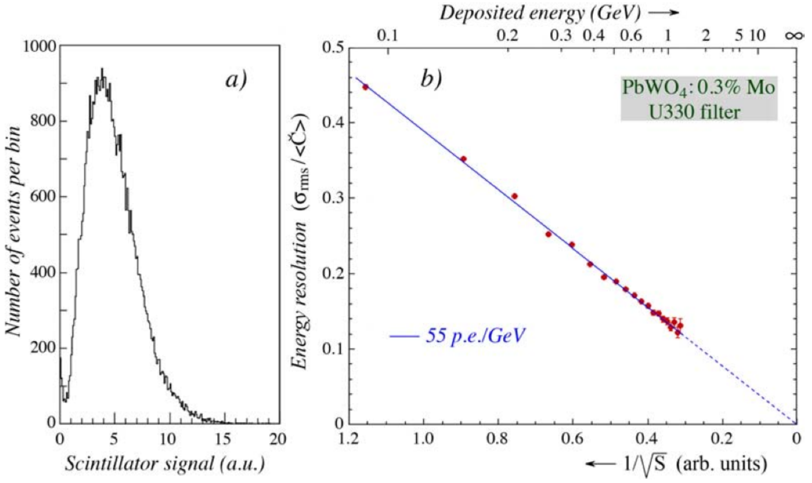

Figure 3.2.5: The scintillator signal distribution for 50 GeV electrons traversing the crystal at $\theta = 30°$(a) and the fractional width of the Cherenkov signal distribution as a function of the amount of energy deposited in the crystal, as derived from the scintillator signal (b). The $PbWO_4$ crystal was doped with 0.3% Mo [23]. See the text for more details.

energy loss by the showering electrons. This distribution is subdivided in bins and for each of them the signal distribution of the Cherenkov light is measured. The fractional width of this distribution, σ_{rms}/C_{mean}, is plotted in Figure 3.2.5.b as a function of the average scintillation signal in the given bin. It is visible that this fractional width scales perfectly as $E^{-1/2}$. This means that the energy resolution is completely determined by stochastic processes. In this case, only fluctuations in the Cherenkov light yield play a role and so the Cherenkov light yield can be estimated. In the case of $PbWO_4$ crystals doped with 0.3% Mo the light yield is 55 p.e. per GeV deposited energy.

3.2.2 *Experimental results with $PbWO_4$ crystals*

The separation of the calorimeter signals into Cherenkov and scintillation components works best if the contributions of both components are of the same order of magnitude. Most of the crystals have a very large scintillation light yield and are not suitable for dual-readout purposes since the Cherenkov component is too small. Lead-tungstate crystals proved to be the best choice, since the scintillation light yield is smaller than other crystals. Indeed the Cherenkov light contributes up to 15% to the signals, at room temperature.

Unfortunately, lead-tungstate crystals show some disadvantages. The scintillation light is predominantly blue and thus separating the two types of light by means of optical filters is not optimal in order to distinguish the two light components since their spectral region are too close. Moreover the decay of the $PbWO_4$ scintillation light is very fast ($\tau \leq 10ns$) and it is thus hard to distinguish the two components by exploiting the different time structure. Both problems can be solved by doping lead-tungstate crystals with small percentages of impurities. Indeed, impurities shift the peak of the scintillation light to longer wavelengths and increase the scintillation decay time.

The DREAM Collaboration tested first $PbWO_4$ doped with praseodymium (Pr), with three concentration levels (0.5%, 1%, 1.5%). These crystals had a length of 20 cm, a cross-section of 2.0x2.0 cm^2. The scintillation process was unacceptably slow (scintillation components in the μs range) and made this dopant not suitable for dual-readout calorimetry.

Then, $PbWO_4$ crystals with different Molybdenum concentration levels (from 0.1% to 5%) have been tested and they resulted to be promising [23].

An UV filter was positioned between the crystal and the PMT from which the Cherenkov signal was measured while the scintillation side was equipped with a yellow filter. In this way the different time structure of the two components can be exploited to separate them. Three types of UV filters were also tested in order to choose the one which optimizes the figures of merit described above.

In Figure 3.2.6 the emission spectra and the absorption coefficient as a function of wavelength are shown. As the Mo concentration increases, scintillation emission and the self-absorption cutoff shift to longer wavelengths. In Figure 3.2.6.b the cutoff wavelengths of the three UV filters are also indicated: 390 nm, 400 nm and 410 nm for UG11, U330 and UG5, respectively.

The strength, the purity and the attenuation of the Cherenkov light resulted to depend on the narrow bandwidth between the self-absorption edge and the cutoff of the transmission filter. In particular a measurement of the attenuation of the two light components showed that the scintillation was almost independent on the impact point, while the signals on the UV-filter side decreased with the distance (see Figure 3.2.7).

In Figure 3.2.7.a the results of a position scan are shown. 50 GeV electron beam was moved in steps of 2 cm along the longitudinal axis of the crystal, doped with 0.3% Mo in this case. The light is attenuated by only 10% in the case of the U330 and UG5 filter, as it is visible in Figure 3.2.7.b. On the other hand, the UG11 filter transmitted about an order of magnitude less light than the U330 and UG5 filters since it has a self-absorption cutoff very close to the UV absorption edge (see Figure 3.2.6.b). Concerning the effects of Mo concentration, as the Mo concentration decreases, the effect of light attenuation decreases since the self-absorption edge is lower (Figure 3.2.8.b).

In order to decide which UV filter and Mo concentration had to be used, the analysis of the C/S ratio and Cherenkov light yield was also carried out.

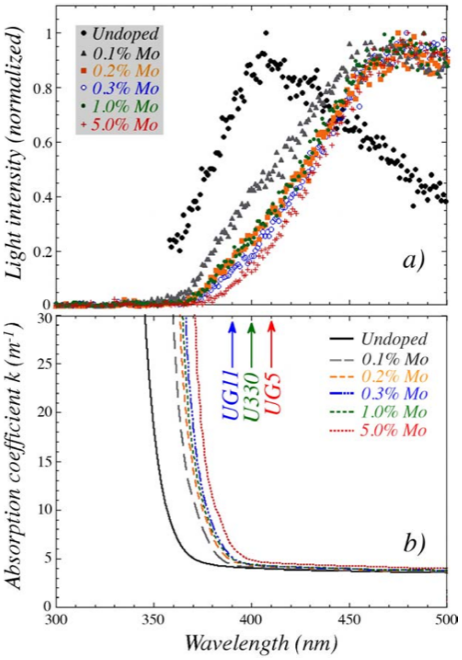

Figure 3.2.6: Normalized emission spectra for $PbWO_4$ crystals doped with different fractions of molybdenum, measured with radio luminescence (a). The absorption coefficient as a function of wavelength, for $PbWO_4$ crystals doped with different fractions of molybdenum (b). The cutoff wavelengths of the three UV transmission filters are also indicated [23].

In Figure 3.2.8.a the asymmetry response as a function of the Mo concentration is shown, for the three different UV filters. As the Mo concentration increases, the C/S ratio increases too, since the scintillation emission starts at longer wavelength and there is less contamination.

Concerning the light yield, the results obtained for different filters and Mo concentrations are summarized in Table 3.2.2. In order to estimate the light yield the method discussed in Section 3.2.1 was exploited. The light yield and the attenuation performances disfavored the UG11 filter, while the U330 and UG5 filters gave comparable results. High concentrations of Molybdenum gave the worst results in almost any respects while 0.1%-1% concentrations seemed to be suitable for dual-readout technique purposes. In particular lead-tungstate crystals doped with 0.3% Mo have revealed optimal, both for spectral separation and temporal response.

It is important to point out that the above results were obtained by testing only one crystal for each value of Mo concentration. In order to prove the accuracy of these results it is necessary to repeat the measurements on many identical crystals. In this context, I have carried out within the Pavia DREAM group a systematic analysis of eight lead-tungstate crystals doped with 0.3% Mo concentration. After the analysis of their response, seven of these crystals were arranged

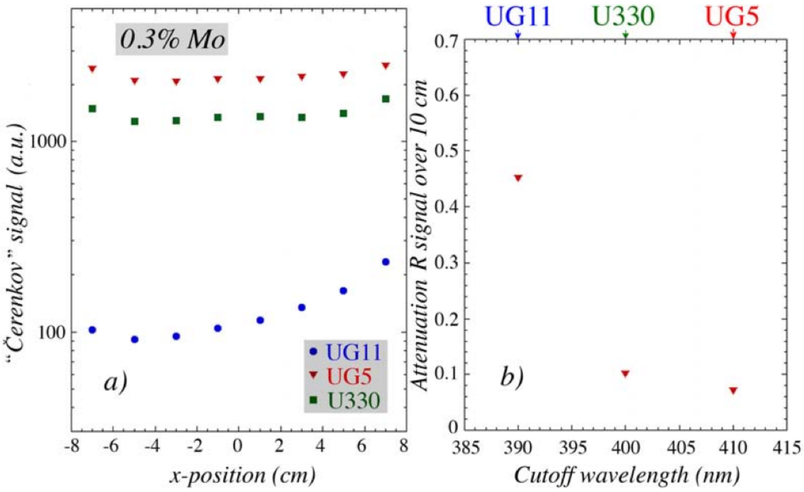

Figure 3.2.7: The position dependence of the Cherenkov signal (Right PMT) for different filters used and with Mo concentration of 0.3%(a). The relative change in the R signal over a distance of 10 cm, for different filters used to enhance the relative Cherenkov contribution to the R signal (b). [23]

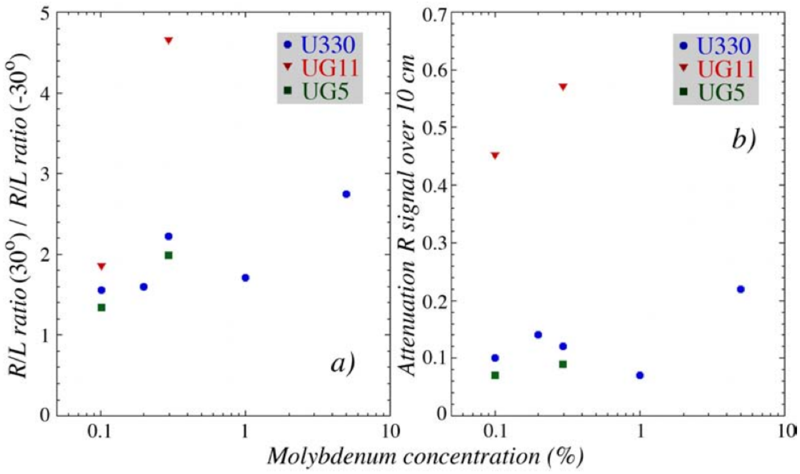

Figure 3.2.8: The ratio of the R/L signal ratios measured at $\theta = 30°$ and $\theta = -30°$ (a), and the relative change in the R signal over a distance of 10 cm (b), as a function of the molybdenum concentration in the $PbWO_4$ crystal [23].

	UG11	U330	UG5
0.1% Mo	4.6	62.1	
0.2% Mo		57.7	
0.3% Mo	5.9	55.3	64.9
1% Mo		58.3	
5% Mo		38.3	

Table 3.2.2: Cherenkov light yield measured for lead-tungstate crystals doped with different fractions of molybdenum and for different filters, with 50 GeV electrons traversing the crystal at 30°. The results are given in p.e. per GeV [23].

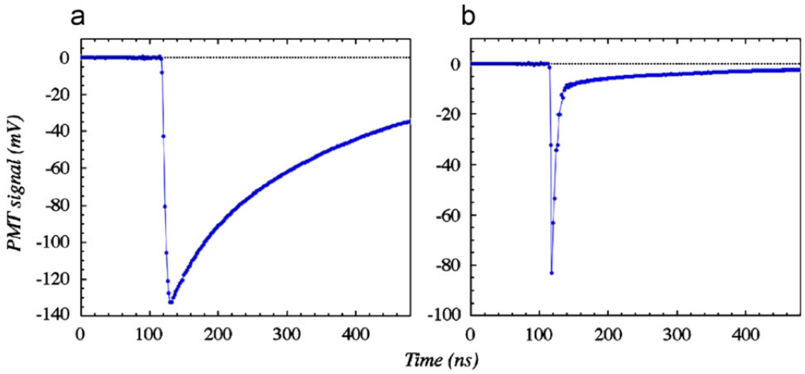

Figure 3.2.9: The time structure of a typical shower signal measured in the BGO crystal equipped with a yellow filter (a), and with a UV filter (b). These signals were measured with a sampling oscilloscope, which took a sample every 2 ns in this case. [18]

as a matrix and tested in detail. In **??**, both the systematic study of the eight crystals and the preliminary analysis of the $PbWO_4$ matrix are discussed.

3.2.3 *Experimental results with BGO crystals*

A totally different type of crystal, bismuth germanate (BGO) was also tested by the DREAM Collaboration. This crystal is very bright and so the Cherenkov light contributes considerably less (1%) than in lead-tungstate crystals. However, the separation of the two light components is made easier since the scintillation light is characterized by a longer time constant with respect to $PbWO_4$ crystals. An UV filter is positioned between the crystal and the PMT from which the Cherenkov signal is measured while the other side is equipped with a yellow filter, as before.

The time structure of the two signals is shown in Figure 3.2.9. In the UV filter side it is visible the sharp peak due to the Cherenkov light and a long tail due to scintillation one. This tail has the same

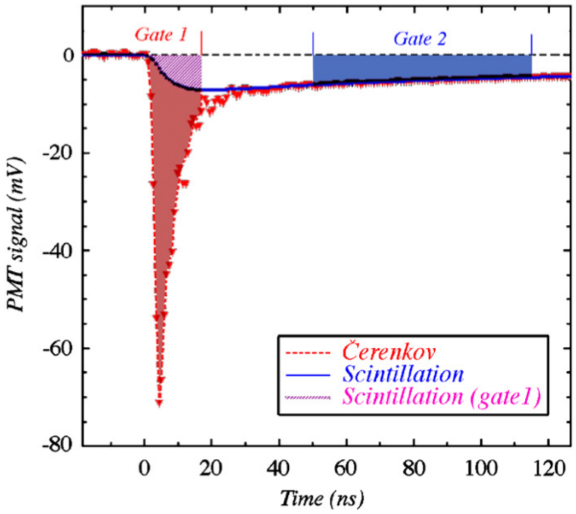

Figure 3.2.10: The UV BGO signals were used to measure the relative contributions of scintillation light (gate 2) and Cherenkov light (gate 1) [33]. See text for details.

characteristic time structure as the pure scintillation signals (yellow filter side). Therefore the signals transmitted through the UV filter contain event-by-event information about both the Cherenkov and the scintillation contributions. This feature allows to exploit only one readout channel, making easier to use this technique in a real experiment, where a two-sided readout would be very difficult to put into practice. A single-side analysis with BGO crystals has been carried out, as it is shown in Figure 3.2.10. The two contributions can be disentangled by integrating on two different time intervals, i.e. gate 1 for the Cherenkov signal and gate 2 for the scintillation one. As it is visible in Figure 3.2.10, there is some contamination of scintillation light in the signals from gate 1. By exploiting the knowledge of the scintillation pulse shape (see Figure 3.2.9.a), the scintillation tail can be fitted and thus the contamination can be estimated event-by-event.

This method has been tested in several measurements in which the DREAM fiber calorimeter was preceded by 100 BGO crystals, as it is described below.

3.2.4 *Combined calorimetry*

The DREAM Collaboration has tested an hybrid calorimeter constituted by 100 BGO crystals (the em section) and the DREAM fiber prototype (the hadronic section). The hadronic showers are not contained in the em section, because of its small dimension, and large signals may be generated only by π^0s produced in the early stages of the hadronic shower development. Therefore, large Cherenkov and scintillation signals will be generated also in DREAM. It is thus rea-

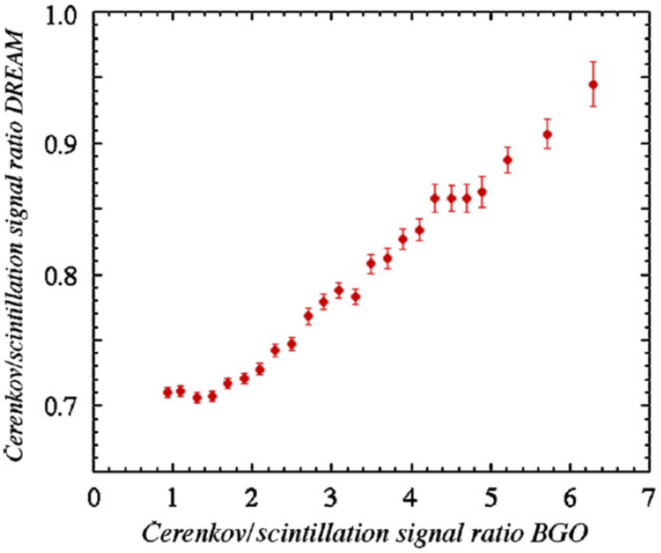

Figure 3.2.11: The Cherenkov/scintillation signal ratio of the DREAM calorimeter, for 200 GeV π^+ starting a shower in the BGO crystal, as a function of the Cherenkov/ scintillation signal ratio of the BGO signal [33].

sonable to expect a correlation between the C/S ratios in both sections of the calorimeter system, as Figure 3.2.11 shows.

The C/S ratio is a measure for the em fraction f_{em} for both the BGO matrix and the DREAM module. Even if the e/h values of the two sections are different and the energy sharing between these sections varies event by event, a simultaneous measurement of the Cherenkov and Scintillation light in both sections allows to measure the em fraction event-by-event.

This is illustrated in Figure 3.2.12, which shows the total distribution of the Cherenkov signal (Figure 3.2.12 (top)) and the distributions for subsets of events selected on the basis of the C/S ratio in this detector combination (Figure 3.2.12 (bottom)). The total distribution is broad and asymmetric, reflecting the characteristics of the em shower fraction fluctuations. The subsets of events are instead narrower and Gaussian, as was observed in the fiber calorimeter in stand-alone mode.

These results were obtained even if the crucial properties of the BGO matrix were far from ideal. Poor light collection, due to the inadequacies of the readout, and response non-uniformity due to the characteristics of the BGO crystals used, limited the improvement of the energy resolution and do not allow to reconstruct completely the energy of the showering hadrons.

The same configuration have been tested in summer 2011 with a small lead-tungstate matrix as the em section. Preliminary results of this new hybrid calorimeter prototype will be shown in **??**.

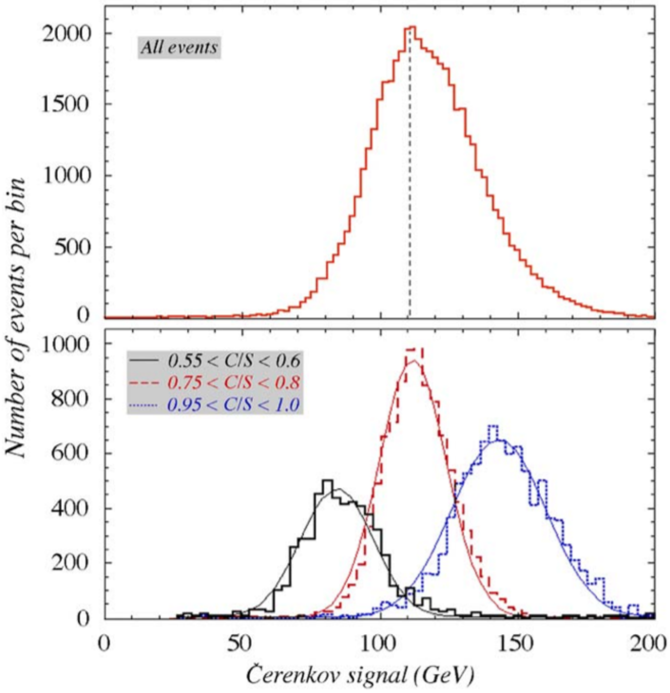

Figure 3.2.12: The Cherenkov signal distribution for 200 GeV "jet" events detected in the BGO+fiber calorimeter system (top) together with the distributions for subsets of events selected on the basis of the ratio of the total Cherenkov and scintillation signals in this detector combination (bottom).[33]

4

DATA ANALYSIS ON LEAD-TUNGSTATE CRYSTALS AND POLARIZATION MEASUREMENTS

During my thesis work I participated in the DREAM research program and in particular I contributed to both the data taking at testbeams and to the data analysis. I focused on the crystals study and the results that I have obtained are summarized in the following.

4.1 SYSTEMATIC ANALYSIS OF EIGHT LEAD-TUNGSTATE CRYSTALS DOPED WITH 0.3% MOLYBDENUM

As mentioned before, the properties of the $PbWO_4$ crystals doped with different Molybdenum concentrations were studied by testing only one crystal for each value of Mo concentration [23]. In order to prove the accuracy of the obtained results, the same measures on many identical crystals had to be repeated.

In this context, eight $PbWO_4$ crystals, doped with 0.3% Mo, were tested in the H8 beam line [1] at the CERN SPS in july 2010. Crystals were wrapped with mylar in order to avoid photon contamination from outside and contain photons produced inside. These crystals were exposed to 180 GeV π^- beam and the signals generated inside them were unraveled into the scintillation and the Cherenkov components, by exploiting the time structure and the spectral properties. The experimental setup, the analysis method and the results achieved are described below.

4.1.1 *Detectors and experimental setup*

The crystal under study was inserted in a box, which had appropriate supports to hold a PMT at both sides of the crystal. The two PMTs read out the light produced by particles traversing the crystal. In Figure 4.1.1 the crystal box and the experimental setup are shown. Each crystal had a length of 20 cm and a cross section of 3.0x3.0 cm^2.

For the scintillation readout a yellow filter (known as GG495), which transmitted only light with wavelength longer than the cutoff value (495 nm), was used. For the Cherenkov readout an UV filter (U330) was chosen, in order to increase the relative fraction of Cherenkov light transmitted. These filters, 3 mm thick and made of glass, were coupled to the crystal and to the PMT by means of elastocil (silicone) "cookies" (n=1.403), which reduced the light trapping effect caused by the large refractive index of lead-tungstate (n=2.19).

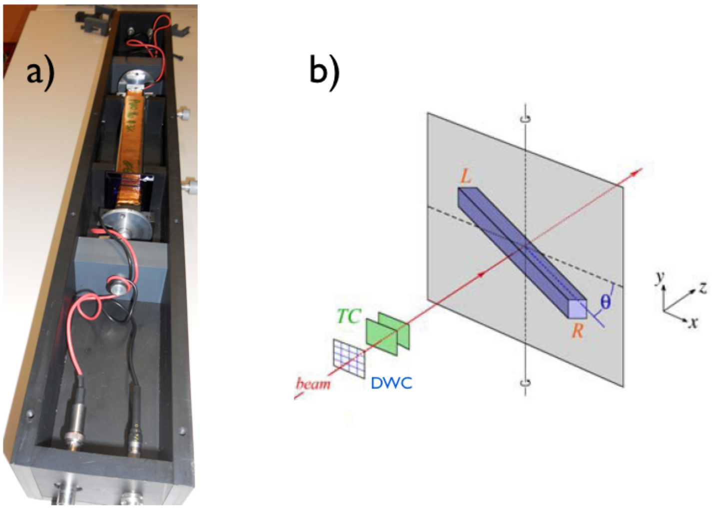

Figure 4.1.1: a) The lead-tungstate crystal optically coupled with PMTs (see text for details). b) the experimental setup in which the beam tests of the crystals were performed.

PMT	filter	light detected	downstream	upstream
R	UV (U330)	C	$\theta = 30°$	$\theta = -30°$
L	Y (GG495)	S	$\theta = -30°$	$\theta = 30°$

Table 4.1.1: The experimental configuration and the readout channel for Cherenkov and scintillator light.

The crystal box was mounted on a platform that could rotate around a vertical axis. The crystal was oriented in the horizontal plane and the rotation axis went through its geometrical center, on which the particle beam was steered. The angle θ (see Figure 4.1.1) represents the angle between the crystal axis and a plane perpendicular to the beam line. The angle increases when the crystal was rotated such that the crystal axis L–R approached the direction of the traveling beam particles. The crystal orientation shown in Figure 4.1.1 corresponds to $\theta = -30°$. In many measurements, θ was chosen to be +30°, since in that case the fraction of the total generated Cherenkov light that was detected in PMT R, as well as the relative Cherenkov content of the signals from this PMT, was maximized. Table 4.1.1 summarizes the experimental configurations.

In order to trigger the data acquisition system, two small scintillation counters (TC) were positioned upstream the crystal. These trigger counters were 2.5 mm thick and the area of overlap was 4x4 cm^2. The signals from these devices were put in coincidence, providing the trigger.

The beam profile in x and y coordinates could be reconstructed by a small Delay Wire Chamber (DWC) which was installed upstream of the trigger counters, as Figure 4.1.1 illustrates. The DWC works like a Multi Wire Proportional Chamber: a particle passing through the chamber ionizes the gas and creates free electrons and ions. The high voltage between anode and cathodes then accelerates the electrons towards the 20 μm anode wires, where avalanche multiplication takes place. Like most Multi Wire Proportional Chambers, the DWC is composed of a sandwich of two cathode planes surrounding a central anode wire-plane. The position information is taken from the cathode and data are acquired by a Time to Digital Converter (TDC). This system made possible to determine the location of the impact point of the beam particles with a precision of typically 200 μm. In order to calibrate a DWC, three series of data acquisitions are taken with the TDC by using a dedicating pulse generator: the chamber is excited at –30 mm, in the center and at +30 mm. In this way three reference points are obtained and the slopes and the offsets of their linear fit are estimated. By means of the relation: $X_{position} = \Delta t * Slope_{horizontal} + Offset_{horizontal}$ the timing information of the TDC is converted in mm (for the x coordinate). A similar relation is applied to obtain the y coordinate.

About 25 m downstream of the crystal, after the beam dump (about 20 interaction lengths), a 50x50 cm^2 scintillator paddle was used as a muon counter. The DREAM fiber module was placed immediately after the crystal and, in this study, its information were exploited only to recognize and eliminate beam impurities.

The average time structure of the Cherenkov and the scintillation signals was recorded for each run and 15 mm thick low-loss cables were used to transport the crystal signals to the counting room in order to limit distortion of the signal time structure. The same type of cables, shorter than the crystal signal ones, were used for trigger counters, which generate the gate and trigger the data acquisition.

A single VME crate hosted all the needed readout and control boards. The time structure of the signals was recorded by means of a Tektronix TDS 7254B digital oscilloscope, which provided a sampling capability of 5 GSample/s, at an analog bandwidth of 2.5 GHz, over 4 input channels. For this study, only two channels were used, in order to sample the signals from PMT R and L. The crystal signals were sampled every 2.0 ns, over a total time interval of 1064 ns (532 data points).

Beam particles were provided to the experiment during a spill of 9.6 s, with a repetition period of 48 s, given the bunch structure of the SPS cycle. This feature allowed to take data efficiently, thanks also to the optimization of the CPU utilization.

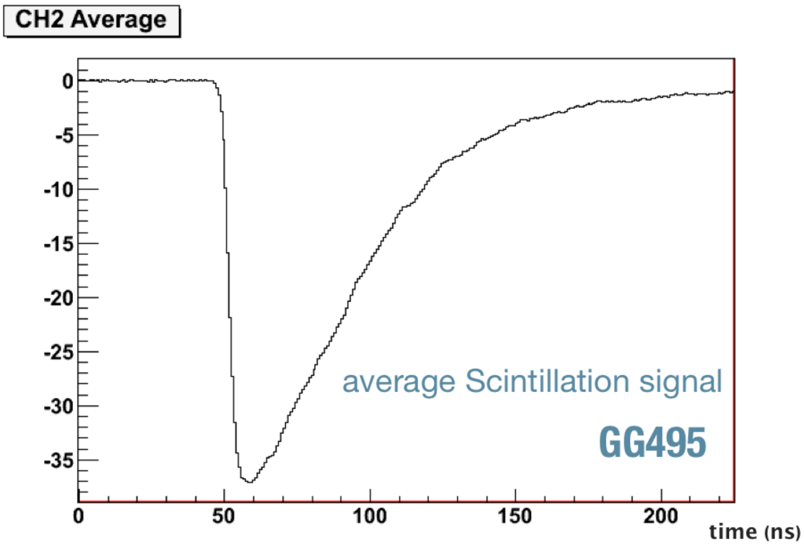

Figure 4.1.2: The average time structure of the scintillation signal from PMT equipped with the yellow filter, with the crystal oriented at +30°.

4.1.2 *Experimental data and analysis method*

In order to separate the two different types of light generated in the crystal, the average time structure of the scintillation and the Cherenkov light were estimated for each run and are shown in Figure 4.1.2 and Figure 4.1.3 respectively. The Cherenkov signal is clearly prompt while the scintillation one is characterized by a decay constant, as expected.

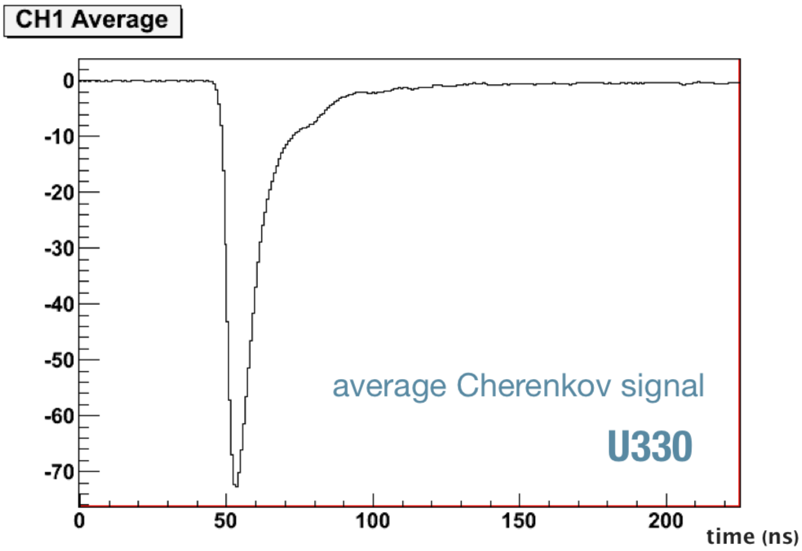

Figure 4.1.3: The average time structure of the Cherenkov signal from PMT equipped with the UV filter, with the crystal oriented at +30°.

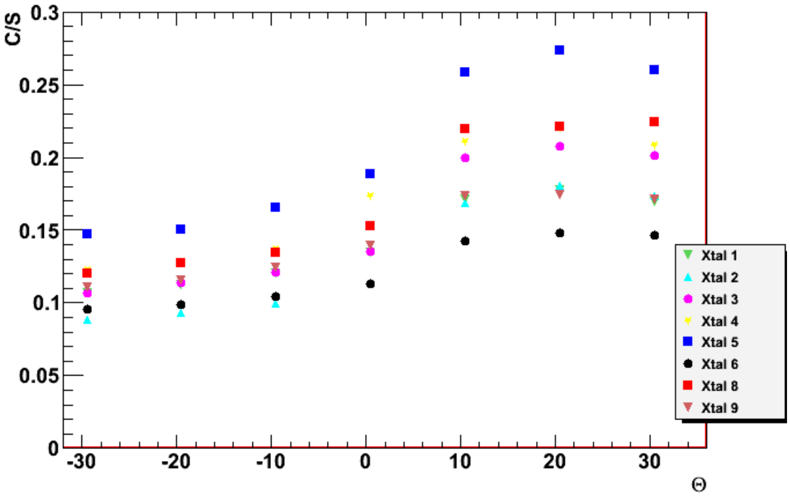

Figure 4.1.4: The C/S ratio as a function of the angle θ for all the crystals tested.

A study of the crystals response as a function of the angle θ was carried out. The angular scan was performed with a 180 GeV π^- beam. The angle θ between the crystal axis and the plane perpendicular to the beam line ranged from -30° to +30°. At each angle 30000-50000 events were collected. In addition, 3000-5000 randomly triggered events provided the pedestal information, which allowed to eliminate, off-line, the baseline. The Cherenkov and the scintillation average signals were integrated event-by-event in order to get the Cherenkov and scintillation ADC equivalent distribution for each event sample. The Cherenkov signal C was integrated only over a small time interval (25 ns) around the peak, while the scintillation signal S was integrated over the entire time structure. The ratio of these values (C/S) is shown in Figure 4.1.4 for all the crystals tested, as a function of θ. The ratio peaks near 27°, i.e. $90° - \theta_C$ where θ_C is the Cherenkov angle (about 63° for lead-tungstate). At the "anti-Cherenkov" angle, the ratio is twice smaller than that at the Cherenkov angle, and this is valid for all the tested crystals.

In order to evaluate the separation capability of the two different light components we used the following variable:

$$\Pi = \frac{(C/S)_{30°}}{(C/S)_{-30°}} \tag{4.1}$$

estimated for each crystals, where $(C/S)_\theta$ represents the C/S value at the θ angle. In Table 4.1.2 the results that I have obtained are summarized.

Comparing the C/S values with the one obtained last year with a similar crystal [23], $\Pi = 2.4$, it is possible to notice that there is poor agreement between the two results. In order to investigate the

crystal	Π	A	C light yield (a.u.)
1	1.59	0.16	1.05
2	1.96	0.15	1.12
3	1.89	0.14	1.00
4	1.70	0.14	0.97
5	1.77	0.17	0.89
6	1.54	0.18	1.10
8	1.87	0.15	0.96
9	1.55	0.18	1.08

Table 4.1.2: The Π ratio, the signal loss in 10 cm (A) of crystal and the Cherenkov light yield values for all the eight crystals tested. See text for details.

source of the mentioned disagreement, I analyzed the reproducibility measurements performed. Indeed, removing and putting the crystals in the box is a delicate operation because of the optical coupling between the crystal and the two PMTs. During this procedure, cookies may move or air bubbles may form between the cookie and the crystal and/or PMT contact surface. In order to understand how much these problems can affect measurements, the same crystal was tested many times, removing and replacing it each time between a measurement and the next one. It turned out that putting and taking-off the crystal introduced differences, between two measurements, within 5% in the case of scintillation and within 15% in the case of Cherenkov light. The conclusion is that small variations of the optical coupling can affect heavily the results, and it is thus necessary to pay attention when crystals are positioned in the box. These results present also variations from one crystal to another at the level of 20% in the case of the Cherenkov light. Crystallographic measurements will be carried out towards the end of 2011 in order to determine possible differences between the crystals in a more absolute way.

After the angular scan, a longitudinal scan was performed for all the tested crystals. The crystal box, oriented at 30° was moved along the longitudinal axis and the results of this position scan are shown in Figure 4.1.5 and Figure 4.1.6. In the regions near both PMTs, signals were anomalously large, since some particles may hit directly the PMTs, and were discarded for the analysis. The scintillation attenuation was almost negligible, while the Cherenkov light was affected by strong attenuation. This is due to the narrow gap between the self-absorption cutoff and the UV absorption edge of the $PbWO_4$ crystal 0.3% Mo doped (see Section 3.2.2).

In order to evaluate the light attenuation A, I estimated the Cherenkov signal loss in 10 cm as:

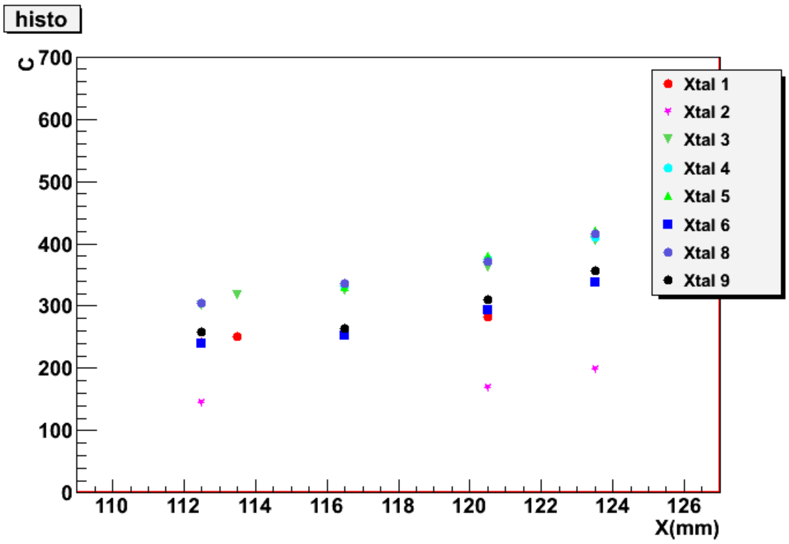

Figure 4.1.5: The integral of the Cherenkov signal as a function of the impact point of the beam, for all the crystals tested.

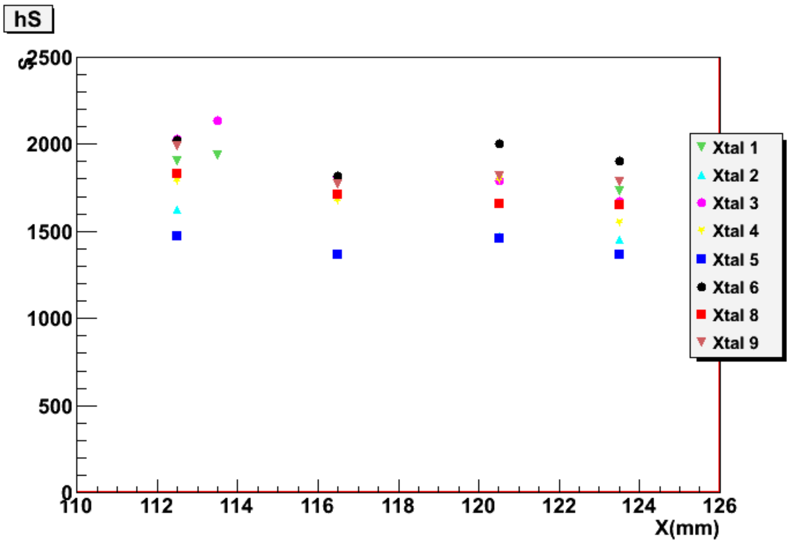

Figure 4.1.6: The integral of the scintillation signal as a function of the impact point of the beam, for all the crystals tested.

$$A(\%) = \frac{I(127) - I(117)}{I(127)} \tag{4.2}$$

where *I(x)* is the integral of the Cherenkov signal with the crystal at the x position (mm). The results are reported in Table 4.1.2. Each length is scaled by a factor $cos\theta$ in order to eliminate the path length dependence of the signals. Also for the light attenuation, there is poor agreement with the results discussed in the paper [23]: A=10%. As before, the optical coupling played a role and could partially justify the difference between the two results.

Finally, I have estimated the fractional width of the distribution of the Cherenkov signal σ_{rms}/C_{mean} for each crystal using the method discussed in Section 3.2.1: we divided the scintillation distribution in N bins and we look at the Cherenkov distributions in the event sample contained in each bin. By fitting these distributions, the σ_{rms}/C_{mean} is determined for each event sample, i.e. for each energy interval. Indeed, the scintillation signal integrated charge is used as a measure of the energy deposited in the crystal.

For the analysis, I have used data acquired with the crystal oriented at $\theta = 30°$ since in this configuration we have the maximum detection efficiency for the Cherenkov light.

The fractional width distribution for the crystal 2 is shown in Figure 4.1.7 as a function of the average energy deposited. Data were fitted with the following equation:

$$\frac{\sigma_{rms}}{C_{mean}} = p_0 + p_1 \frac{1}{\sqrt{S}} \tag{4.3}$$

Only statistical errors have been considered and were estimated by combining in quadrature the statistical errors of σ_{rms} and C_{mean}. It turned out that the fractional width distribution scales quite well with $S^{-1/2}$, i.e. $E^{-1/2}$. At high energies side leakage fluctuations strongly contribute to the energy resolution and hence deviations from the $S^{-1/2}$ scaling were observed.

Once the relationship between the energy released E and the scintillation signal S is estimated by means of a Monte Carlo (MC) simulation, the number of photoelectrons per GeV, i.e. the light yield, can be estimated from the parameter p_1. We have neglected fluctuations in the scintillation light yield, and since also other fluctuations may contribute as well, the assumption that all fluctuations are due to light yield leads to a lower limit.

In Table 4.1.2 the Cherenkov light yield value (in arbitrary units) for each crystals is reported. An absolute value has not been estimated yet. However, the aim of this analysis was to make a relative comparison of the crystal response and I focused mostly on the Π ratio and the signal loss.

We have discarded the crystal with the worst characteristics in order to assemble a seven crystals matrix for further tests. It constitutes

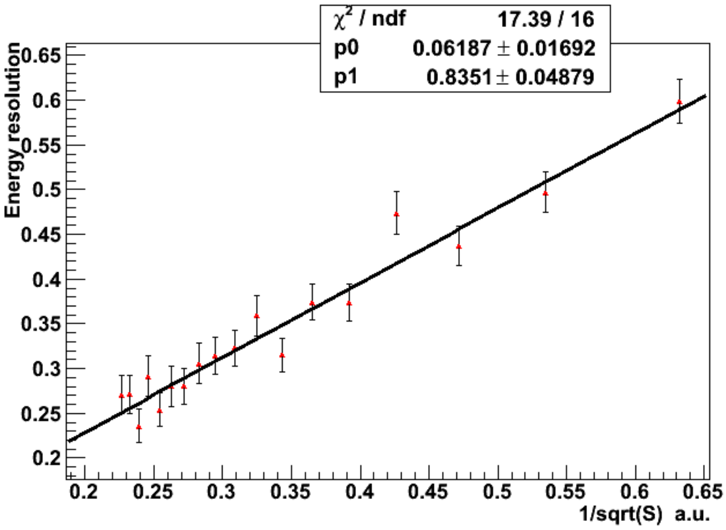

Figure 4.1.7: The fractional width distribution of the Cherenkov signal, i.e. σ_{rms}/C_{mean}, as a function of energy (a.u.) for crystal 2.

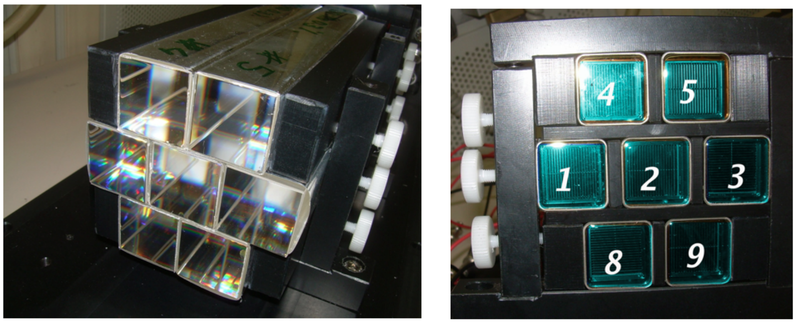

Figure 4.1.8: The $PbWO_4$ Mo doped crystals matrix. In the right photo, the position of each crystal, as seen by the beam, is shown.

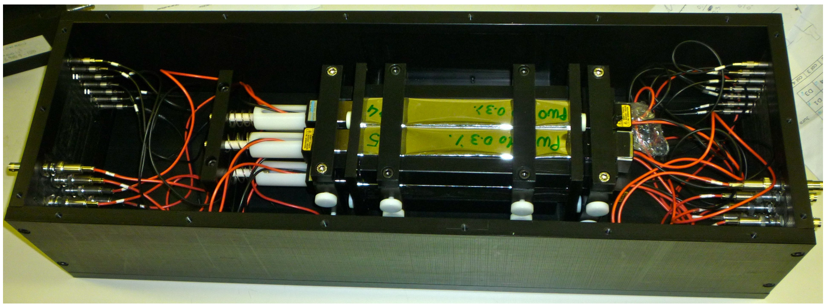

Figure 4.2.1: The matrix box. Each crystal is readout by two PMTs, and is wrapped with mylar (1 mm).

the electromagnetic section of a combined calorimeter. Crystal 6 was the one with the lower Π ratio and the higher signal loss and so we had decided to discard it. Crystal 2 was instead characterized by the higher Π ratio and it was thus placed in the center of the matrix, as it is shown in Figure 4.1.8.

This crystal matrix has been tested in October 2010 and in July 2011, as the em section of a combined calorimeter. The data analysis turned out to be very difficult due to the poor conditions of the electron beam (fundamental for the calibration procedure). The results achieved and the analysis methods are discussed in the next section, mainly based on the 2010 campaign.

4.2 THE ANALYSIS OF THE LEAD-TUNGSTATE CRYSTALS MATRIX

Each crystal in the matrix (see Figure 4.2.1) was readout at both sides with PMTs. A yellow and a UV filters were installed in order to separate the scintillation and the Cherenkov components by spectral properties. Time characteristics of the two components were exploited for this task, and the time structure of each signal was sampled with the CAEN V1742 board based on the Domino Ring Sampler (DRS) chip. This chip was characterized by high sampling frequency, which was crucial in separating the Cherenkov from the scintillation contribution. The quality of the sampled signal waveform are shown in Figure 4.2.3.

Data have been taken at the H8 SPS testbeam at CERN with pion and electron beams of different energies, and the calibration has been made with 80 GeV electrons. The matrix and the DREAM detector were placed on a platform which could move both horizontally and vertically, to allow for position scan. The crystal matrix was put in front of the DREAM fiber module as it is visible in Figure 4.2.2. The experimental setup is described in Section 4.1.1. For all the following measurement the crystal matrix is positioned with the crystal long axis parallel to the beam line. Moreover UV filter is positioned downstream while yellow filter upstream.

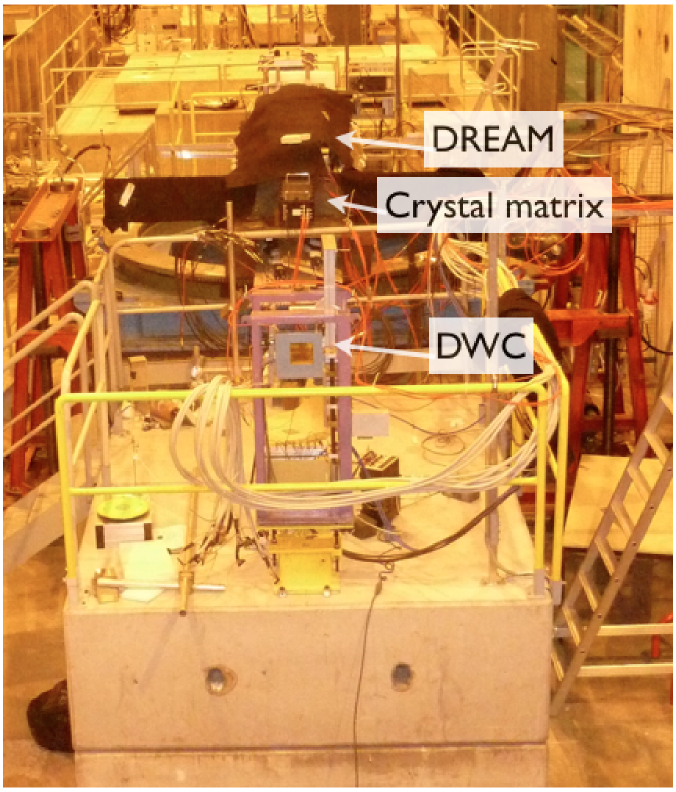

Figure 4.2.2: A picture of the experimental area as seen from the beam, in which the DREAM detector, the crystal matrix and the two DWC chambers are visible.

The DWC information was crucial in the off-line analysis due to the poor quality of the electron beam. The coordinates of the moving platform corresponding to the center of each crystal were found using a π^- beam, which was more collimated than the electron one. During this procedure, the gains of all PMTs were also equalized, in order to have signals of almost the same amplitude, in the same experimental conditions.

In this section I discuss the analysis that I have carried out within the Pavia DREAM group on the crystal matrix.

4.2.1 *Calibration of the crystal matrix*

The calibration procedure was performed steering 80 GeV electrons in the center of each crystal longitudinally ($\theta = 90°$). This was easily feasible since the crystal matrix was mounted on a platform which could move vertically and horizontally. For each crystal, 25000 events were recorded. In addiction, 2500 randomly triggered events provided the pedestal information.

The average time structure of both the Scintillation and Cherenkov signals are shown in Figure 4.2.3. The Cherenkov signals were integrated over 100 ns around the peak, while the scintillation signals were

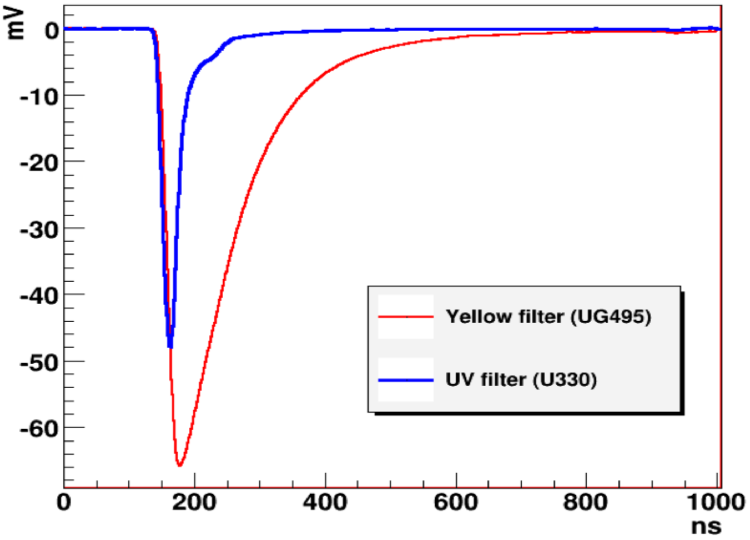

Figure 4.2.3: The average time structure for the scintillation (yellow filter) and the Cherenkov (UV filter) light, for the central crystal.

integrated over the entire time structure. The integration of the pulse shape was done event-by-event in order to get the ADC equivalent distributions (see Figure 4.2.7).

As it is shown in Figure 4.2.4, the electron beam was very broad and had a larger cross section than the trigger counters (at each electron energy). Each crystals in the matrix has a section of 3.0x3.0 cm^2, a cut on both x and y coordinates was needed in order to select events for which the particles enter the crystal in a small region located around its geometrical center. The intervals [3,13] for x (mm) and [-4,4] for y (mm) were chosen in order to select events with a significant amount of energy deposited in the central crystal. The selection criteria is based on the scatter plot representing the scintillation ADC counts of the central crystal versus x and y coordinates (see Figure 4.2.5).

In order to obtain a conversion factor between the ADC counts and the energy deposited in the matrix, two MC simulations have been carried out. It turned out that the total mean energy released by 80 GeV electrons in one crystal is 82% (65.7 GeV), while the energy released in the whole matrix is 93% (74.2 GeV). In Figure 4.2.6 the simulated matrix is shown: the seven lead-tungstate crystals have 1 mm air gap between each others (instead of mylar as in reality). The simulation has been done with the GEANT4 platform, for 80 GeV electrons and only the scintillation process was considered. The simulated beam spot has dimensions given by the cut applied to DWC coordinates. On the basis of the MC simulation results, the calibration coefficients were estimated for the scintillation signals, using the relation: $E^S_{dep} = k_S * S_{mean}$.

In order to estimate the total matrix response and its energy resolution, I have analyzed the calibration runs, i.e. the data taking when

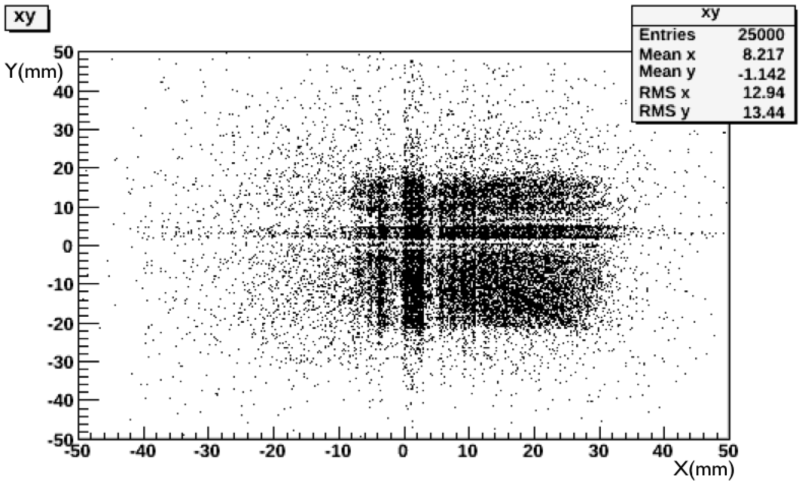

Figure 4.2.4: The beam profile for 80 GeV electrons, as obtained from the DWC.

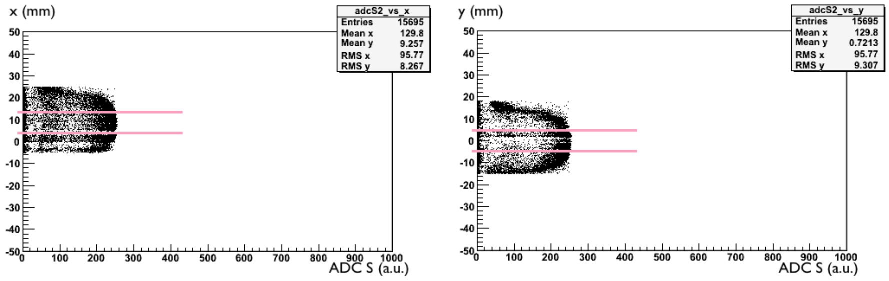

Figure 4.2.5: The scatter plot of the x and y coordinates as a function of the scintillation ADC count in crystal 2. Each events is represented by a dot (80 GeV electrons in the center of crystal 2). The solid lines represent the chosen cuts on coordinates: [3, 13] for x(mm) and [-4, 4] for y (mm).

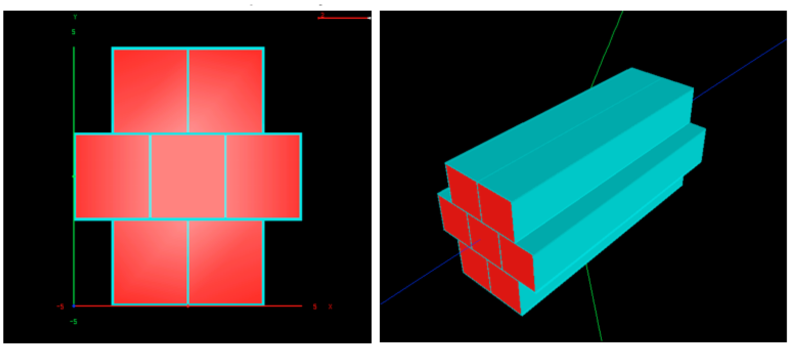

Figure 4.2.6: The front and side view of the GEANT4 simulated matrix. Each Crystal is surrounded by 1 mm air, in order to simulate the mylar wrapping.

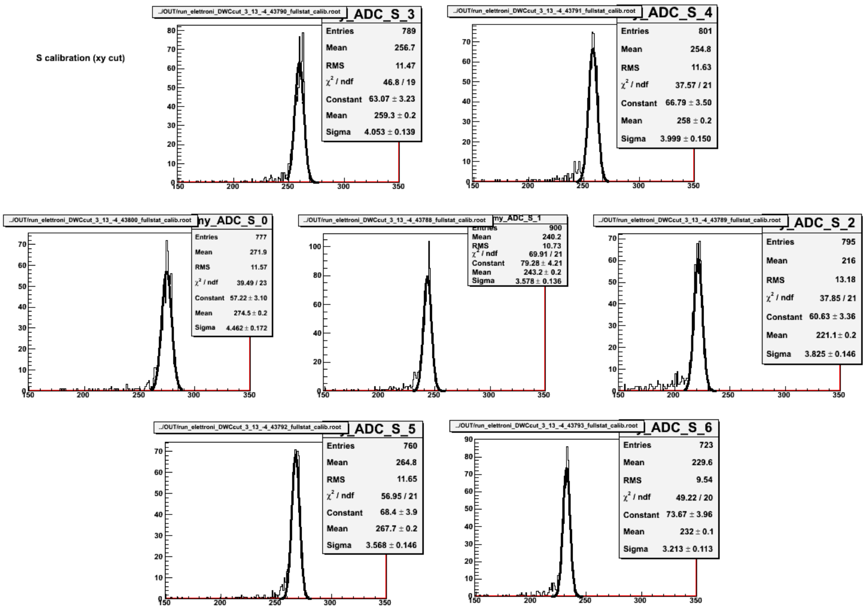

Figure 4.2.7: The equivalent ADC distribution of each crystal for the scintillation signal, fitted with a Gaussian after the cut on coordinates.

the beam was steered in the center of each crystal. The response of each crystal is fitted with a Gaussian and the equalization coefficients with respect to the crystal 2 were estimated, for both Cherenkov and scintillation signals, by comparing the mean of the distributions shown in Figure 4.2.7.

Then, I have obtained the total scintillation and Cherenkov signals by adding the signals from each crystal, for both scintillation and Cherenkov signal components. Thus, by applying the calibration coefficients to both scintillation and Cherenkov signals, I have obtained the energy deposited distribution for each beam energy (see Figure 4.2.8 and Figure 4.2.9 respectively).

4.2.2 *The energy scan with electron beam*

Once that the calibration constants have been estimated, I have analyzed data relative to the energy scan. Electrons beams of 30, 60, 80, 100 and 150 GeV were steered on the central crystal longitudinally (the matrix oriented at $\theta = 90°$). For each energy, 25000 events were recorded.

In a first phase we analyzed the central crystal alone and derived its electromagnetic resolution. We have then considered the matrix as a whole and studied its response.

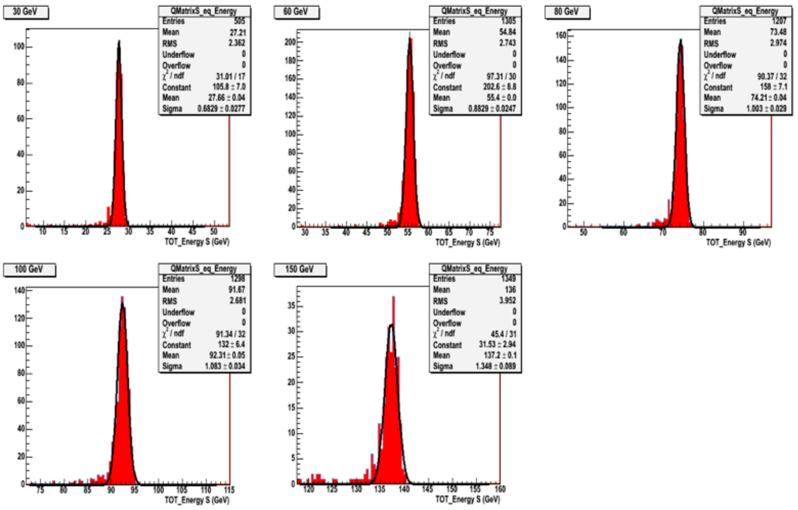

Figure 4.2.8: The energy distribution for each electron beam energy in the scan for the scintillation signals in the whole matrix, fitted with a Gaussian.

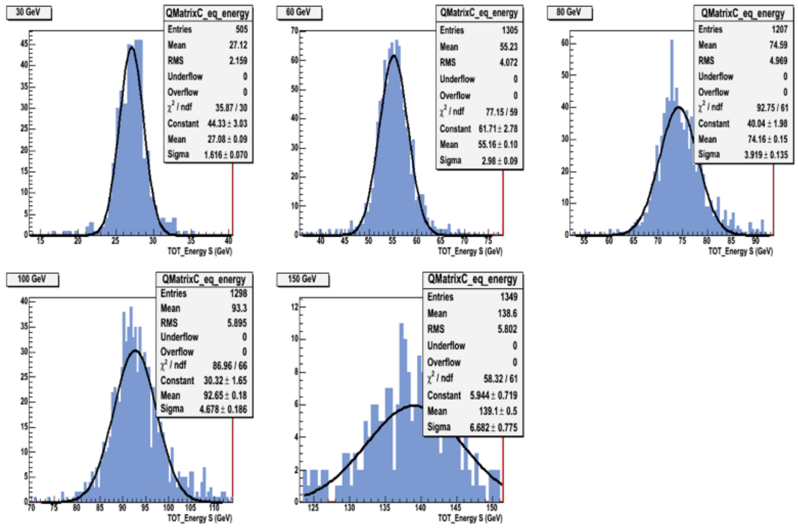

Figure 4.2.9: The energy distribution for each electron beam energy in the scan for the scintillation signals in the whole matrix, fitted with a Gaussian.

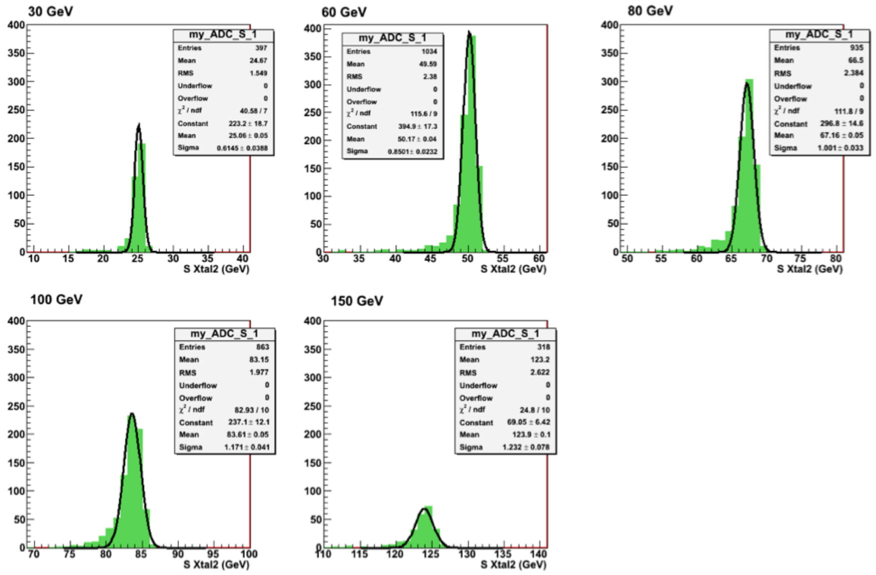

Figure 4.2.10: The equivalent ADC distributions, for each electron beam energy in the scan for the scintillation signal in crystal 2, fitted with a Gaussian (black line).

4.2.2.1 *The central crystal response*

In Figure 4.2.10 and Figure 4.2.11 the equivalent ADC distributions, after proper cuts and calibrations, of both scintillation and Cherenkov signals in crystal 2 (central), for each energy of the electron beams, are shown. The low energy events and pedestals are not displayed.

I have estimated the energy resolution σ_{rms}/E, where σ_{rms} is given by the Gaussian fit of the distributions while E is the beam energy, of the crystal 2 as a function of energy. The results are shown in Figure 4.2.12.a in the case of scintillation signals. I have fitted data with the relation $\sigma/E = p_1/\sqrt{E} + p_0$. As it is visible from the plot, the constant term is almost zero while the stochastic term is about $12\%/\sqrt{E}$. The latter is due to fluctuations in the number of photoelectrons per unit of deposited energy, to fluctuations in shower leakage and to fluctuations in longitudinal shower development (which may affect the signal because of light attenuation effects).

In the case of the Cherenkov light, the energy resolution for central crystal is $27\%/\sqrt{E}$, with the constant term is about zero (see Figure 4.2.12.b). The resolution is expressed in a.u./GeV because the calibration coefficient was not determined in the case of the Cherenkov signal. The stochastic term is greater than the one for scintillation signal, as it is expected by looking at the ADC distributions (Figure 4.2.11) which are broader. In this case, fluctuations relative to the light yield are greater and contributes more to the Cherenkov energy resolution. The stochastic term is also due to the shower leakage and to absorption effects. Therefore, it is not possible to estimate the Cherenkov light yield from this term. However, the event-by-event

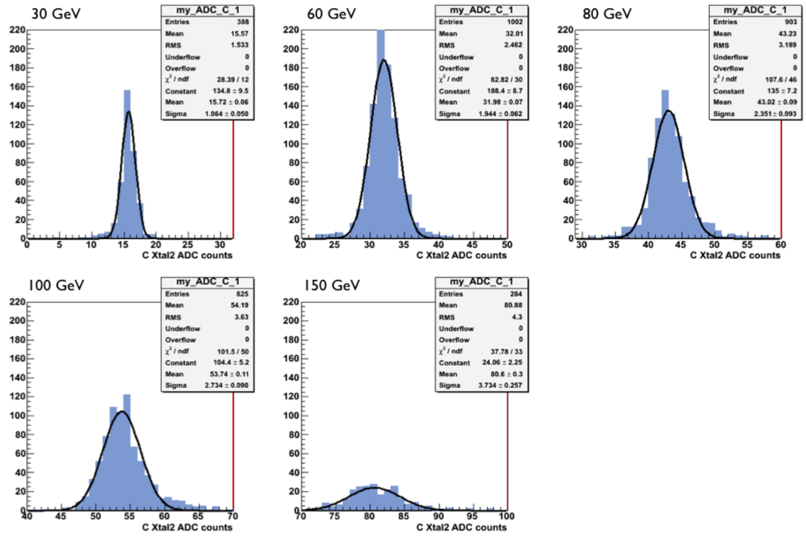

Figure 4.2.11: The equivalent ADC distributions, for each electron beam energy in the scan for the Cherenkov signal in crystal 2, fitted with a Gaussian (black line).

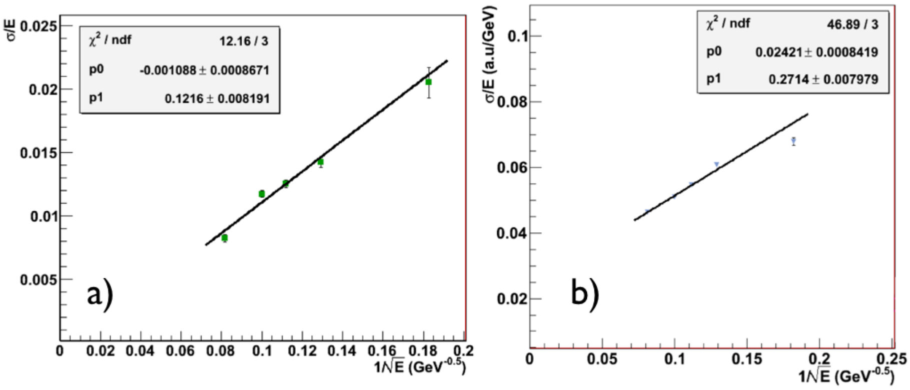

Figure 4.2.12: The energy resolution for scintillation light (a) and Cherenkov light (b) of the central crystal of the matrix, as a function of $E^{-1/2}$. See text for details.

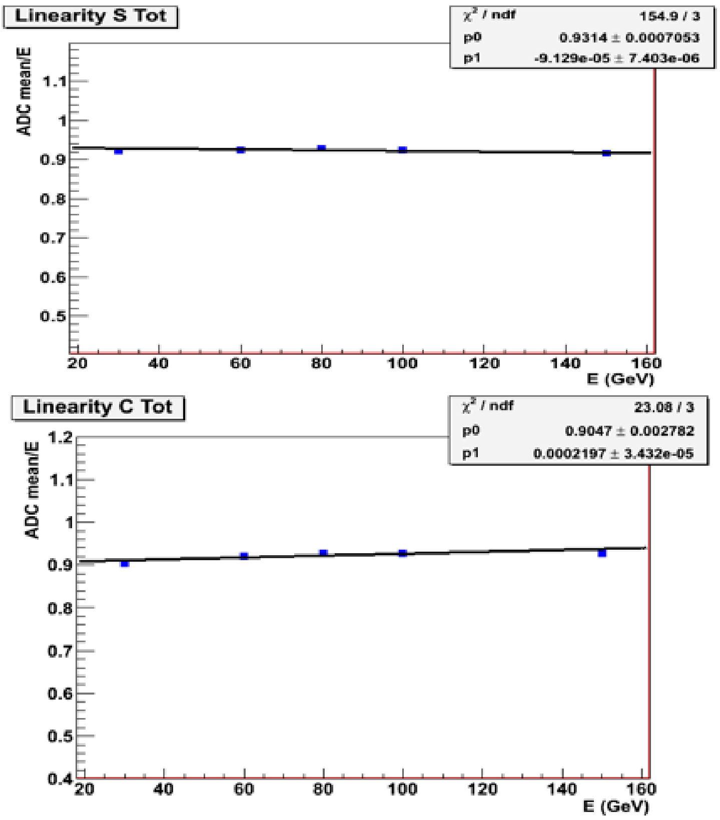

Figure 4.2.13: The crystal matrix response linearity for the scintillation (top) and the Cherenkov (bottom) light, as a function of the energy.

distribution of the Cherenkov/scintillation signal ratio provides more information in this respect, since it is less sensitive to the fluctuations that are unrelated to the light yield, such as the shower leakage fluctuations [21]. By fitting the C/S distribution with a Gaussian, turns out that the relative width of the distribution is $\sigma/mean \simeq 6\%$. Since the width of the distribution is inversely proportional to the Cherenkov light yield, the latter is at least 50 p.e. per GeV.

4.2.2.2 *The crystal matrix response*

In order to assess the crystal matrix response I added the signals from each crystal, for both scintillation and Cherenkov signal components.

In Figure 4.2.13 the response linearity of the crystal matrix for scintillation and Cherenkov light is shown, fitted with the linear relation $f(E) = p_1 E + p_0$. The constant term in both the plots is less than 1, since the matrix does not fully contain the electromagnetic showers (containment at 93% level, from MC simulation). In the case of the scintillation light p_1 is close to zero and has a negative value since the PMT which detects the scintillation signals is located upstream the crystal: as the beam energy increases, the shower develops further with

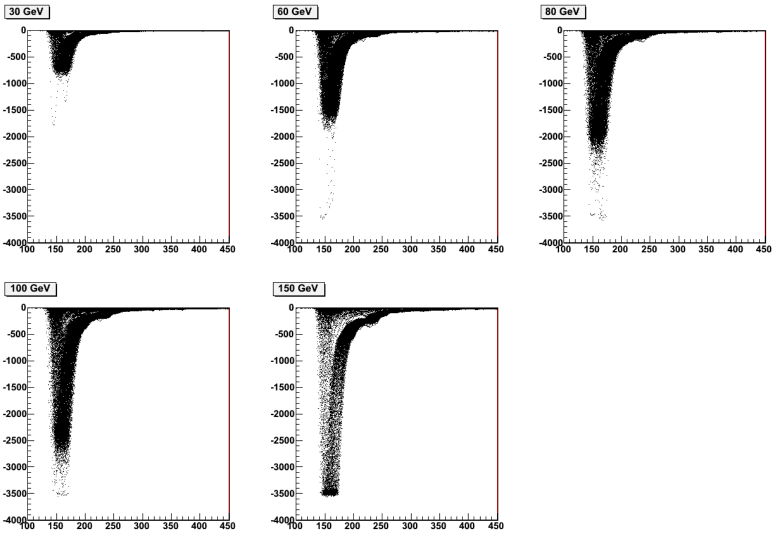

Figure 4.2.14: The pulse shapes of Cherenkov signals event-by-event, for each electron energy of the scan.

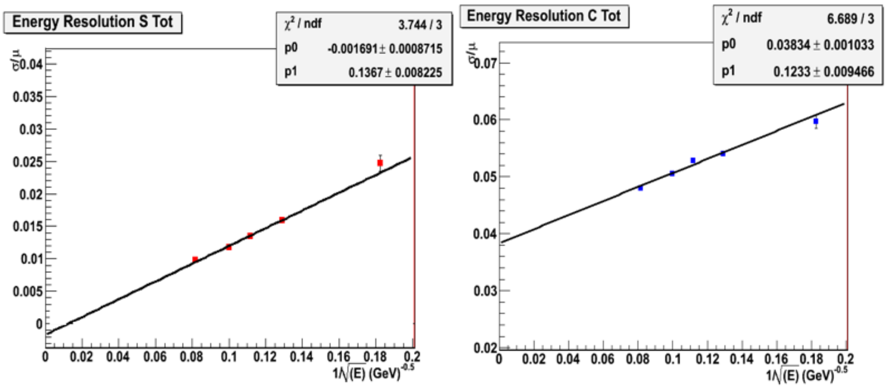

Figure 4.2.15: The energy resolution of the crystal matrix for the Cherenkov and the scintillation signals, as a function of $E^{-1/2}$.

respect to the upstream PMT and absorption effects come into play. Besides these effects, at 150 GeV saturations effects due to the high voltage of the PMTs become relevant and contribute to the p_1 negative value. For the Cherenkov light the constant term is close to zero too, and it is positive since the PMT which detects the Cherenkov light is located downstream: as the energy increases, the shower develops deeper and may releases energy directly in the photomultiplier. In Figure 4.2.14 it is clearly visible the saturation of the Cherenkov signals, when 150 GeV electrons hit the crystal.

For this analysis, we have decided to use the scintillation calibration constant also for the Cherenkov signals.

The crystal matrix energy resolution for scintillation and Cherenkov light turns out to be $\sigma/E = 13.7\%/\sqrt{E}$ and $\sigma/E = 12\%/\sqrt{E} + 3.8\%$ respectively, as it is shown in Figure 4.2.15. The constant term in the

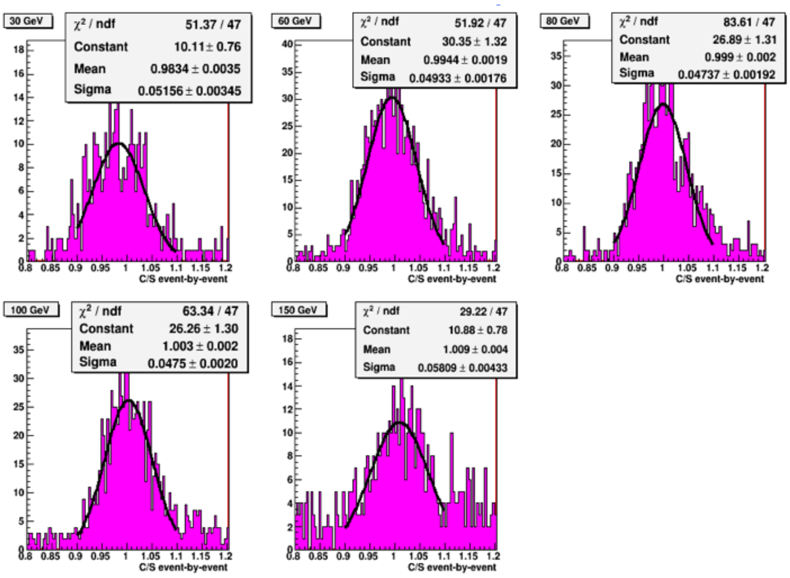

Figure 4.2.16: The total C/S distribution for all electrons beam energy in the scan, for the crystal matrix. The distribution are fitted with a Gaussian.

Cherenkov light resolution is due to saturation effects, as discussed before. The stochastic term for the scintillation light is worse with the respect to the single crystal one probably due to some miscalibration effect which is under investigation.

Since the estimation of the electromagnetic fraction is made by the knowledge of the C/S ratio event-by-event, I have estimated the C/S width, i.e. the σ_{rms} of the C/S distribution, and the C/S response linearity of the crystal matrix, for different electron beam energy. The C/S distributions event-by-event for each electron energy in the scan is shown in Figure 4.2.16 while the C/S response linearity and the C/S width are reported in Figure 4.2.17. The response linearity results very stable as the energy increases, and the C/S σ_{rms} turns out to be 4.6%.

Further improvements to these results may be done, for example, by determining more precise equalization coefficients minimizing the width of the sum of the towers. The equalization issue could be investigated also by a Monte Carlo simulation. In this context I have made a GEANT4 simulation of the scintillation and the Cherenkov processes in a lead-tungstate crystal. The optical processes simulation is not trivial and I have to investigate still many aspects, such as the simulation of cookies, optical filters, and mylar wrapping. However, I have obtained angular scan results qualitatively in agreement with physical predictions and I would like to simulate the entire crystal matrix, after that most of the problems with the optical processes will be solved. In this way, it would be possible to estimate correctly the equalization coefficients.

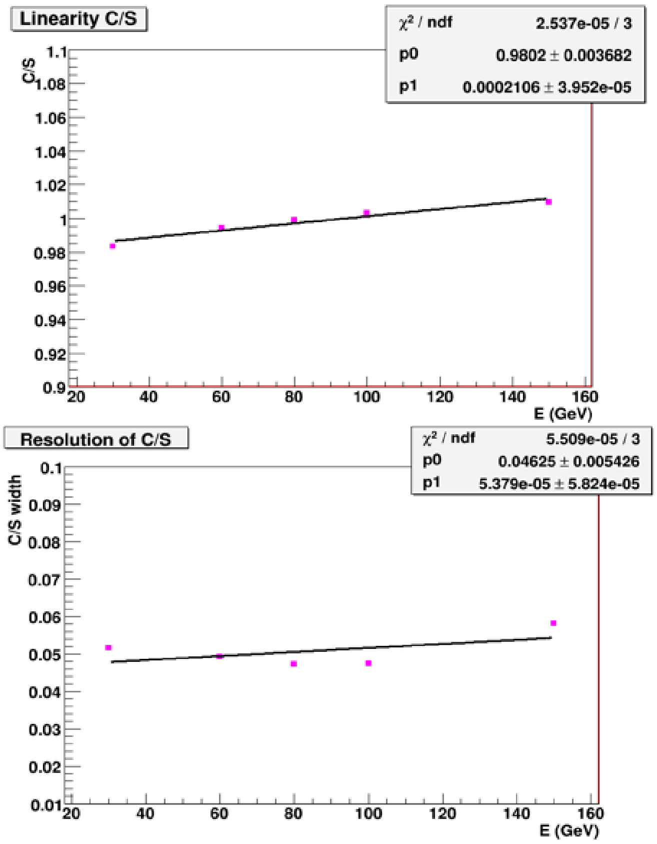

Figure 4.2.17: The linearity response of the C/S ratio, for the crystal matrix, as a function of energy (top). The energy resolution of the C/S ratio, for the crystal matrix, as a function of $E^{-1/2}$.

4.2.3 *The pion signals*

Electrons are fundamental for the calorimeter calibration. Once it is done, we started a test program based on pion beams. As for electrons, we studied the response of both the central crystal and of the whole matrix. For the pion beam we mainly concentrated on the use of the C/S signal to study combined performances with the DREAM fiber module.

In Figure 4.2.18 the pion beam profile as obtained from the DWC and the applied cuts are shown. Also in this case, I have chosen the cuts on the coordinates as described in Section 4.2.1. The scintillation signal distribution of the central crystal is shown in Figure 4.2.19. It is obtained by integrating the average signal shape over the entire time structure as discussed before. The distribution is very different from the electrons one, since a large fraction of pions traverses the crystal without starting a shower. These events populate the large mip peak. The interaction length of lead-tungstate crystal is 18 cm. This value concerns protons, and the value for pions is typically 50% larger. Therefore an interaction length of 27 cm for pions would imply that

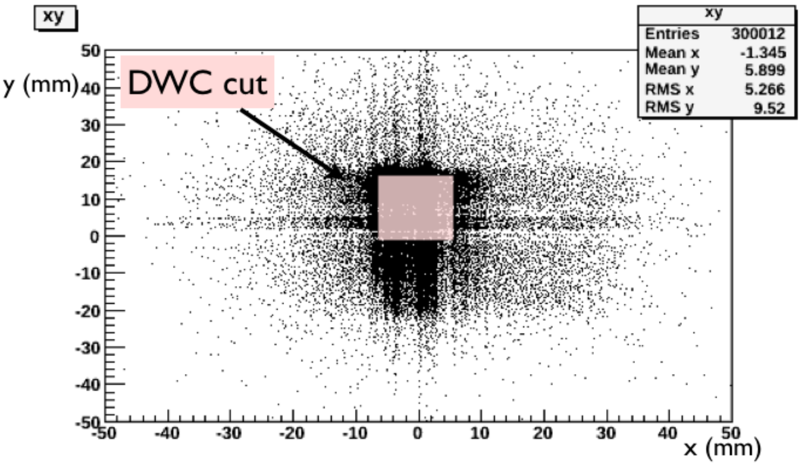

Figure 4.2.18: The 180 GeV pion beam profile. Events in the intervals [-5, 5] for x, and [-1, 15] for y (mm) are selected for the analysis.

about 48% of these particles traverse the 20 cm long crystal without undergoing a nuclear interaction. This is close to the observed fraction of events in the mip peak (the event sample consists of 300000 events in total).

As shown in Figure 4.2.19, I have selected for the analysis only pions which interact in the crystal and deposit a significant amount of energy in it. Concerning the Cherenkov signals, only the pedestal events were cut (see Figure 4.2.20).

The scintillation and Cherenkov signals of DREAM (fiber module) central tower are shown in Figure 4.2.21. They have been obtained after the event selection discussed above.

As discussed in Section 3.2.4, if the C/S ratio is known event-by-event, the hadronic energy resolution can be improved, and the calorimeter response becomes Gaussian. In the case of an hybrid calorimeter, this is true if the C/S ratio of the two sections are correlated. In order to show the merits of the dual readout methods and the mentioned correlation, I have applied the knowledge of the C/S ratio of the crystal matrix to the scintillation signals in DREAM, as described below.

The distribution of the Cherenkov/scintillation signal ratio for the selected pions events, in the central crystal, is shown in Figure 4.2.22. I have selected two regions, one with the C/S ratio ranging from 0.3 to 0.4 and the second for C/S greater than 0.8. For the selected subsamples, I have obtained the plot of the distribution of the scintillation signal measured in the central tower of DREAM (see Figure 4.2.23). The two distributions are narrower and more symmetric than the scintillation ADC distribution shown in Figure 4.2.21 (bottom plot). Indeed, since the C/S ratio is related to the f_{em}, as C/S value increases, the average value of the subsample distribution increases. Therefore

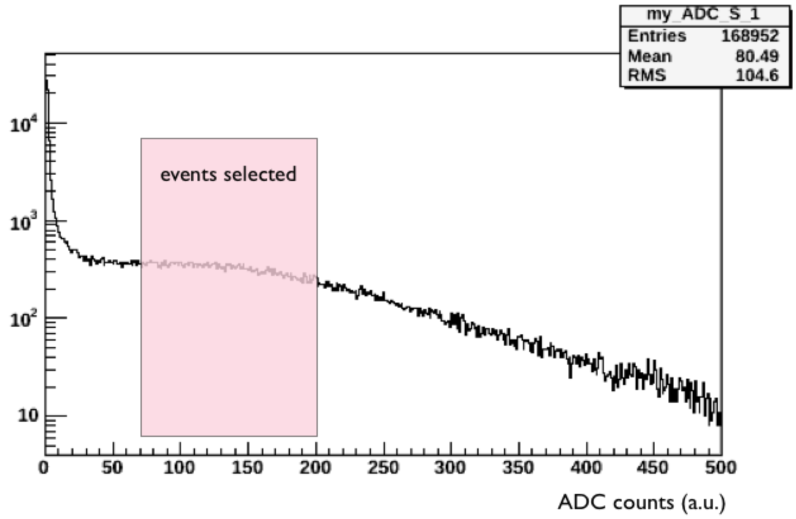

Figure 4.2.19: The equivalent ADC scintillation distribution for the central crystal. Only pions which have started a shower in the lead-tungstate crystal and have deposited a significant amount of energy are selected (highlighted region).

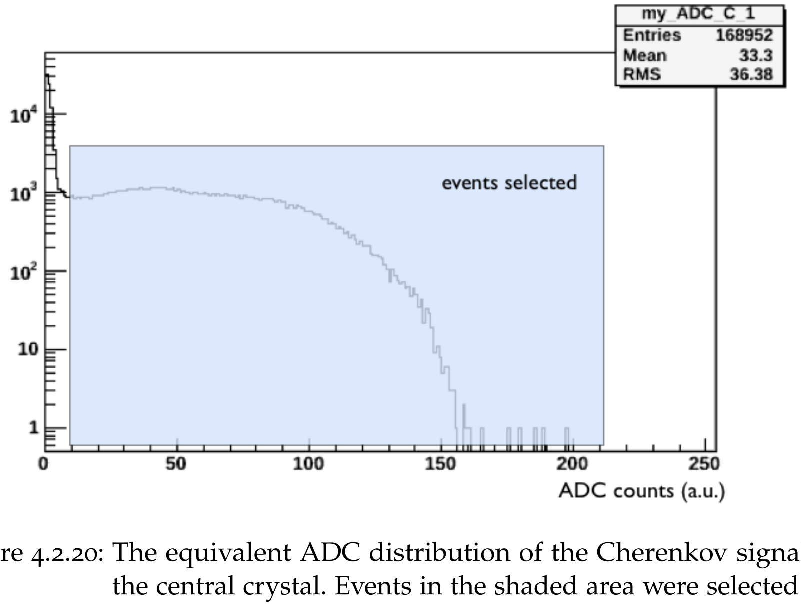

Figure 4.2.20: The equivalent ADC distribution of the Cherenkov signal in the central crystal. Events in the shaded area were selected for the analysis.

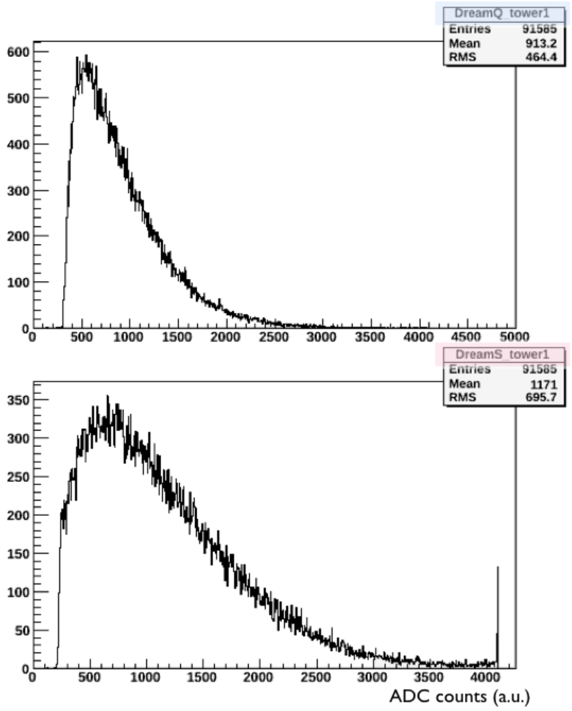

Figure 4.2.21: The ADC distributions of the Cherenkov (top) and the scintillation signal (bottom) of the central DREAM tower, after cut on events, based on the crystal Cherenkov and scintillation signals.

the event selection on the basis of the C/S ratio in the crystal is a good measure of f_{em}.

If we consider signals in the whole lead-tungstate matrix, the distribution of the Cherenkov/scintillation signal ratio for the selected pions events is shown in Figure 4.2.24. The distribution peaks at 1 since we have chosen the same calibration constants for the two types of signals. As before, I have selected two regions, one with the C/S ratio ranging from 1 and 1.6 and the second with C/S greater than 3.5. Hence, I have done the plot of the distribution of the total scintillation signal measured in DREAM for the mentioned subsets of events (see Figure 4.2.25).

The signal distribution for the events with a large C/S value is narrower and peaks at a larger value than the distribution for the events with a smaller C/S signal ratio. This is reasonable since the fractional width of the signal distributions observed in DREAM decreases as the events become more "electromagnetic". Comparing each distribution with the total energy distribution of the scintillation in DREAM (Figure 4.2.26), we note that the distribution of the sample with C/S>3.5 is narrower and thus the hadronic resolution improves if the knowledge of the C/S ratio is exploited. These results are worse than the ones obtained with only the DREAM central tower, and this can find an explanation in the difficulties encountered in the DREAM calibration.

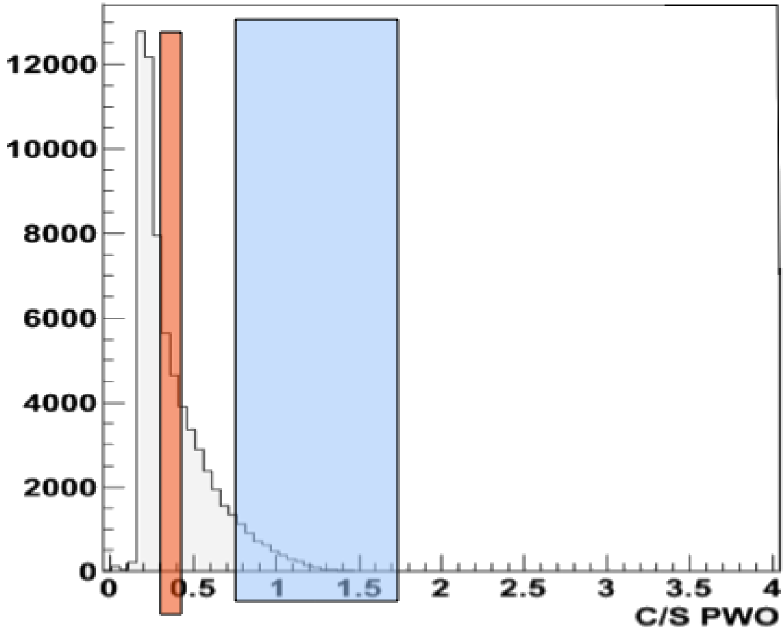

Figure 4.2.22: Distribution of the Cherenkov/scintillation signal ratio (not calibrated) for 180 GeV π^- that start a shower in the central crystal of the matrix (crystal 2). Two event samples (highlighted area), which have covered different C/S values, are taken for further analysis. See text for details.

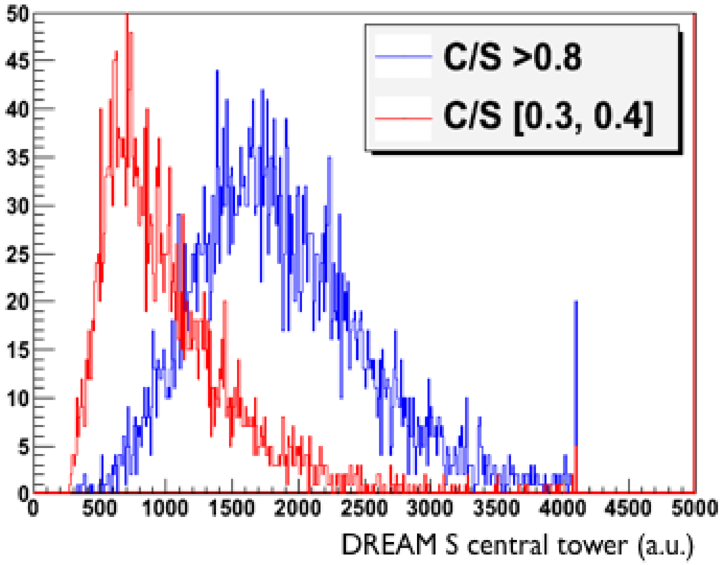

Figure 4.2.23: The equivalent ADC distribution for the scintillation signal of the DREAM central tower, for two subsets of events selected on the basis of the C/S ratio in the central crystal of the lead-tungstate matrix.

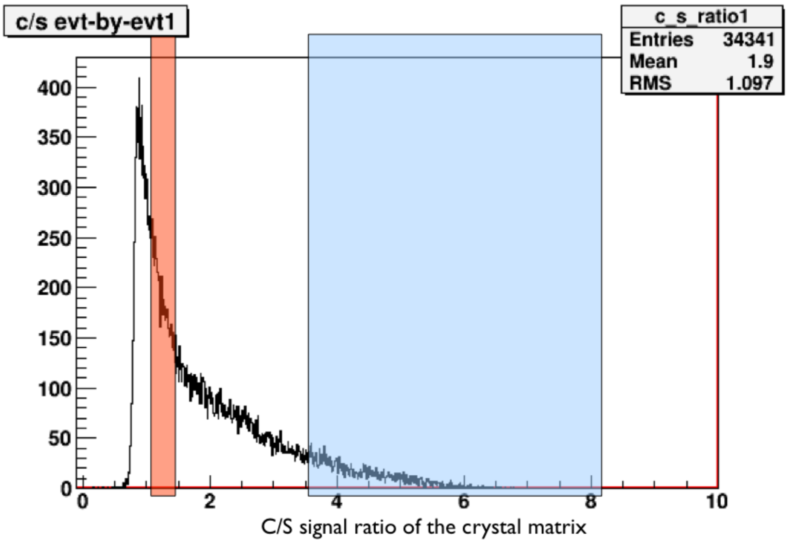

Figure 4.2.24: Distribution of the total Cherenkov/scintillation signal ratio (calibrated) for 180 GeV π^- that start a shower in the central core of the matrix. Two event samples (highlighted area), which cover different C/S values, are taken for further analysis. See text for details.

Since the poor quality of the beam, many events contribute to pedestal distributions, which are not easy to fit and subtract from the raw data.

However, this preliminary analysis demonstrates that it is possible to apply the dual-readout technique to an hybrid detector. Due to the poor beam conditions and the small dimensions of the crystal matrix, it was not possible to assess quantitatively the improvements in hadronic energy resolution and calorimeter response function. Indeed the cuts on coordinates strongly reduce the statistics and the calibration procedure is difficult because the beam spot was very large and the electromagnetic showers used to calibrate crystal signals were not fully contained in them.

The lead-tungstate matrix has been tested as the em section of a combined calorimeter also in July 2011, with higher statistics. The quality of the electron beam was improved and, by exploiting a second DWC, a pre shower detector and a veto counter, which triggers the DAQ system only for events passing through a circle of 2 cm diameter, more information is available on the beam. Moreover both sides of the crystal matrix have been equipped with UV filters, in order to apply the single-side analysis and to compare the two signals. This allows to correct and thus eliminate off-line the Cherenkov absorption effects. The analysis of these data will be done in autumn 2011, and more promising results could come out.

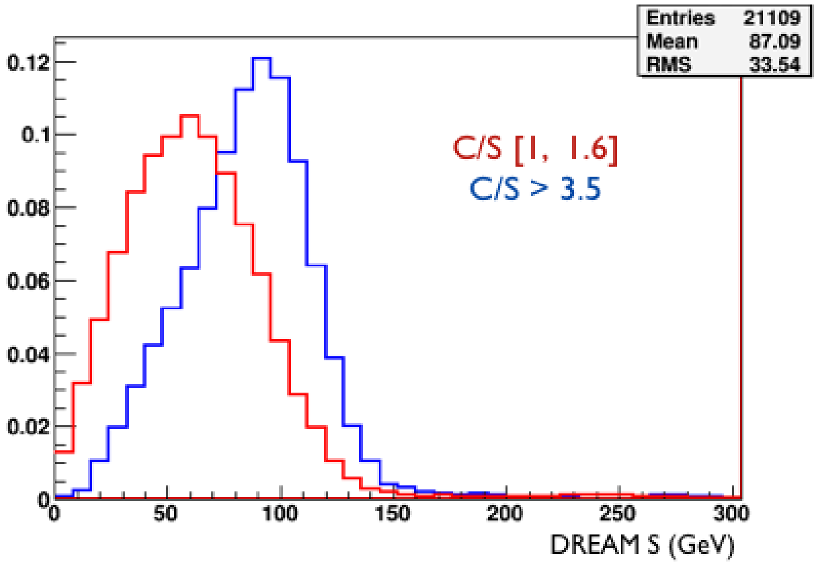

Figure 4.2.25: The DREAM scintillation signal distribution for subsets of events selected on the basis of the total C/S ratio of the crystal matrix.

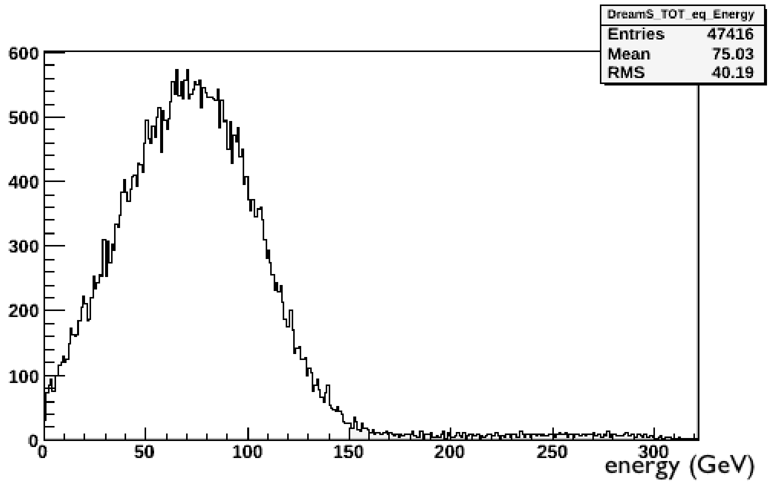

Figure 4.2.26: The total energy deposited (scintillation signal) in the DREAM detector.

4.3 THE ANALYSIS OF POLARIZATION MEASUREMENTS ON A BSO CRYSTAL

In the previous sections we have seen that lead-tungstate crystals are characterized by a high Cherenkov light yield but they are affected by strong self-absorption in the UV range, which may be a problem in calorimeters where showers starting point fluctuates over distance of 20 cm. The DREAM Collaboration has also studied other types of crystals, in order to find the most suitable crystal for application in dual-readout calorimetry.

Studies with BGO crystals have shown that the Cherenkov radiation represents only a small fraction, i.e. 1%, of the light output. However, it is possible to separate the two types of light by means of optical filters in a quite efficient way [22] since the long tail of the scintillation signal.

Given these results, a systematic study of the properties of BSO was carried out [24], since this crystal has the same structure of BGO but the optical characteristics are even more suitable for dual-readout technique. It turned out from tests that BSO had a two or three times larger light yield, and the purity of the Cherenkov signals obtained with an UV filter was better than in BGO. Light attenuation resulted to be approximately the same in both crystals, and smaller than in lead-tungstate ones. Besides, also with BSO crystal it is possible to carry out a single-side analysis (see Section 3.2.3), since the scintillation has a long decay constant. For these reasons, BSO crystals may be good candidates in a combined dual-readout calorimeter.

Apart from directionality, time structure and spectral properties of the signals, there is another feature that can be used to separate the scintillation and the Cherenkov light in homogeneous media, namely the fact that the latter is polarized. The Cherenkov light is emitted by a medium that is traversed by relativistic charged particles. The medium atoms are excited and polarized in this process. They emit coherent radiation at a characteristic angle θ_C with respect to the particle track. The polarization vector of this radiation is oriented perpendicular to the direction in which the photons travel, i.e. perpendicular to a cone whose central axis is the particle track, as shown in Figure 4.3.1.

In the case of relativistic particles which traverse the BSO crystal at $\theta = 30°$ (see Figure 4.1.1), the Cherenkov light emitted in the horizontal plane travels approximately perpendicular to the end face of the crystal, where the PMT is located, since in BSO $\theta_C \approx 60°$. Light traveling at an angle ϑ with this plane may also be detected by the PMT. The critical angle, i.e. the angle at which total internal reflection occurs, is about 43°. However, since photons have to traverse three cookies and 2 filters, the optical one and the polarizer, the critical angle is smaller, $\sim 30°$. When $\vartheta \neq 0$ the polarization vector has also a component in the vertical plane (P_y). But, even when ϑ is close to

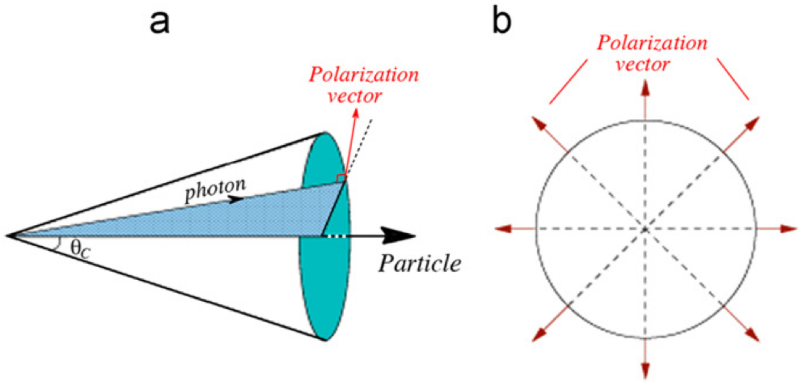

Figure 4.3.1: Polarization of Cherenkov light emitted when a charged particle traverses a medium with refractive index n at a speed greater than c/n. The light is emitted in a cone with angle $\theta_C = arccos(\beta n)^{-1}$ (a) and is polarized with the polarization vector oriented perpendicular to this cone (b).

the critical angle, the vertical component is less than a half as large as the horizontal one (P_x) [25]. Therefore a polarization filter will be favorable if the transmission axis is in the horizontal plane.

In 2011 the DREAM Collaboration decided to investigate this characteristic for Cherenkov/scintillation separation.

4.3.1 *Study of the Cherenkov light polarization*

For this study we used a BSO crystal, with a length of 18 cm and a cross section of 2.0x2.0 cm^2. The traverse dimension corresponds to 1.74 X_0. The experimental setup is shown in Figure 4.3.2.

An UV filter (U330) is used in the Cherenkov readout side while a yellow filter (GG495) is used in the scintillation readout side. In addition to the optical filters, both sides of the crystal were equipped with polarization filters, which were cut in order to cover the entire crystal end faces. Thin elastocil cookies provided the optical coupling between the crystal, the optical filter, the polarizer and the PMT, to each other.

A series of angular scan were carried out in order to study the Cherenkov light polarization as a function of the angle θ. When the angle θ is negative the side equipped with the UV is downstream and it is therefore optimal for the Cherenkov detection.

The measurements were performed with 180 GeV π^- beam, which contained about 30% of muons. The angle θ between the crystal axis and the plane perpendicular to the beam line (Figure 4.1.1) ranged from -67.5° to +50°. At each angle 40000-50000 events were collected. In addiction, 4000-5000 randomly triggered events provided the pedestal information. The angular scan was performed for three different setup, as summarized in Table 4.3.1. The polarization filter is said to be

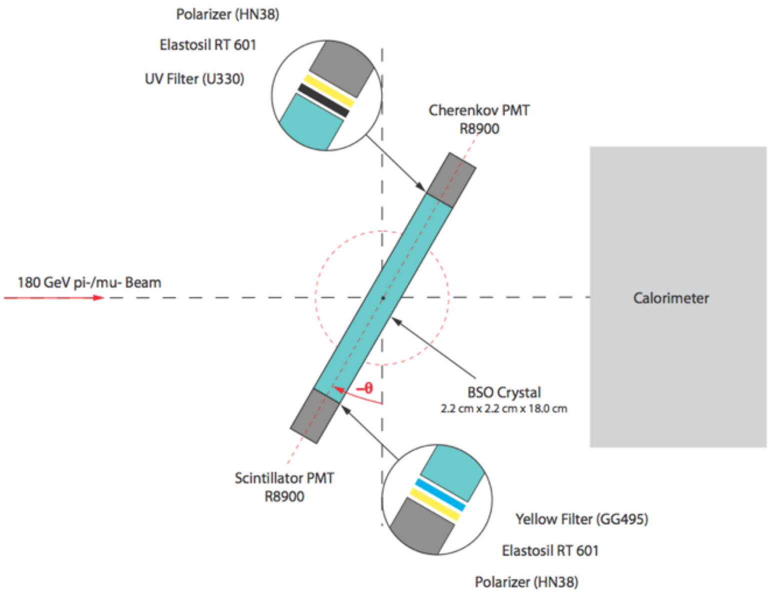

Figure 4.3.2: The experimental setup for the angular scan measurements. See text for details.

	S (GG495 side)	C (U330 side)
SETUP 0	no polarizer	no polarizer
SETUP 1	polarizer favorable	polarizer favorable
SETUP 2	polarizer unfavorable	polarizer unfavorable

Table 4.3.1: The three different setup for the angular scan. See text for details.

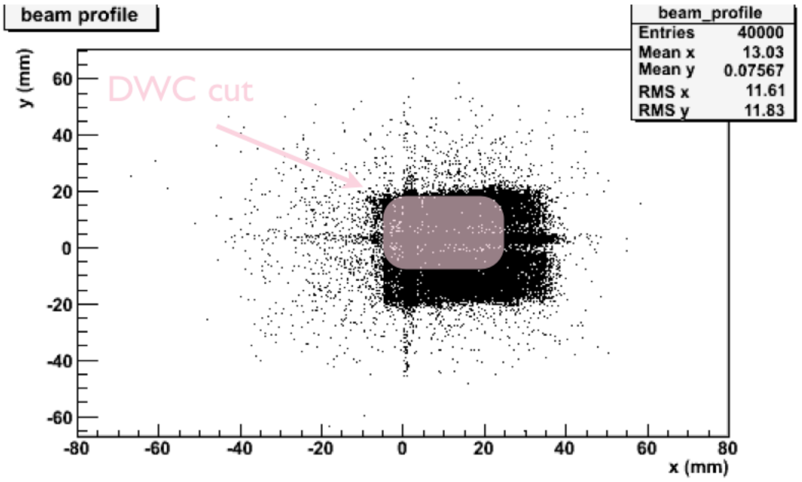

Figure 4.3.3: The beam profile, obtained from the DWC (Delay Wire Chamber) information. The pink region represents the events selected for the analysis. See text for details.

favorable when the transmission axis is parallel to the polarization direction of the Cherenkov photons, i.e. in the horizontal plane. The polarization filter is said to be *unfavorable* when the transmission axis is perpendicular to the polarization direction of the Cherenkov photons, i.e. in the vertical plane.

In the off-line analysis, I have exploited the beam chamber (DWC) information to select events which enter the crystal in a small region located around its geometrical center. In Figure 4.3.3 the beam profile obtained from the DWC data is shown, as well as the selected coordinates [-5,25] in x and [9,18] in y (mm).

The Cherenkov and the scintillation signals were acquired event-by-event by means of a digital oscilloscope. As in the previous analysis, the average time structure of Cherenkov signals was integrated for each event over a small time interval ($\sim$ 80 ns) while the scintillation average time structure was integrated over the entire pulse shape.

Once the baseline subtraction is performed by exploiting the pedestal information, I have removed saturated events and "zeros". Saturated events were due to signals which deposited a great amount of energy in the crystal, generating a signal which exceeds the range of the readout system, while zeros were events which deposited very little amount of energy in it, mainly not interacting pions.

In Figure 4.3.4 the angular dependence of the polarization effects are shown. In these plots the C and S values are the mean values of the respective ADC equivalent distributions, estimated by fitting the distributions with a Landau. The error bars are very small thanks to the high statistics. An example of the ADC equivalent distribution and of its Landau fit is shown in Figure 4.3.5. The Cherenkov signals are considerably larger for $\theta < 0°$ than for $\theta > 0°$, since the maximum detection efficiency for the Cherenkov light is for $\theta \sim 90°\text{-}\theta_c$. This

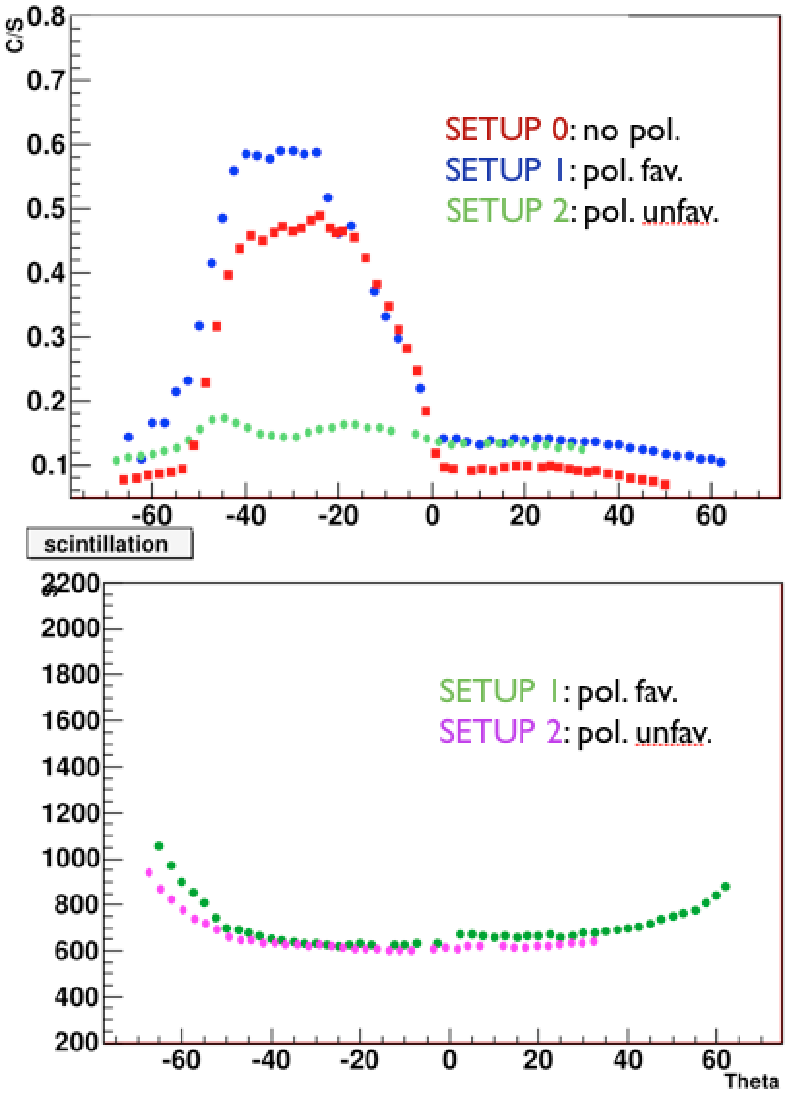

Figure 4.3.4: The C/S (top) and the scintillation light (bottom) as a function of the angle θ, for the three different setup. In the case of setup 2 the angular scan has been done only between -67.5° and 35°.

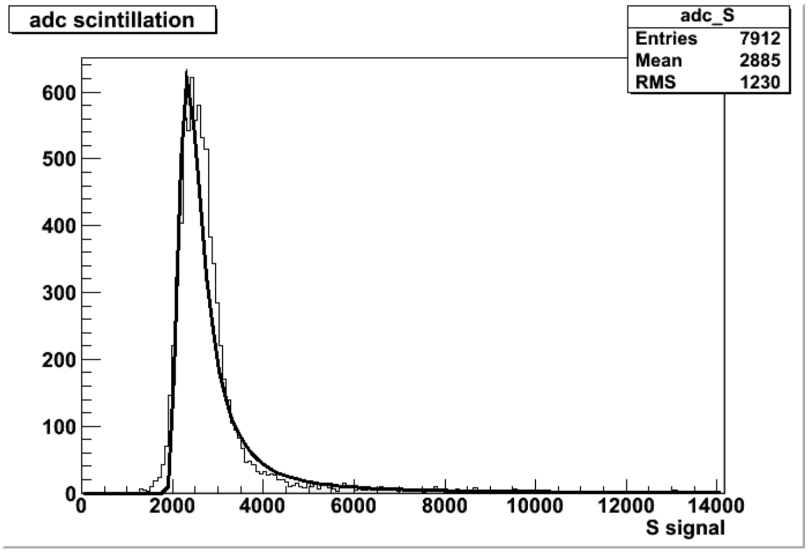

Figure 4.3.5: The ADC distribution of scintillation light (180 GeV negative pions), fitted with a Landau.

effect is more pronounced for measurements in the setup 1, when the polarization filter is favorable. Indeed by means of polarization filter the separation power of the C/S signals increases of about 30%. On the other hand, the Cherenkov light is strongly reduced when the polarizer is unfavorable, which confirms the assumption made before on the Cherenkov polarization vector are correct. In Figure 4.3.4 it is also visible a small bump at the "anti-Cherenkov angle". This bump is due to the Cherenkov light which makes a roundtrip in the crystal and is detected from the Cherenkov PMT. The origin has been established from the fact that this signal was delayed by a few ns with respect to the signal observed at the Cherenkov angle.

The orientation of the polarization filter has no effect on the scintillation signals, as it is clearly visible in Figure 4.3.4 (bottom). The increasing of the scintillation light at large angles is due to its $cos^{-1}\theta$ dependence on the path length of the beam particles through the crystal.

Since the pion beam was not pure, as said, due to muon contamination, I have discriminated muon and pion event samples, by using the DREAM information. In the case of pions, a large amount of energy is deposited in the DREAM detector while muons behave as mips, and so they are represented by a mip peak at low energy in the total ADC distribution of the scintillation signal in DREAM, as it is visible in Figure 4.3.6.

In Figure 4.3.7 the scintillation light S, the Cherenkov light C and the C/S ratio for pions and muons, in the setup 1 configuration, are shown.

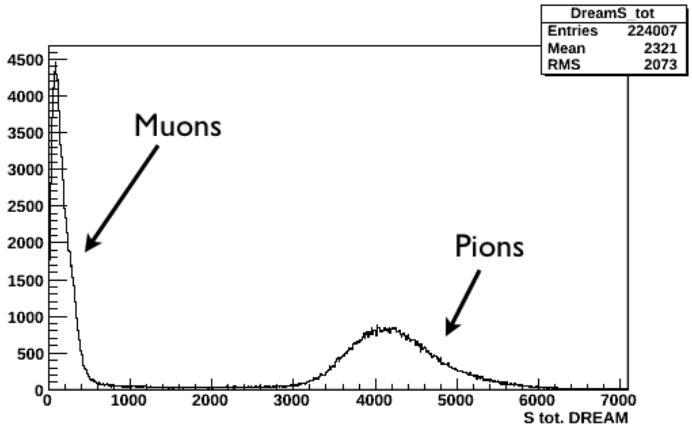

Figure 4.3.6: The DREAM scintillation total distribution for a 180 pions beam, contaminated with muons. The two different energy deposition distribution are clearly visible.

4.3.2 *Study of the longitudinal polarization profile of em showers*

Besides the study of the Cherenkov light polarization as a function of angle, it may be interesting to investigate the longitudinal polarization profile of an electromagnetic shower.

As discussed in Section 2.3.2, the longitudinal development of a shower scales approximately with the radiation length X_0 of the material. The mean longitudinal profile of the energy deposition in an electromagnetic cascade is reasonably well described by a gamma distribution [35]:

$$\frac{dE}{dt} = E_0 b \frac{(bt)^{a-1} e^{-bt}}{\Gamma(a)} \tag{4.4}$$

where E_0 is the initial energy of the shower and t is the shower depth in units of radiation length. The b parameter depends upon both the Z-value of the material and the incident energy, while a describes the shape of the shower. The shower maximum t_{max} occurs at depth $(a-1)/b$.

Since the scintillation light produced in the crystal is a measure of the energy deposited in it, the em shower profile can be measured by placing lead plates of increasing thickness (from 0.5 cm to 12 cm) in front of the crystal, as shown in Figure 4.3.8.

Measurements were performed with 80 GeV electron beam, hitting the center of a 20 cm long BSO crystal, with a cross section of 2.0x2.0 cm^2. 10000-20000 events were recorded for each Pb thickness, and 1000-2000 randomly triggered events provided the pedestal information. At both sides of the crystals polarization filters are placed, as described in the previous section. Measurements were performed with the crystal oriented at the Cherenkov angle, i.e. 30°, as well as the lead plates. Because of the poor beam condition, only 4000-8000 events were

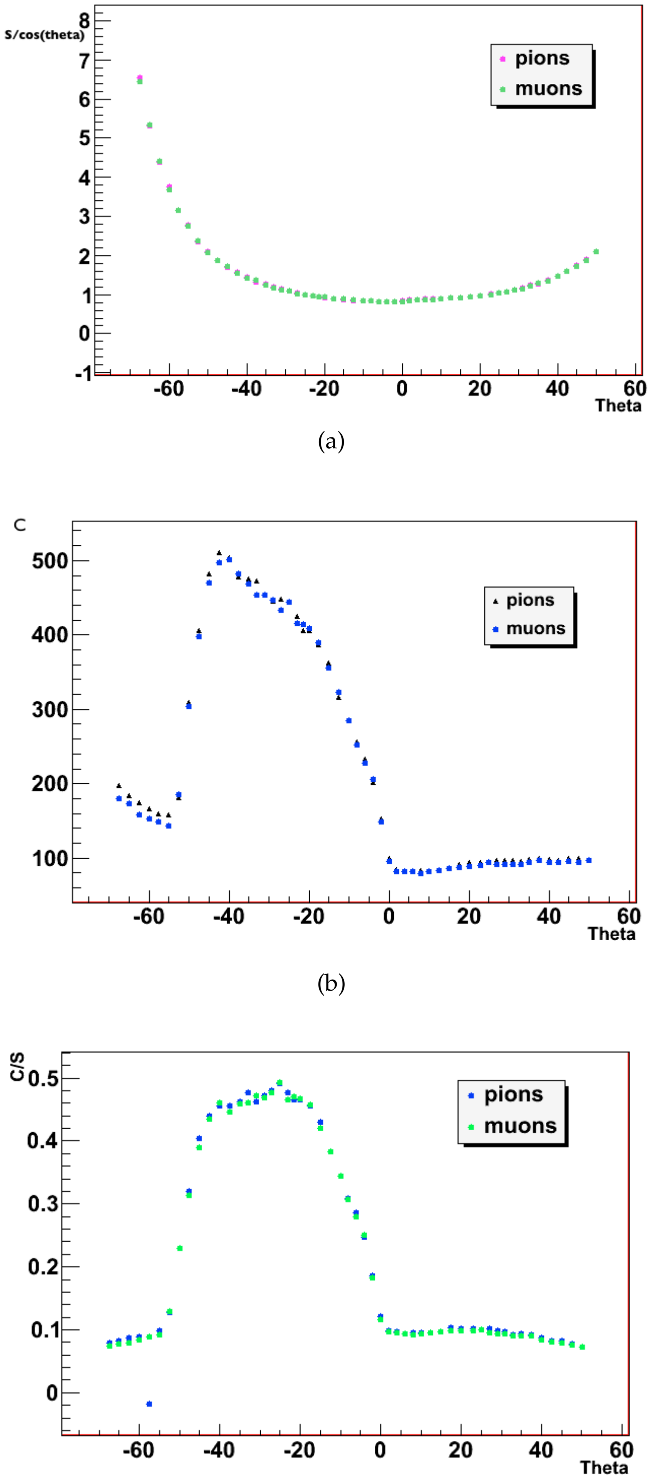

(a)

(b)

(c)

Figure 4.3.7: The scintillation light (a), the Cherenkov light (b) and the C/S ratio (c) as a function of θ for pions and muons (setup 1). In the plot (a) the scintillation signals are divided by a factor $cos(\theta)$ in order to eliminate the path length dependence.

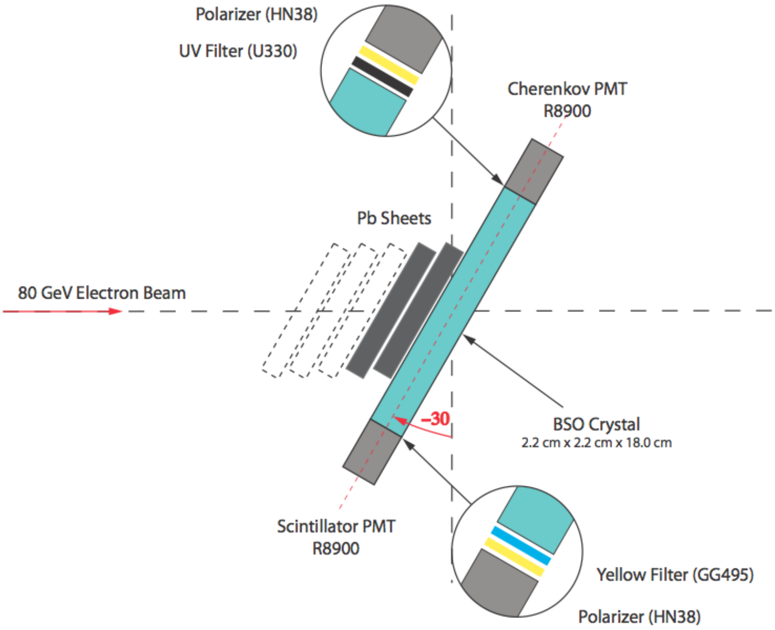

Figure 4.3.8: The experimental setup for longitudinal shower profile measurement.

used for the analysis, after the cut on coordinates based on DWC information.

In Figure 4.3.9 the results for the setup 1 (polarizer favorable) are shown. The error bars are given by $\sigma_{rms}/\sqrt{N}$, where σ_{rms} is the root mean square of the equivalent ADC distributions of the Cherenkov and the scintillation signals fitted with a Landau, while N is the number of events. An example of such a fit is shown in Figure 4.3.5. In order to show the radiation length dependence of the shower profile, the thickness of the BSO crystal and of the lead plates are converted to radiation lengths (BSO: $X_0 = 1.15\,cm$ lead: $X_0 = 0.56\,cm$). I have divided each scintillation signal by a factor 0.86 ($cos\,30°$), in order to eliminate the path length dependence.

The obtained electromagnetic shower profiles shown in Figure 4.3.9 are fitted with Equation 4.4. The profile obtained with the scintillation data, i.e. the energy deposited, is quite well represented by the gamma distribution. On the other hand, in the case of the Cherenkov light, the curve behavior shows some discrepancies. Indeed in the first stages Cherenkov signals rise faster since they are proportional to the number of relativistic particles, while the scintillation light rises more slowly since the shower has not developed yet. On the other hand, in the late stages the Cherenkov signals decrease quickly since more and more particles fall below the Cherenkov production threshold and loose directionality, therefore is more poorly sampled.

These measurements were carried out also with the polarizer unfavorable for the Cherenkov side. In order to see the polarizer effect,

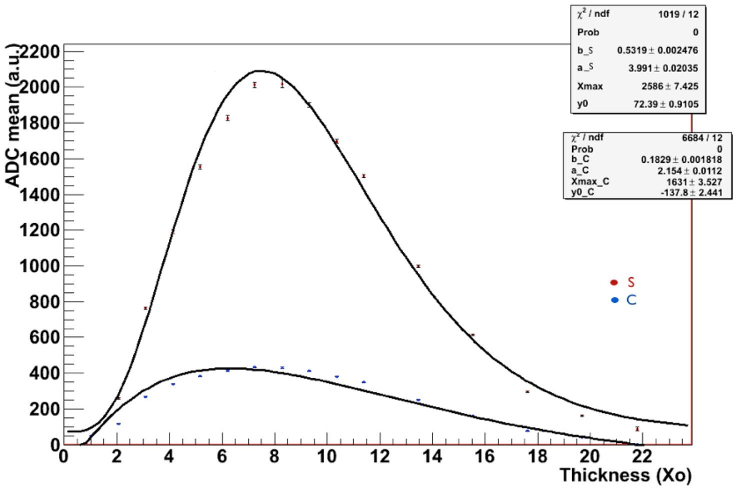

Figure 4.3.9: The longitudinal profile of the scintillation and Cherenkov light as a function of the radiation length. Polarization filter favorable.

the C/S ratio as a function of X_0 are shown for both configurations (Figure 4.3.10). As it is visible, polarization in the early stages ($< 7X_0$) of the shower is preserved, and the effect of the polarizer is relatively large. Indeed when the filter is favorable the C/S ratio is high while when the filter is unfavorable the Cherenkov light is strongly suppressed. After the shower maximum polarization has not a unique orientation, indeed after 15 X_0 the orientation of the polarizer has no meaning for the Cherenkov light: the C/S ratio is roughly the same for both configurations. This effect is shown also in Figure 4.3.11: after the maximum the two Cherenkov light profiles decay roughly the same, since in the late stages of the shower development particles are emitted mostly isotropically.

This aspect of Cherenkov radiation may be useful in different applications in calorimetry. In particular it might provide additional separation power in crystals which exploit the dual-readout technique.

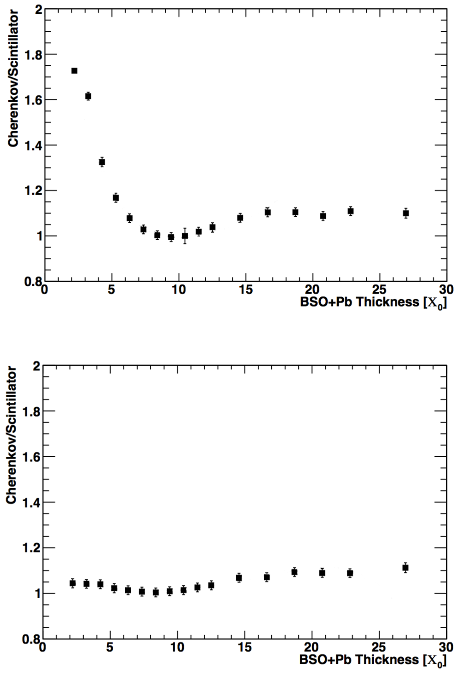

(a)

(b)

Figure 4.3.10: The C/S ratio as a function of the radiation length for polarizer favorable (a) and polarizer unfavorable (b).

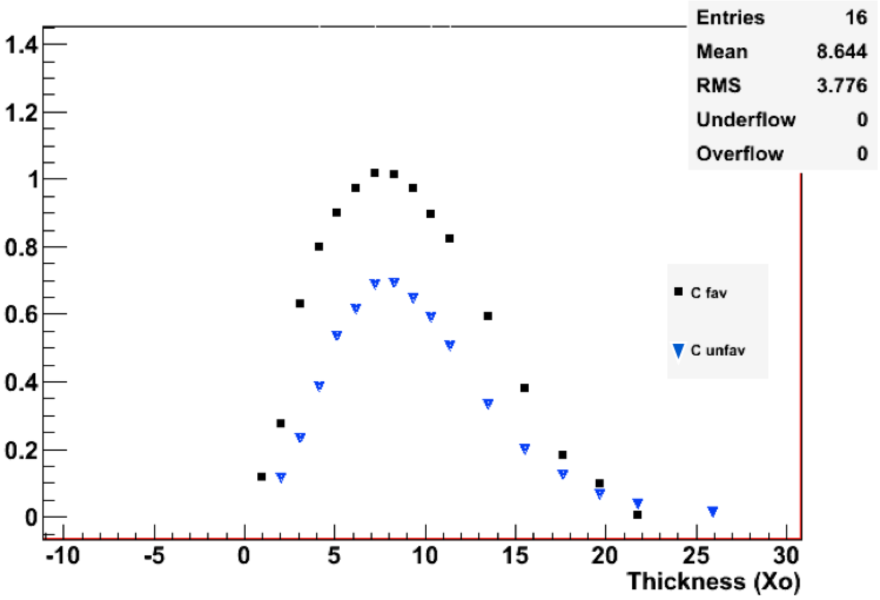

Figure 4.3.11: The shower profile for Cherenkov light, with polarizer favorable and unfavorable.

5

CONCLUSIONS

In the last quarter century, calorimeters have become very relevant in high-energies experiments. However, factors related to the detection of physical process hamper the exploitation of the full potential of these devices. Concerning the hadronic showers, the energy sharing between the em (the electromagnetic fraction, f_{em}) and the non-em component fluctuates strongly and in a non-Gaussian manner event by event, and it causes limitations to the hadronic detection performances. Besides, when nuclear interactions take place in the calorimeter, a fraction of the shower energy is used to unbind nucleons, and thus does not generate any detectable signals. All these problems give rise to non-linearity, non-Gaussian response functions, poor energy resolutions, etc. which prevent further improvement in the calorimeters performance.

Hadronic Monte Carlo shower simulations are not yet perfect, and in the past 30 years, progress have been achieved mainly through dedicated R&D projects. The Dual-readout Method (DREAM) allows to measure the electromagnetic shower fraction and the neutron fraction event by event, eliminating the relative fluctuations and making possible to reach the ultimate limit for the hadronic energy resolution. Until now, the DREAM Collaboration has designed and tested different prototypes, in order to test the validity of the principles on which improvement of the hadronic calorimeter performance is based.

In this thesis the application of the dual-readout methods to scintillation crystals is discussed in detail. In particular I have participated in the test of eight lead-tungstate crystal doped with 0.3% Molybdenum. The systematic analysis of the crystals points out that all of them have a good Cherenkov/scintillation separation. Besides, it turns out that this type of crystal is characterized by a Cherenkov light yield of at least 50 p.e. per GeV, which makes it suitable for the dual-readout method. On the other hand, Cherenkov light attenuation of even 18% in 10 cm has been observed, due to the small effective bandwidth for the Cherenkov signal. This aspect may be a problem in calorimeters where showers starting point fluctuates over distance of 20 cm. However, the reproducibility measurements have shown that changing accidentally the optical coupling affects the crystal response also at 15% level. Crystallographic measurements will be carried out towards the end of 2011 in order to determine possible differences between the crystals and check the results that we have achieved.

The preliminary results on an hybrid prototype, made of a lead-tungstate crystal matrix and the DREAM fiber prototype, show that the application of the dual-readout at both sections leads to Gaussian hadronic response and improvement in the hadronic energy resolution. It turns out that the C/S ratio of the crystal matrix is a good measure of the f_{em}, as in the case of the DREAM module in stand-alone mode. In particular the DREAM scintillation distributions for subsamples selected on the basis of the crystal matrix C/S are more Gaussian and narrower with respect to the total distribution. Concerning the electromagnetic response, the energy resolution of the central crystal turned out to be $12\%/\sqrt{E}$, with electrons shower containment at 82% level. Moreover, the crystal response is linear for both scintillation and Cherenkov light. Due to the not perfect calibration, caused by the poor beam condition, the energy resolution of the crystal matrix has been wrongly estimated. However a high performance of the crystal matrix in electromagnetic detection is expected, once that shower leakage are eliminated and the calibration is done properly.

The analysis done on the lead-tungstate matrix exploited both spectral and time structure differences between the Cherenkov and the scintillation light. The polarization of the Cherenkov light may provide a further tool in order to separate the Cherenkov and the scintillation light in crystals which make use of the dual-readout technique. Indeed the separation power of the C/S light increases of about 30%.

From these analysis turns out that a high hadronic energy resolution will be easily reached, once that the shower leakage fluctuations and instrumental effects will be eliminated or at least reduced.

In the next years, the DREAM Collaboration plans to construct a new fiber detector, large enough to contain high-energy hadronic showers at the 99% level and with several modifications addressing the weak points of the original detector. Moreover a crystal matrix, sufficiently large to serve as the electromagnetic section of a combined calorimeter, in which the fiber detector constitutes the hadronic section, will be constructed. This two detectors will be tested individually and in combination in high-energy beams of electrons and hadrons.

The dual-readout technique has already shown that it is suitable for high-quality calorimetry for all types of particles, with an instrument calibrated with electrons. The dual-readout calorimetry could thus meet the performance requirements of future experiments, such as the International Linear Collider (ILC) or the Compact Linear Collider (CLIC).

BIBLIOGRAPHY

[1] Introduction to the use of the h8 beam. *SL/EA/KE/*, 2000.

[2] U. Amaldi. *Phys. Scripta*, (23):409, 1981.

[3] CALICE Collaboration. Report to the calorimeter R&D review panel. *ILC Report*, 2007.

[4] The DREAM Collaboration. Dual-readout calorimetry for high-quality energy measurements. *Proposal and request to CERN's SPS Committee*, 2010.

[5] A. N. Diddens et al. *Nucl. Instr. and Meth.*, (178):27, 1980.

[6] D. Acosta et al. *Nucl. Instr. and Meth.*, A(294):193, 1990.

[7] D. Acosta et al. *Nucl. Instr. and Meth.*, A(308):481, 1991.

[8] D. Acosta et al. *Nucl. Instr. and Meth.*, A(136):184, 1992.

[9] H. Abramowicz et al. *Nucl. Instr. and Meth.*, (180):429, 1981.

[10] L. Bartoszek et al. *Nucl. Instr. and Meth.*, A(301):47, 1990.

[11] M. De Vincenzi et al. *Nucl. Instr. and Meth.*, A(243):348, 1986.

[12] M. G. Catanesi et al. *Nucl. Instr. and Meth.*, A(260):43, 1987.

[13] N. Akchurin et al. *Nucl. Instr. and Meth.*, A(399):202, 1997.

[14] N. Akchurin et al. *Nucl. Instr. and Meth.*, A(408):380, 1998.

[15] N. Akchurin et al. *Nucl. Instr. and Meth.*, A(533):305, 2004.

[16] N. Akchurin et al. *Nucl. Instr. and Meth.*, A(537):537, 2005.

[17] N. Akchurin et al. *Nucl. Instr. and Meth.*, A(536):29, 2005.

[18] N. Akchurin et al. *Nucl. Instr. and Meth.*, A(595):359, 2008.

[19] N. Akchurin et al. *Nucl. Instr. and Meth.*, A(593):530, 2008.

[20] N. Akchurin et al. *Nucl. Instr. and Meth.*, A(598):422, 2009.

[21] N. Akchurin et al. *Nucl. Instr. and Meth.*, A(598):710, 2009.

[22] N. Akchurin et al. *Nucl. Instr. and Meth.*, A(610):488, 2009.

[23] N. Akchurin et al. *Nucl. Instr. and Meth.*, A(621):212, 2010.

[24] N. Akchurin et al. *Nucl. Instr. and Meth.*, A(640):91, 2011.

[25] N. Akchurin et al. *Nucl. Instr. and Meth.*, A(638):47, 2011.

[26] T. A. Gabriel et al. *Nucl. Instr. and Meth.*, A(338):336.

[27] T. Akesson et al. *Nucl. Instr. and Meth.*, A(262):243, 1987.

[28] O. Ganel and R. Wigmans. On the calibration of longitudinally segmented calorimeter systems. *Nucl. Instr. and Meth.*, A(409):621, 1998.

[29] D. Green. *Proc. 4th Int. Conf. on Calorimetry in High Energy Physics*, La Biodola, Italy, eds. A. Menzione and A. Scribano, (Singapore: World Scientific), 1994.

[30] Erwin Hilger. The ZEUS uranium-scintillator calorimeter for hera. *Nucl. Instr. and Meth.*, 1987.

[31] J. Kruger. The uranium/scintillator calorimeter for the ZEUS detector at the electron-proton collider hera. *Internal Report DESY*, DESY F35-92-02, DESY Hamburg, 1992.

[32] W. R. Leo. Techniques for nuclear and particle physics experiments. 1987.

[33] G. Gaudio M. Livan and R. Wigmans. The art of calorimetry. *Proceedings of the International School of Physics "Enrico Fermi", Course CLXXV "Radiation and Particle Detectors"*, Edited by S. Bertolucci, U. Bottigli, P. Oliva, 2006.

[34] V. L. Morgunov. Calorimetry design with energy-flow concept. 2002.

[35] Journal of Physics G. Nuclear and particle physics. 37(7A):IOP Publishing, 2010.

[36] V. Radeka and W. J. Willis. *Nucl. Instr. and Meth.*, 120:221, 1974.

[37] C. Leroy Y. Sirois and R. Wigmans. *Nucl. Instr. and Meth.*, A(252): 4, 1986.

[38] M. Livan V. Vercesi and R. Wigmans. Scintillating-fibre calorimetry. *Yellow Report*, CERN 95-02.

[39] R. Wigmans. *Nucl. Instr. and Meth.*, A(259):389, 1987.

[40] R. Wigmans. *Nucl. Instr. and Meth.*, A(265):273, 1988.

[41] R. Wigmans. *Calorimetry: energy measurement in particle physics*. International series of monographs on physics. Clarendon Press, 2000.

[42] R. Wigmans and M. T. Zeyrek. *Nucl. Instr. and Meth.*, A(485), 2002.